ANKARA YILDIRIM BEYAZIT UNIVERSITY

GRADUATE SCHOOL OF NATURAL AND APPLIED SCIENCES



FABRICATION AND OPTIMIZATION OF HOMOJUNCTION PHOTOANODES-BASED DYE-SENSITIZED SOLAR CELLS

Ph.D. Thesis by

Abdullah ATILGAN

Department of Energy Systems Engineering

December, 2022

ANKARA

FABRICATION AND OPTIMIZATION OF HOMOJUNCTION PHOTOANODES-BASED DYE-SENSITIZED SOLAR CELLS

A Thesis Submitted to

The Graduate School of Natural and Applied Sciences of

Ankara Yıldırım Beyazıt University

In Partial Fulfillment of the Requirements for the Degree of Doctor of Philosophy in Civil Engineering, Department of Energy Systems Engineering

by

Abdullah ATILGAN

December, 2022

ANKARA

Ph.D. THESIS EXAMINATION RESULT FORM

We have read the thesis entitled **"FABRICATION AND OPTIMIZATION OF HOMOJUNCTION PHOTOANODES-BASED DYE-SENSITIZED SOLAR CELLS"** completed by **ABDULLAH ATILGAN** under the supervision of **PROF. DR. ABDULLAH YILDIZ** and we certify that in our opinion it is fully adequate, in scope and in quality, as a thesis for the degree of Doctor of Philosophy.

Prof. Dr. Abdullah YILDIZ

Supervisor

Prof. Dr. Bülent YEŞİLATA	Prof. Dr. Savaş SÖNMEZOĞLU
Jury Member	Jury Member

Prof. Dr. Sefer Bora LİŞESİVDİN	Prof. Dr. İlhan KOŞALAY
Jury Member	Jury Member

Prof. Dr. Sadettin ORHAN

Director

Graduate School of Natural and Applied Science

ETHICAL DECLARATION

I hereby declare that, in this thesis which has been prepared in accordance with the Thesis Writing Manual of Graduate School of Natural and Applied Sciences,

- All data, information and documents are obtained in the framework of academic and ethical rules,
- All information, documents and assessments are presented in accordance with scientific ethics and morals,
- All the materials that have been utilized are fully cited and referenced,
- No change has been made on the utilized materials,
- All the works presented are original,

and in any contrary case of above statements, I accept to renounce all my legal rights.

Date: 26.12.2022 **Signature: ……..**

Name & Surname: Abdullah ATILGAN

ACKNOWLEDGMENTS

Firstly, I would like to extend my gratitude and many thanks Prof. Dr. Abdullah YILDIZ for his guidance, keen knowledge, and patience. The door to Prof. Dr. YILDIZ's office was always open whenever I ran into a trouble spot or had a question about my research or writing. Working in his photovoltaic research group, supplied me with insights into a multidisciplinary approach, combining chemistry, physics, material science, and engineering. In addition to my advisor, I would like to thank the rest of my thesis committee: Prof. Dr. Bülent YEŞILATA, Prof. Dr. Savaş SÖNMEZOĞLU for their encouragement and insightful comments. Again, I would like to thank Prof. Dr. Sefer Bora LIŞESIVDIN and Prof. Dr. İlhan KOŞALAY for their valuable contributions.

Further, I would also like to thank Ankara Yıldırım Beyazıt University, and specifically the Department of Material Engineering for their XRD measurement support. I would like to express my thanks to Dr. Mahir GÜLEN for his support with chemical material. Apart from that, I would like to express my endless thanks to Erser ERGÜR from SLD Otomasyon, Cenk DIKMEN from 4K Kesici, Zafer YIĞIT from Nanografi, Arda MUNGAN from Teknotıp, and Adem YAZI from NeomLab, from whom I received support throughout my thesis process. I am also thankful to all my friends from laboratory especially Aycan ATLI, Dr. Kenan ÖZEL, Yusuf YILDIZ, and Z. Kerem YILDIZ for their support during my thesis work. I also thank my colleagues, Dr. Polat NARİN and M. Enes YELKOVAN.

I would like to convey my deepest gratitude to Bengisu ÇETINER OKŞİN and Mehmet ŞEN for helping to regain my health.

Finally, I must express my very profound gratitude to my parents, my wife Esma ATILGAN for her endless love and for providing me with unfailing support and continuous encouragement through the process of researching and writing this thesis.

2022, 26 December **Abdullah ATILGAN**

FABRICATION AND OPTIMIZATION OF HOMOJUNCTION PHOTOANODES-BASED DYE-SENSITIZED SOLAR CELLS

ABSTRACT

Today, when fossil resources are exhausted and energy needs increase day by day, interest in new energy sources and renewable energy resources has increased considerably. Furthermore, the growing global population, industrialization, and the negative effects of human hunger are manifesting themselves as an increase in greenhouse gas emissions, global warming, water pollution, and air pollution. Although the yields of existing solar cells are modest, the poisonous gases and production costs during production are a large dead end. At this point, third-generation solar cells grow. These batteries have a low recycling cost, and the cost is quite promising in terms of performance. Painted solar cells, one of the third-generation solar cell technologies, stand out with a low cost, low toxicity, and a simple production process. In the thesis study, the blocking layer and the key parameters affecting dye-sensitized solar cells efficiency, including porous TiO_2 and electrolyte, were studied. A strategy has been developed to increase the open circuit voltage and short circuit current together. A blocking layer has been produced using $TiCl_3$-based solutions optimized for production parameters. The efficiency is optimized with electrolytes used frequently in the literature for the final cell. Initially obtained, the battery's J_{SC} value was approximately 10 percent, the V_{OC} value was approximately 20 percent, and total cell performance was increased by approximately 80 percent to 8.03 percent. As a result, dye-sensitized solar cells are a promising renewable energy technology with great potential to reduce production costs and increase the efficiency of solar batteries. With ongoing research and development, dye-sensitized solar cells can eventually become the most cost-effective solar cells available on the market.

Keywords: Dye-sensitized solar cell, titanium dioxide, electrolyte, seed layer, homojunction photoanode.

HOMOJUNCTION FOTOANODE TABANLI BOYA DUYARLI GÜNEŞ PİLLERİN ÜRETİMİ VE OPTIMIZASYONU

ÖZ

Fosil kaynakların tükenmeye yüz tuttuğu ve enerji ihtiyacının günden güne arttığı günümüzde yeni enerji kaynakları ve yenilenebilir enerji kaynaklarına ilgi oldukça artmıştır. Bunların yanı sıra artan dünya nüfusu, sanayileşme ve insanoğlunun gün geçtikçe büyüyen enerji açlığının olumsuz etkileri sera gazı salınımı artışı, küresel ısınma, su ve hava kirliliği olarak karşımıza çıkmaktadır. Mevcut güneş pillerinin verimleri mütevazi değerlerde olsa da üretim sırasında çıkan zehirli gazlar ve üretim maliyetleri oldukça büyük bir çıkmazdır. Bu noktada imdada üçüncü nesil güneş pilleri yetişir. Bu piller düşük geri dönüşüm maliyetine sahip ve maliyet performans yönünden oldukça umut vericidir.

Üçüncü nesil güneş pili teknolojilerinden biri olan boyaya duyarlı güneş pilleri, basit üretim süreci, düşük toksisite avantajlarına sahip düşük maliyetli ile ön plana çıkmaktadır. Tez çalışmasında bloklama katmanı ve gözenekli TiO_2 ve elektrolit olmak üzere DSSCS verimi etkileyen anahtar parametereler üzerine çalışılmıştır. Açık devre voltaji ve kısa devre akımını birlikte artıracak strateji geliştirilmiştir. Bloklama katmanı olarak $TiCl_3$ temelli solusyon kullanılarak üretim parametreleri optimize edilmiş ve bloklama katmanlarının katitesini ortaya koyabilecek bir formül üretilmiştir. Final hücre için literatürde sıklıkla kullanılan elektrolitlerle verim optimize edilmiştir. Başlangıçta elde edilden pile ait J_{SC} değeri yaklaşık yüzde10, V_{OC} değeri yüzde 20 ve dolluluk oranı yüzde 35 ve toplam hücre performansı yaklaşık yüzde 80 artırılarak toplam verim 8.03 yüzde değerine taşınmıştır.

Sonuç olarak, DSSC'ler, üretim maliyetini azaltmak ve güneş pillerinin verimliliğini artırmak için büyük potansiyele sahip umut verici bir yenilenebilir enerji teknolojisidir. Devam eden araştırma ve geliştirme ile DSSC'ler sonunda piyasada mevcut olan en uygun maliyetli güneş pillerinin adayı haline gelebilir.

Anahtar Kelimeler: Boya duyarlı güneş pilleri, titanium dioksit, elektrolit, bloklama katmanı, homojuntion fotoanot.

NOMENCLATURE

Roman Letter Symbols

E_c	Energy of conduction band
E_v	Energy of valence band
E_{pa}	Anodic peak potential
E_{pc}	Cathodic peak potential
eV	Electron volt
I_{pa}	Anodic current
I_{pc}	Cathodic current
I_{SC}	Short circuit current
J_{SC}	Short circuit current density
P_{in}	Incident light power
R_s	Series resistance
R_{CE}	Charge transfer resistance at the counter electrode
R_{rec}	Electron recombination resistance at the photoanode
R_{sh}	Shunt resistance
V_{OC}	Open circuit voltage

Acronyms

ACN	Acetonitrile
AFM	Atomic force microscopy
AM1.5	Incident air mass 1.5 global spectrum
BMII	1-butyl-3-methylimidazolium iodide
BSE	backscattered electrons (BSE)
CB	Conduction band
CBD	Chemical bath deposition
CE	Counter electrode
CIGS	Copper-indium-gallium selenid
CuSCN	Copper(I) thiocyanate
CV	Cyclic voltammetry
CZTSSe	$Cu_2ZnSn(S,Se)_4$
DSSC	Dye-sensitized solar cell
EDX	Energy-dispersive X-ray spectroscopy

EIS	Electrochemical impedance spectroscopy
FF	Fill Factor
FTO	Fluorine-doped tin oxide
FWHM	Full width at half maximum
GuSCN	Guanidine Thiocyanate
HOMO	Highest occupied molecular orbital
ITO	Indium-doped tin oxide
IMVS	intensity-modulated photovoltage spectroscopy
LPD	liquid phase deposition
LUMO	Lowest unoccupied molecular orbital
N719	Ru3(NCS)2 dye
NREL	National Renewable Energy Laboratory
OSC	Organic solar cell
P25	20 nm sized Titanium Dioxide Nanopowder
PA	Photoanode
PCS	perovskite solar cells
PEDOT	Poly(3,4-ethylenedioxythiophene)
PEG	polyethylene glycol
PV	Photovoltaic
QDSC	Quantum dot solar cell
SE	Secondary electrons
SEM	Scanning electron microscopy
SQ	Shockley-Queisser
TBP	4-tert-butylpyridine
UV	Ultraviolet
XRD	X-ray diffractometry

CONTENTS

Ph.D. THESIS EXAMINATION RESULT FORM ii
ETHICAL DECLARATION iii
ACKNOWLEDGMENTS iv
ABSTRACT v
ÖZ vi
NOMENCLATURE vii
CONTENTS ix
LIST OF TABLES xii
LIST OF FIGURES xiii

CHAPTER 1-INTRODUCTION 1
1.1 Background 1
1.2 Energy Needs and Current Energy Resources 1
1.3 Objectives, Scope, and Layout of This Thesis 5
1.4 Thesis Outline 6

CHAPTER 2-THEORETICAL BACKGROUND 7
2.1 Photovoltaic Technologies 7
2.2 Emerging Solar Cell Technologies 9
2.3 Introduction of Dye-Sensitized Solar Cells 11
2.4 Basic Components of Dye-Sensitized Solar Cells 12
2.4.1 Transparent conducting oxide glass substrate 13
2.4.2 Wide bandgap semiconductor 14
2.4.3 Dye as the photosensitizer 15
2.4.4 Redox mediator 16
2.4.5 Counter electrode 17
2.5 Working Principle of a Typical DSSCs 18
2.5.1 Design of test specimens 19
2.5.2 Electron injection 20
2.5.3 Electron transport 20
2.5.4 Reduction of the redox mediator 21
2.5.5 Electron recombination 21
2.6 The Fundamental Manufacturing Processes Utilized by DSSCs 22

2.6.1 Spin Coating 23
2.6.2 Doctor Blading 24
2.6.3 Chemical bath deposition 25
2.6.4 Template method 26
2.6.5 Realizing the Limits of Dye-Sensitized Solar Cells 26
2.7 Literature Review 28
2.7.1 An Ideal Blocking Layer for DSSCs 29
2.7.2 Effect of TiO_2 nanoparticle characteristics 30
2.7.3 Impact of the paste's composition 31
2.7.4 Effect of the structure of the film 32
2.7.5 The influence of sintering temperature profile and $TiCl_4$ post-treatment 33

CHAPTER 3- THEORETICAL CALCULATIONS 34
3.1 XRD Analysis 34
3.2 AFM Analysis 36
3.3 SEM Analysis 38
3.4 EDX Analysis 39
3.5 Transmittance and absorbance analysis 41
3.6 Figure of Merit 42
3.7 JV Analysis 43
3.8 EIS and Bode Analysis 45
3.9 Mott-SchottkyAnalysis 48

CHAPTER 4- MATERIALS AND METHODS 51
4.1 Chemical Materials Used in Experimental Studies 51
4.2 Cell Production 52
4.2.1 Cleaning of FTO substrates 52
4.2.2 Production of the compact TiO_2 layer 52
4.2.3 Production of the mesoporous TiO_2 layer 53
4.2.4 Production of the electrolytes 54
4.2.5 Dye loading the working electrodes. 55
4.2.6 Counter electrode preparation 55
4.2.7 Cell assembly 55

CHAPTER 5- RESULT AND DISCUSSION 56
5.1 $TiCl_3$ Based Blocking Layer 56
5.1.1 Surface examination of the blocking layer by SEM 59
5.1.2 UV-Vis and AFM results $TiCl_3$ based compact layer 63
5.1.3 Change of resistivity of FTO/TiO_2 under various test parameters ... 72
5.1.4 EDS Analysis for Annealing Time and Temperature 76
5.1.5 Figure of merits FTO/TiO_2 films 77
5.2 Ni-doped TiO_2/TiO_2 homojunction photoanodes 79
5.2.1 SEM analysis of modified and bare particles 79
5.2.2 Elemental analysis of bare and modified P25 NPs 80
5.2.3 XRD Anaysis of NPs 81
5.2.4 Raman spectra of particles 82
5.2.5 UV-Vis Spectra of PAs 84
5.2.6 The flat-band potential 87
5.2.7 Photovoltaic performance parameters 89
5.2.8 EIS measurements 91
5.3 Optimization of Electrolyte 98
5.3.1 Introduction 98
5.3.2 Specifications of electrolyte components 101
5.3.3 Photovoltaic performance parameters 104

CHAPTER 6- RESULT AND DISCUSSION 108
6.1 Conclusions 108
6.2 Outlook 109
REFERENCES 110
CURRICULUM VITAE 136

LIST OF TABLES

Table 2.1 Estimated PCE and loss efficiencies for a device with Eg=1.31 eV 28

Table 4.1 Optimization parameters of c-TiO_2 layer. 53

Table 4.2 Receipts of electrolytes. 54

Table 5.1 Comparison of the sheet resistance of FTO/TiO_2 layers formed to that of FTO and other coated films..... 73

Table 5.2 Photovoltaic performances of the DSSCs based on different photoanodes measured under simulated 100 mW/cm^2 AM 1.5 illumination. *Average values from 5 devices..... 91

Table 5.3 Parameters determined by EIS for the devices assembled with different photoanodes..... 95

Table 5.4 Physical characteristics of commonly employed solvents 102

Table 5.5 Performance parameters of DSSCs various electrolytes..... 106

LIST OF FIGURES

Figure 1.1 Roadmaps for 100% Clean and Renewable Wind, Water, and Sunlight Energy for a) world and b) Türkiye 3

Figure 1.2 Solar Radiation Spectrum Solar radiation is the radiant energy emitted by the Sun. 4

Figure 1.3 Representation of the atmospheric sunlight absorption associated with various air mass indices and the corresponding solar radiation spectrum. 4

Figure 2.1 History of solar energy: timeline and invention of solar panels 8

Figure 2.2 In comparison to the Shockley-Queisser efficiency limit, a variety of third-generation solar systems have achieved record efficiencies and band gaps in accordance with those efficiencies. 10

Figure 2.3 A schematic illustrating the main components of a dye-sensitized solar cell. 13

Figure 2.4 a) A schematic of the working principle of dye-sensitized electrochemical photovoltaic cells b) The kinetic data for the different electron transfer processes taking place at the oxide/dye/electrolyte (TiO_2/Ru-sensitizer/iodide-triiodide) interface for DSSC under working conditions (Standard 1 Sun) 19

Figure 2.5 Some production techniques used for DSSC. 23

Figure 2.6 Schematic of chemical bath deposition technique 26

Figure 2.7 Fishbone diagram for DSSC performance enable research scope at various levels. 29

Figure 3.1 Bragg's law diagram 35

Figure 3.2 Working principle of X-ray diffraction (XRD) 35

Figure 3.3 Rigaku Miniflex 600 XRD 36

Figure 3.4 Working principle of AFM 37

Figure 3.5 Q-Scope™ 250AFM 38

Figure 3.6 Interaction of the electron signal with the specimen upon contact. SE1 corresponds to secondary electron mode, while SE2 and SE3 are employed in back scattered 39

Figure 3.7 X-ray spectrum types shown schematically as a result of rapid electron bombardment. 40

Figure 3.8 I-V curve to evaluate the cell performance 44

Figure 3.9 (a) Charge transfer kinetics involved in dye-sensitized solar cells where dark arrow shows loss mechanism: (1) injection of electrons, (2) diffusion of electrons in the TiO_2, (3) regeneration of dye, (4) regeneration of redox mediator (I_3^-/I^-), (5) diffusion of I_3^-, (6) diffusion of I^-, (7) back reaction of TiO_2 conduction band electrons with I_3^-, (8) recombination of electrons with oxidized dye, and (9) back reaction of electrons from FTO to I_3^- 45

Figure 3.10 (a) Nyquist plot of DSSC (b) bode plot of DSSC 48

Figure 3.11 Schematic illustration of band bending at the n-type semiconductor/electrolyte interface. 49

Figure 5.1 The requirements of an ideal blocking layer. 57

Figure 5.2 SEM topographies of (a) bare FTO, (b) 25 mM , (c) 50 mM, and (d) 100 mM solution of $TiCl_3$ aqueous was spin-coated onto clean FTO substrates..... 59

Figure 5.3 Comparison of the FE-SEM images of bare and coated FTOs under various spinning speed. 60

Figure 5.4 Top-view SEM image of bare and coated FTOs under various drop cycles. 61

Figure 5.5 Comparison of the FE-SEM images of bare and coated FTOs under various annealing temperatures. 62

Figure 5.6 FE-SEM surface morphologies of uncoated and coated FTOs sintered at 450 degrees Celsius for 15, 30, and 60 minutes. 63

Figure 5.7 a) Transmittance spectra b) relative changes against FTO according to concentration of precursor, surface topologies of c) bare FTO, and coated FTOs with solution of d) 25 mM, e) 50 mM and f) 100 mM $TiCl_3$ in isopropanol. 65

Figure 5.8 a) Transmittance spectra b) relative changes against FTO according to roational speed, and surface topologies of c) bare FTO, and spin-coated FTOs at d) 1.6K , e) 3.2K and f) 6.4K rpm. 66

Figure 5.9 a) Transmittance spectra and b) relative change against FTO according to various coating cycles, and surface topologies of c) uncoated, coated for d) 8, e) 16 and f) 32 cycles. 68

Figure 5.10 a) Transmittance spectra and b) relative change against FTO according to various annealing time, and surface topologies of c) uncoated, anealed for d) 15, e) 30 and f) 60 minutes..... 70

Figure 5.11 a) Transmittance spectra and b) relative change against FTO according to various annealing temperature, and surface topologies of c) bare, anealed at d) 350, e) 450 and f) 550 C°. 72

Figure 5.12 Comparison of the sheet resistance of FTO/TiO_2 layers formed to that of FTO and other coated films..... 75

Figure 5.13 The average spectrogram of mCl^{-1} versus annealing temperature with annealing temperature. The point-intersected dashed lines represent the ideal chosen temperature and time to exclude all chlorides..... 77

Figure 5.14 a) The effect of 10% Rsh change on FOM value under constant transmittance, b) Effect of 10% transmittance change on FOM under constant R_{sh}. 78

Figure 5.15 FESEM images of (a) Ni-doped, (b) bare P25 nanoparticles, and the particle distribution of (c) Ni-doped, (d) bare P25 nanoparticles. In order to find mean and median of particle sizes the abundant versus particle diameter graphs were fitted to Lorentzian equation 80

Figure 5.16 EDAX spectra of (a) Ni-doped, and (b) bare P25 nanoparticles 81

Figure 5.17 XRD patterns of bare and modified P25..... 82

Figure 5.18 Raman spectra of undoped and Ni-doped TiO_2..... 83

Figure 5.19 The Tauc's plots to determine the band gap value of undoped and Ni doped TiO_2..... 84

Figure 5.20 Relative UV-vis absorption spectra of the dye loaded photoanodes 85

Figure 5.21 The absorption spectra and relative change according to wavelength of undoped and Ni doped TiO2 mono layer thin films 86

Figure 5.22 Mott-Schottky curve of photoanodes..... 88

Figure 5.23 J-V curve of the devices based on various photoanodes. 89

Figure 5.24 (a) On the basis of various photoanode Nyquist plots, EIS measurements for the devices were performed. (b) Plots of Bode phase angle versus frequency. ... 92

Figure 5.25 The statistical distribution of the photovoltaic characteristics of DSSCs with different placements of modified layer (a) distribution of J_{SC} (b) V_{OC} (c) FF (d) PCE. The J-V curves are used to extract parameters under AM 1.5 conditions. Five 0.16 cm^2 cell active area devices have been produced for each DSSC assembly..... 94

Figure 5.26 Schematic illustration of DSSCs containing different photoanodes of (a) TT, b) NN, c) TN, and d) NT..... 97

Figure 5.27 The energetics of DSSCs in relation to the redox potentials of each of commonly used redox couples that are employed in DSSCs..... 100

Figure 5.28 Schematic energy level diagram of a dye-sensitized solar cell. 103

Figure 5.29 JV curves of DSSCs..... 104

Figure 5.30 Performance parameter statistics of solar cells versus electrolyte..... 106

CHAPTER 1

INTRODUCTION

1.1 Background

Humanity, which has needed energy since its existence, has become heavily dependent on energy due to agricultural and industrial mechanization, industrialization, and urbanization. Fossil fuels are not only limited and environmentally harmful, but crises such as the 1973 World Oil Crisis and the 2022 Russian-Ukraine conflict also show that fossil fuel supply is not sustainable. The price of food and energy around the world is rising quickly as a direct result of global outbreaks, climate change, and military conflicts between governments. For these reasons, interest in solar energy, which provides renewable, environmentally friendly, and endless energy, has increased considerably. In this section, the place of photovoltaic technology among renewable sources of energy is discussed in terms of increasing energy needs and the status of existing energy resources. The working principle and existing problems of dye-sensitized solar cells (DSSCs), one of the generational solar cell species, are emphasized. In this context, the suggestions developed for the solution of existing problems are explained in line with the purposes of the thesis study.

1.2 Energy Needs and Current Energy Resources

The rapid growth of the world's population brings about numerous challenges in its wake. According to Nobel laureate Richard Smalley [1], energy is humanity’s greatest problem in the next fifty years. Smalley adds that locating sustainable sources of energy for the entire world will not only alleviate a developing energy crisis but will also aid in the resolution of the world's numerous other issues, such as water, terrorism, war, and health. In addition to determining the scope of the problem, Smalley summarizes its vision for our future: the complete transition to renewable energy resources through the development of cost-effective technologies that capture the sun, wind, and geothermal energy is possible [2].

Energy is critical to economic and social progress and increased quality of life in many nations, including Türkiye. Diversifying energy sources and investing in renewable energy are both important visions for a country's economic future. In the wake of the agricultural and industrial revolutions, human populations have expanded at an unprecedented rate. Population growth poses a significant threat to plant life, ecosystems, and the planet's long-term viability. Apart from the fact that existing energy sources will be depleted soon, the usage of these fossil-based fuels generates pollution, which is becoming an increasingly serious threat with each passing day. This pollution rapidly alters the global climate, jeopardizing the entire natural equilibrium. As a result, there are severe concerns regarding the quality of life for humanity. Energy, which is the basic indicator of socioeconomic growth all over the world, is becoming increasingly important due to finite energy resources and the fact that it is continuously consumed, requiring countries to re-examine climate policy and use energy more effectively. Many national and international legal agreements, such as the Kyoto Protocol and the Paris Climate Agreement, have been formed for reasons such as limiting global harm and releasing fewer greenhouse gases [3].

At this point, clean and sustainable options to meet energy demands were sought. Many scientists and researchers argue that nuclear energy could be an option. Nuclear energy is a low-carbon and cost-effective energy source. It also has one of the least significant carbon footprints. Unfortunately, the Fukushima Nuclear Disaster triggered the tsunami that emerged in Japan after the earthquake in 2011. Three of Fukushima Daiichi's reactors overheated, resulting in meltdowns and explosions that released enormous amounts of radioactive material. After the Chernobyl disaster, what happened at Fukushima Daiichi once again caused humanity to question its belief in nuclear power plants.

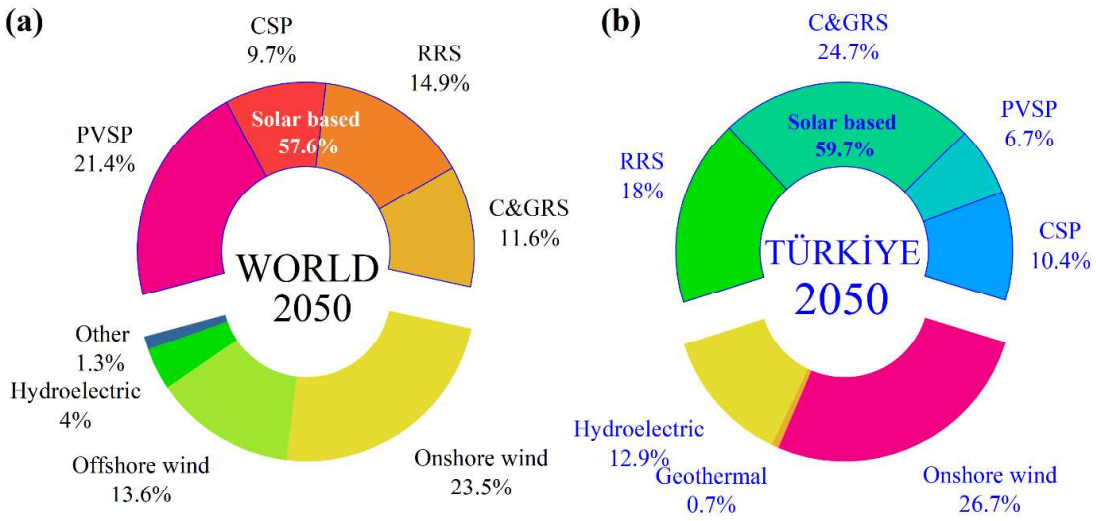


Figure 1.1 Roadmaps for 100% Clean and Renewable Wind, Water, and Sunlight Energy for a) world and b) Türkiye

According to data from last year (Statistical Review of World Energy 2021), 83 percent of the world's electricity demands were met by coal, oil, and natural gas [4]. Apparently, we are far from where we should be. Jacobson et al. created roadmaps to convert 139 countries' all-purpose energy infrastructures (electricity, transportation, heating and cooling, industry, agriculture/forestry/fishing) to ones driven by wind, water, and sunlight [5]. According to Jacobson et al., it is possible to use completely clean energy in 2050. The use of solar-based renewable energy resources in the world and Türkiye is 57.6% and 59.7%, respectively, and PV applications are 46% and 49.3% in all of them, respectively. Solar cell applications for the world and our country are the top priorities [6].

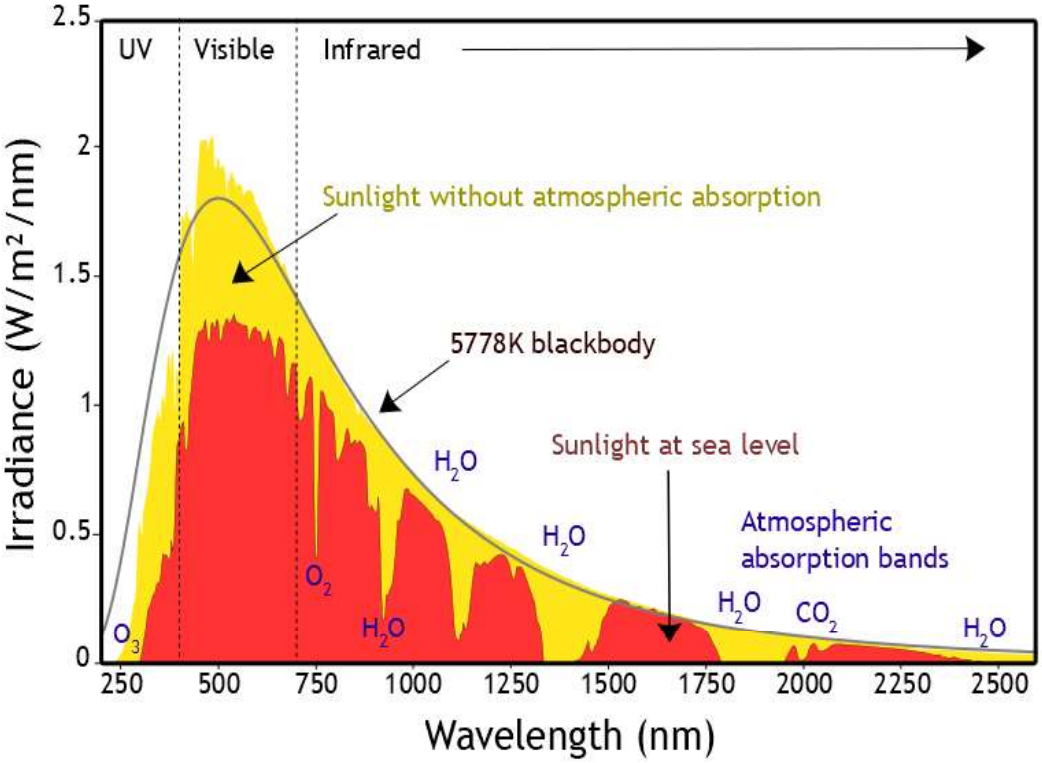


Figure 1.2 Solar Radiation Spectrum Solar radiation is the radiant energy emitted by the Sun.

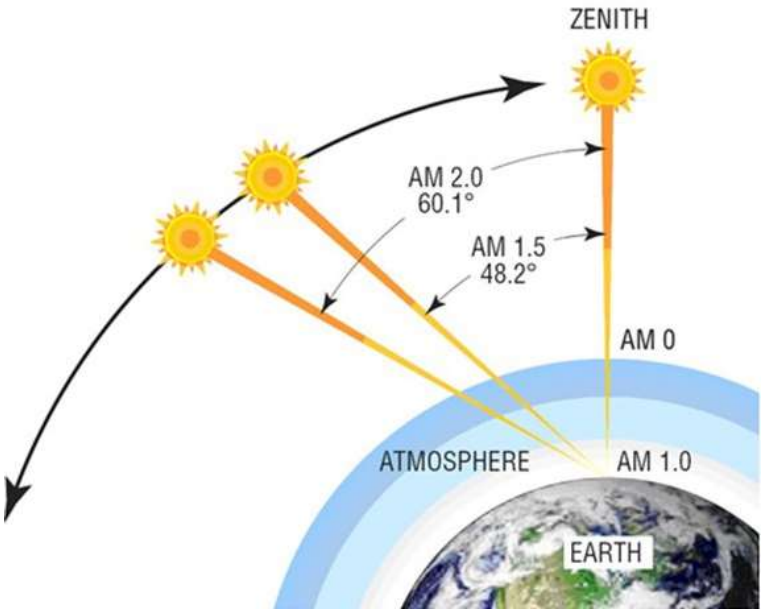


Figure 1.3 Representation of the atmospheric sunlight absorption associated with various air mass indices and the corresponding solar radiation spectrum.

Precipitation, clouds, and sandstorms reduce solar radiation in the visible spectrum. Because most ultraviolet solar radiation is absorbed and does not reach the earth's surface, the peak of the solar radiation that reaches the earth's surface is in the visible portion of the spectrum. About three-quarters of the total radiation reaches the Earth. The solar spectrum energy distribution is approximately 5% UV, 43% visible, and 52% infrared.

Hydrogen is being converted to helium in the sun's core. This process is called nuclear fusion. Four hydrogen atoms are required to create one helium atom. A portion of the mass is converted into energy during the process. This energy illuminates and warms our world. The air mass index is associated with the spectral energy distribution of light (see Figure 1.3). AM0 represents the spectrum standard for space applications. It possesses a total output of 1366.1 W/m^2. Two criteria for terrestrial use have been established. The AM1.5 Global spectrum is designed for modules with 1000 W/m^2 (100 mW/cm^2) of integrated power. AM1.5 Direct (+circumsolar) spectrum is specified for solar concentrator work.

1.3 Objectives, Scope, and Layout of This Thesis

Dye-sensitized solar cells (DSSCs) are an emerging and attractive contender for a future renewable energy source due to their possible low production cost, incorporation of ecologically benign components, and reasonable energy conversion efficiency. Understanding and developing the blocking layer, mesoporous layer (m-TiO_2), and ionic liquid have required significant effort. It must be emphasized that each component is crucial to the overall performance. The primary objective of this thesis and research is to enhance device performance and develop novel process variants. In this study, three major components are explored. For the blocking layer, a spin-coatable formulation was produced using $TiCl_3$ as a precursor. In addition, spin-coatable pastes have been developed for the mesoporous TiO_2 layer. The surfaces of the P25 particles were treated using NiO. The treated and untreated P25 particles were used as two layers in the mesopore section and allowed to form a homojunction. The most efficient position of this component has been determined.

Finally, the recipe was optimized according to the newly designed structure, and the most suitable electrolyte was determined for this structure.

1.4 Thesis Outline

The outline of this thesis is as follows:

Chapter 1 presents an introduction to the thesis topic. It includes a justification for this work and a summary of the structure of the thesis.

Chapter 2 describes DSSCs, their operating principles, and relevant literature. It provides a summary of the classification of PV technologies and their respective milestones. It discusses current research in the field of DSSC and provides an overview of the requirements for a high-performance device.

Chapter 3 discusses the theoretical calculations of a DSSC device's performance. Also discussed is the relationship between theory and experiment.

Chapter 4 outlines the utilized materials, experimental methodologies, and characterization techniques utilized in this investigation. In this chapter, the reader will receive information about character analysis techniques.

Chapter 5 covers the experimental outcomes and provides a discussion of the experimental data.

Chapter 6 concludes the DSSC's developments and outlines potential future possibilities.

CHAPTER 2

THEORETICAL BACKGROUND

This section contains background information for readers on dye-sensitized solar cells and covers their functioning principle. This document provides information regarding dye-sensitized solar cells. Following that, an overview of the most recent research is provided to provide readers with an up-to-date grasp of the technology and to highlight the significance of the work presented in this study to the field.

2.1 Photovoltaic Technologies

The Swiss physicist Horace-Bénédict de Saussure constructed heat traps in the 18th century. Heat traps can be thought of as a form of miniature green house. He built heat boxes by placing a glass box inside of a larger glass box for a total of up to five boxes in each unit he created. The temperature in the innermost box may reach levels as high as 108 degrees Celsius when it is subjected to direct solar irradiation. This is hot enough to cause water to boil and to prepare food. One could argue that these containers were the very first solar collectors ever created [7]. Solar energy is converted into electrical energy with the help of photovoltaic devices. In 1839, French physicist Alexandre-Edmund Becquerel was the one who first identified the "photovoltaic phenomena," which ultimately led to the development of the idea of a photovoltaic device. While studying the effect of light in electrolytic cells, Becquerel observed that the tension between platinum electrodes immersed in the electrolyte was dependent on the light falling on the electrolyte. In 1883, Charles Fritts developed the first solid-state photovoltaic cell by forming the connections by covering the semiconductor selenium with a thin layer of gold; the device was only around 1% efficient. Bell Labs reported the first workable silicon solar cell on April 25, 1954, with a 6 per cent efficiency. The Centre for Photovoltaic Engineering at the University of New South Wales developed 20% efficient silicon solar cells in 1985 [8-10]. The efficiency barrier of 40 percent was broken for the first time by a metamorphic three-junction GaInP/GaInAs/Ge solar cell in the year 2006 [11].

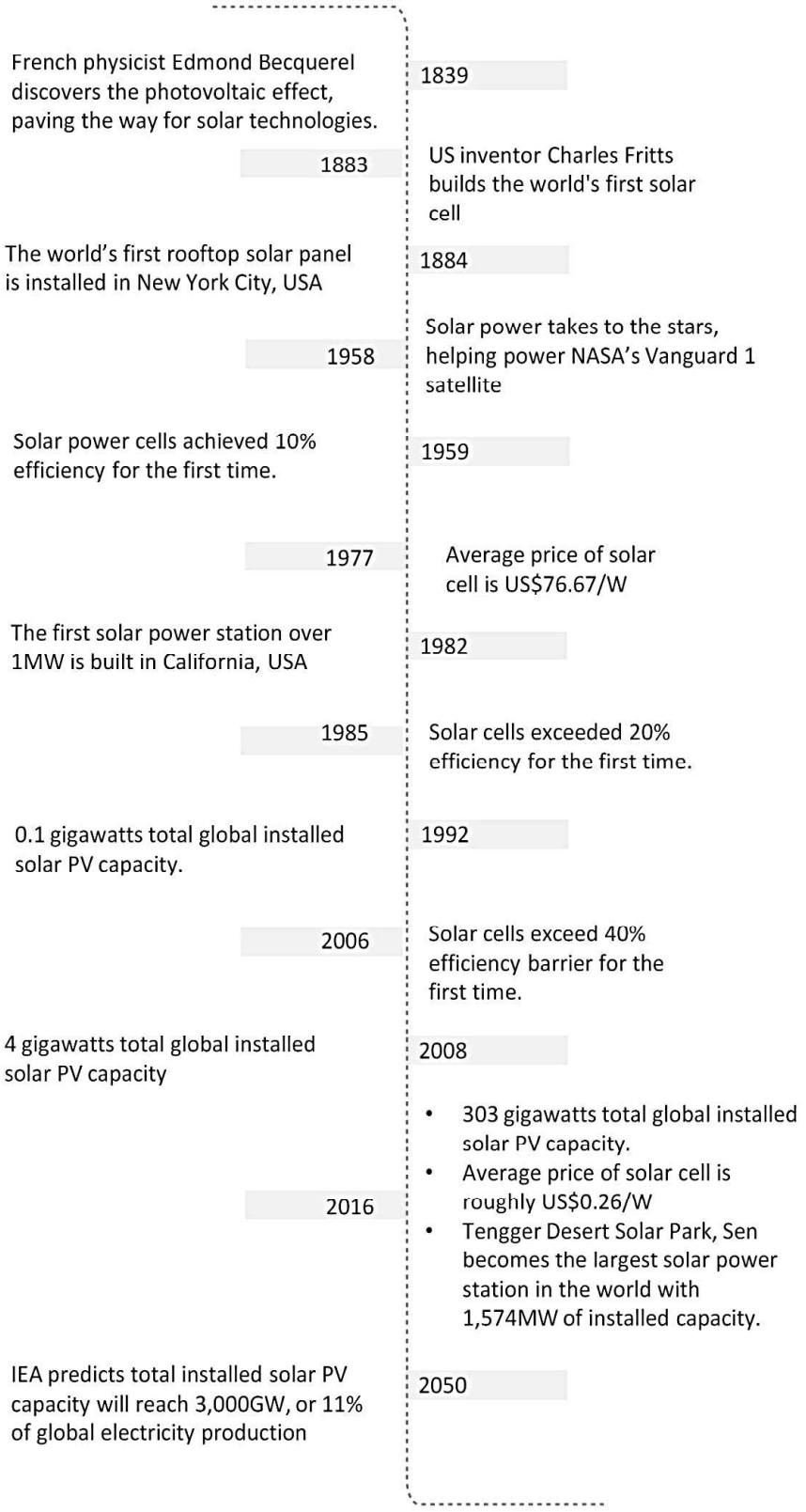


Figure 2.1 History of solar energy: timeline and invention of solar panels

Solar energy has some advantages in comparison with wind and geothermal energy. Solar energy is the most eco-friendly kind of generating because it does not contribute to the release of greenhouse gases or pollutants and does not endanger any forms of natural life. It is possible to use it almost anywhere, and it can be harnessed even in rural areas that are not connected to the electrical grid. It is a solution that is both practical and economical, as it does not necessitate large wiring costs and has relatively minimal maintenance costs. In addition to being inexpensive, solar power plants take up very little room because they are typically erected on rooftops [12, 13]. In addition to this, they have a lengthy life cycle and do not require manual monitoring. Considering all the above, people can much more easily persuade themselves to install solar panels on their roofs rather than wind turbines or geothermal plants in their backyard. Furthermore, wind turbines generate noise pollution due to their operation, and geothermal power plants can cause earthquakes. [14, 15].

Despite all their advantages, solar systems have not been widely adopted. The main obstacle facing solar systems is their cost. If solar cell companies can reduce costs enough, they will be able to compete with electric and natural gas companies. If prices continue to drop, solar cells might change the whole idea of energy, making it cheaper and easier for individuals to gather for themselves. That's what Smalley calls "disruptive technology" [1, 16].

2.2 Emerging Solar Cell Technologies

In recent years, novel solar cell ideas have been considered. Third-generation photovoltaic systems are mostly concentrated photovoltaic technology. Since the third-generation solar cells are designed with the experience gained from the first- and second-generation solar cells, they have several advantages over older generations. Due to the low-cost materials and simple manufacturing, it is anticipated that these technologies will play a large role in the rapidly expanding solar industries. In addition to the third-generation technologies, a number of innovative solar cell technologies utilizing quantum dots/wires, quantum wells, and superlattice technologies are now under development. By bypassing the thermodynamic

restrictions of traditional crystalline cells, these technologies may make it possible to achieve extremely high efficiencies. In 1961, William Shockley and Hans Queisser collaborated on a study that came to be known as the Shockley-Queisser limit [17]. In this study, they determined the parameters that influence the efficiency with which energy is transformed. The Shockley-Queisser limit is an indication of the highest theoretical efficiency that may be achieved by a single pn junction cell. This limit is computed based on the quantity of electricity that is generated per photon of the incoming radiation. Under the conditions of the AM1.5 sun spectrum, the limit suggests that a single pn junction with a home band range of 1.34 eV implies that the highest efficiency in the conversion of solar energy into electricity may be roughly 33.7%. (Air Mass 1.5).

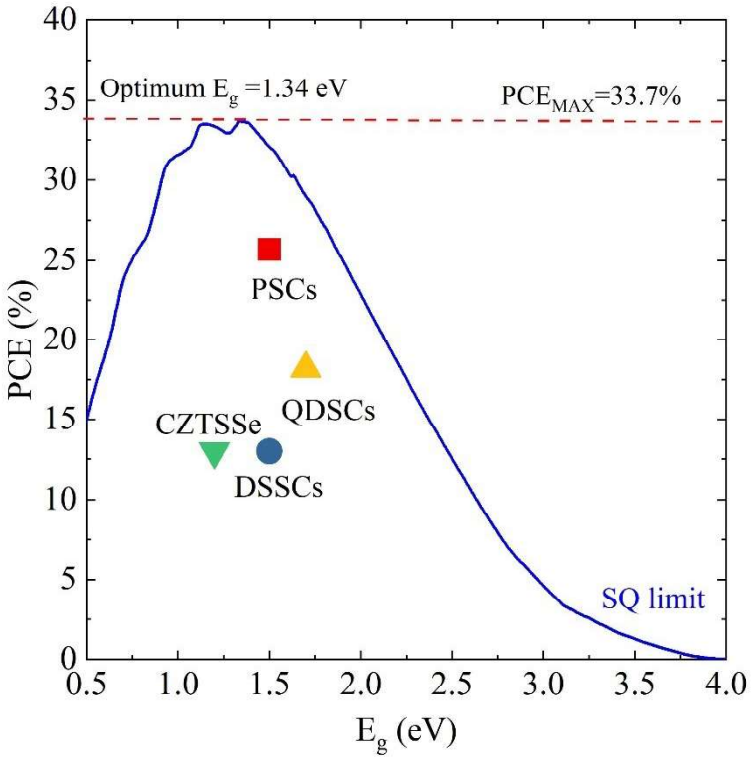


Figure 2.2 In comparison to the Shockley-Queisser efficiency limit, a variety of third-generation solar systems have achieved record efficiencies and band gaps in accordance with those efficiencies.

2.3 Introduction of Dye-Sensitized Solar Cells

When we look at the solar cell production process, we realize that the use of high-purity silicone is the solution to regeneration difficulties, but the purification procedure is difficult and extremely expensive. Because of this cost, solar panels are unable to compete with energy sources that are based on fossil fuels, and the cost of solar panels reflects this inability. Due to these factors, more affordable materials and a photovoltaic system should be developed as soon as possible. Photoelectrochemical solar cells are a great option for these kinds of solar cells, and they are one of the best options overall.

Michael Gratzel, and Brian O'Regan created a photoelectrochemical battery system in 1991. They reached an efficiency of 7% by manufacturing ruthenium complex dye and nano-crystalline titanium dioxide [18]. This efficiency has reached up to 15.2% as of today [19].

A nanostructured wide-band gap semiconductor is frequently employed as the base material in the manufacturing of DSSCs. Although TiO_2 is the most popular option, n-type metal oxides including ZnO, WO_3, SnO_2, Nb_2O_5, and $SrTiO_3$ are also frequently utilized as components of the semiconductor layer. A conductive substrate is used for the metal oxide deposition, and, among the many viable substrate options, the one with a transparent fluorine-doped tin oxide (FTO) coating is typically selected. To prevent certain recombination pathways, a blocking layer can be placed between the FTO and the semiconductor. This layer should locate between FTO and semiconductor layer. After a sensitizer has been adsorbed onto a photoanode, it is termed complete and ready for use. Sensitizers for use with DSSCs are abundant in variety. These sensitizers fall into two distinct categories: metal-organic complexes and organic dyes [20-23]. Due to its large surface area, the nanostructure can absorb a great deal of light from incident photons, making it ideal for photovoltaic applications. Due to the nanostructured semiconductor's porous nature, a redox electrolyte or a substance that transports holes can now enter it. To complete the DSSC, a cathode composed of a catalytically active material toward the redox mediator, or HTM, is employed. Carbon-based compounds, conductive polymers

(such as PEDOT), and precious metals are the most typical alternatives (such as platinum, gold, and silver) [24].

In summary, in a silicon solar cell, the semiconductor serves as both the electron source and electric field provider, whereas in a DSSC, the semiconductor is primarily employed for charge transport, and photoelectrons are provided by a separate source (dye). DSSCs can work in low-light circumstances, making them suitable even in cloudy weather and indirect sunlight, where conventional cells fail. On the contrary, the interruption in DSSC is very low, so it is ideal for indoor use to gather energy for small appliances from house lights. DSSCs are the solar cells of the most recent generation, and they have cheap production costs, a fast energy payback time, and low generation energy consumption.

2.4 Basic Components of Dye-Sensitized Solar Cells

The usual structure of the DSSC is made up of five primary components, as depicted in Figure 2.3:

- a transparent conducting oxide (TCO) glass substrate.
- a wide bandgap semiconductor (typically a nanocrystalline TiO_2 film coated on the TCO glass substrate)
- a dye sensitizer attached to the TiO_2 film's surface.
- a redox mediator, a volatile electrolyte comprising the iodine/triiodide (I^-/I_3) redox couple; and
- a counter electrode, often a platinum coated TCO glass substrate.

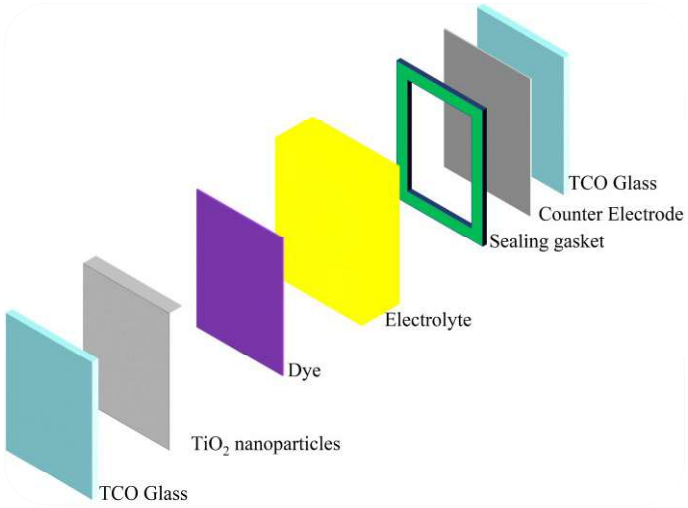


Figure 2.3 A schematic illustrating the main components of a dye-sensitized solar cell.

2.4.1 Transparent conducting oxide glass substrate

Due to their remarkable optical transparency in the visible and near-infrared areas of the electromagnetic spectrum, transparent conductive glasses are extensively employed as bottom materials in DSSCs. Moreover, depending on the band tension of the semiconductor, the UV-light-blocked training of TCOs may also be a factor in the choice of photodecomposition. The conductor layer (film) is expanded on the lower glass surface. While allowing sunlight to reach the cell through this portion, it transmits electron carriers to the external circuit, which has a significant impact on cell efficiency.

The most common transparent conductive oxide coated glasses are Fluorine doped Tin Oxide (FTO, SnO_2: F) and Indium doped Tin Oxide (ITO, SnO_2: In). ITO films have a visible area transparency of 83-87% and a sheet resistance of 8-100 Ω/cm^2, whereas FTO films have a visible region transparency of 82-85% and a sheet resistance of 7-13 Ω/cm^2 for TCOs intended for use. During the process of TiO_2 and Pt layer preparation, the sintering temperatures of substrates are increased to 450-500 °C to meet the thermal strength requirement. In DSSCs, both ITO and FTO are used. However, because ITO layers aren't very stable at high temperatures and the element is rare, FTO glass is usually chosen.

In short, the TCO processes are not easy to do, and a successful DSSC design of TCO requires high optical transparency, low resistance, and high thermal strength.

2.4.2 Wide bandgap semiconductor

The dye-sensitized broadband gap semiconductor oxide layer is a crucial performance element for DSSCs made from semiconductor oxide material. In DSSCs, semiconductor material groups such as TiO_2, ZnO, SnO_2, Nb_2O_5, WO_3, Ta_2O_5, CdSe, CdTe, and CdS can be utilized as electron transport materials on the conductive substrate [25-30]. Due to its low cost, abundance, non-toxic components, and exceptional features such as biocompatibility, TiO_2 is the best candidate for DSSCs. Desilvestro demonstrated in 1985 that the power conversion efficiency of DSSC can be significantly improved by using TiO_2 nanoparticles [31, 32]. Until Grätzel utilized porous TiO_2 as the anode material, the efficiency of DSSCs did not surpass 1%. TiO_2 special characteristics make it the chosen semiconductor material for DSSCs. The edge of the conduction band is just below the excited state energy level of a number of dyes, which is one of the criteria for efficient electron injection. In the painting and cosmetics industries, TiO_2 is a white pigment, and it can be utilized in the electronics sector as a gate insulator in microelectronic devices and as a photocatalyst in architecture to create self-cleaning surfaces.

A colloidal solution (or paste) of TiO_2 is prepared and coated on clear conductive oxide glass, followed by sintering at 450-500°C to produce a TiO_2 thin film photoelectrode. This procedure produces a 10-20 μm thick TiO_2 film. The film has a nanoporous structure with TiO_2 nanoparticles ranging in size from 10 to 30 nm on average. Consequently, because of this porous structure, the actual surface area of the TiO_2 sheet is greater than its apparent surface area. Because this structure is so porous, the amount of dye that sticks to the surface will increase by a lot.

The anatase phase of titanium dioxide (TiO_2) is characterized by a large band gap, a high surface area, a large pore diameter, and transparency. Because the dye loading will provide more area for adsorption, the increased surface area will contribute to an improvement in the J_{SC} value. It raises the Fermi level and increases the value of the V_{OC} in DSSCs, which results in increased electron concentration in the conduction

band [33]. Investigations, on the other hand, have shown that DSSCs based on ZnO and SnO_2 are less effective than those based on TiO_2 [34, 35].

2.4.3 Dye as the photosensitizer

TiO_2 has a wide band gap, therefore it absorbs light with wavelengths longer than 370-390 nm. However, dye molecules covalently bonded to the TiO_2 surface serve as antennas to absorb as much of the solar spectrum as possible before it reaches the ground. Photons with energies greater than the HOMO level of the utilized paint are absorbed, allowing for a more rapid conversion of incident light into a current. There are a few things to keep in mind when picking out paint, and if we make a list,

- The dye must have a sufficiently extended excited-state lifetime to allow for effective electron injection.
- To enhance chemical bonding with the semiconductor surface and potentially operate as bridges for electron injection, paint requires connecting groups (-carboxyl, -phosphate, -sulfite, etc.).
- It's important that the electrolyte redox doesn't take the dye away from the electrode, so it must be soluble in something.
- Optimal solar energy collection requires that the dye have a broad absorption range.
- The excited state of the dye needs to be located energetically above the conduction band edge of the semiconductor to ensure rapid electron injection. The photosensitizer has to hold up well under the sun's light and in an electrolyte without losing any of its chemical, thermal, or electrochemical properties.
- The extinction coefficient of the sensitizer needs to be high across its whole absorption spectrum if it is to absorb the majority of the light while using the least amount of dye possible.
- It is necessary for the oxidized dye to have a higher potential than the redox couple in the electrolyte to prevent the injected electron from recombining with the oxidized dye. But the redox potential of the electrolyte is very important because it sets the potential of the counter electrode and, in turn,

the photovoltage of the cell.

A DSSC utilizes both organic and inorganic dyes. Natural and synthetic organic dyes are examples of the former, while inorganic dyes include metals like Ruthenium (Ru) and Osmium (Os) polypyridyl complexes, metal complexes like metal porphyrin phthalocyanine, and inorganic quantum dots. It's well known that natural dyes can be used as a cheap replacement for DSSC made from inorganic materials. From red to purple, natural dyes can be found in the plant's fruit, flowers, and leaves, all of which can be easily removed using standard techniques and put to use in the manufacture of DSSC.

2.4.4 Redox mediator

By allowing the transmission of charge between the photoanode and counter electrodes, the electrolyte is essential to the operation of the DSSC. The electrolyte's function is to revive the oxidized paint. Dye is used to transform light into electricity, which results in the loss of electrons and the acquisition of a positive charge. The cycle can be repeated because the electrolyte regenerates while holding the electron to the dye. To achieve this, it moves the positive charge to the counter electrode, where a returning electron from the external circuit regenerates the redox pair. Equations (2.1) and (2.2) depict the processes in the electrolyte [36].

$$I_3^- + 2e^- \rightarrow 3I^- \tag{2.1}$$

$$3I^- \rightarrow I_3 + 2e^- \tag{2.2}$$

Both the liquid and solid states of the conducting electrolyte, which contains various ions and is where oxidation and reduction take place, may be found. The electrolyte must, however, possess the following characteristics:

- For reduction to take place, the electrochemical potential of the redox pair must be lower than that of the dye that has been oxidized.
- Since the open-circuit voltage relies on the potential of the counter electrode

and subsequently the electrolyte, the redox potential should be as positive as possible.

- The redox pair should not react at the TiO_2 electrode but be reversible at the counter electrode.
- The visible spectrum should not be considerably absorbed by the electrolyte. because it has the potential to decrease the creation of dye-sensitive photos.
- The electrolyte must exhibit long-term resistance to chemicals, heat, and electrochemistry. Corrosive elements in the electrolyte may harm the electrodes and make working conditions worse.
- The charge carriers need to be highly ionic conductive and have quick diffusion in order to produce a high dye regeneration process. This is supported by the electrolyte's low viscosity.

Acetonitrile solutions containing the triiodide/iodide redox couple are the most often utilized electrolyte in high-throughput DSSCs [37]. TCO-glass, however, may be extensively corroded by it, which leads to poor long-term stability [38, 39].

2.4.5 Counter electrode

Another important element of the DSSC, which reduces the mediator, is the counter electrode. To return electrons from the external circuit to the redox electrolyte, the counter electrode's function is to transfer them. In order to reduce the redox pair, it must be a good conductor and show a low overvoltage. The following characteristics are sought for an optimal counter-electrode material to be employed in DSSCs [40]:

- High catalytic activity: To facilitate quicker cell regeneration, it should have high catalytic activity against ionic electrolytes.
- High conductivity: A counter electrode's electrical conductivity is also significant. High catalytic activity and low charge transfer resistance satisfy expectations.
- High optical reflectivity: To maximize the use of light, high optical reflectivity is necessary. Back reflection toward the dye molecules raises Jsc just before the light exits the cell.
- Cost savings,

- High surface area: The counter electrode is anticipated to have a high surface area, which translates to greater catalytic activity, similar to the photoanode component. The likelihood of electron regeneration increases with the number of active sites.
- The best thickness
- Chemical, electrochemical, and mechanical stability: The counter electrode must be able to tolerate chemicals, particularly those found in the electrolyte.
- Corrosion protection,
- Corrosion protection, energy level corresponding to the potential of the redox double electrolyte.
- Effective adherence to the surface of transparent conductive glass: The film's ability to stick to the glass's surface is crucial. If not, it may start to come off or break down in the electrolyte, which would be bad for the device.

Use of ITO or FTO glasses alone results in a very sluggish reduction reaction [41, 42]. In order to reduce the charge transfer overvoltage and speed up the response, transparent conductive glasses' surfaces are coated. Pt has the benefit of having a high catalytic activity for the iodide/triiodide redox process, which is why it is most often utilized as a counter electrode. Pt, however, is a pricey component. Low-cost cell manufacture requires a Pt coating of just a few nanometers, and bidirectional light-receiving may be achieved with Pt-coated electrodes since the thin Pt layer is almost transparent. High temperature stability, strong electrical and thermal conductivity, high optical transmittance, low charge transfer resistance, high corrosion, etc. are only a few of the significant properties of platinum [40]. A very thin coating of gold may sometimes aid in increasing fill rates. Recently, none of these materials have been able to match the yields of platinum.

2.5 Working Principle of a Typical DSSCs

The diagram in Figure 2.4 lays out a straightforward explanation of the DSSC as a working concept. The key concept is to combine dye-sensitizers with semiconductors to imitate the natural light-harvesting mechanisms in photosynthesis by decoupling the light absorption process from the charge collection process. In an ideal DSSC, the

photocurrent production cycle consists of six phases. In fact, there are undesirable occurrences that diminish the device's overall effectiveness. The processes conducted during the operation of the cell are illustrated in Figure 2.4 and briefly detailed below.

$$S + h\nu \rightarrow S^* \tag{2.3}$$

$$S^* \rightarrow S + h\nu \tag{2.4}$$

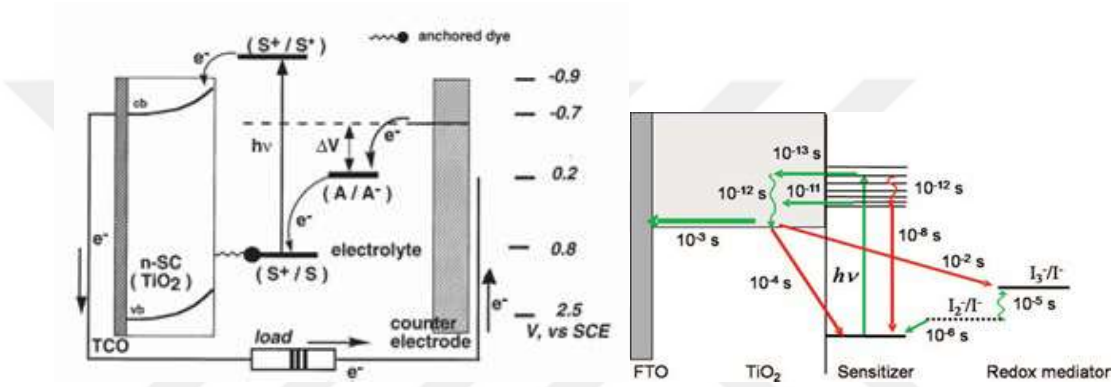


Figure 2.4 a) A schematic of the working principle of dye-sensitized electrochemical photovoltaic cells [43] b) The kinetic data for the different electron transfer processes taking place at the oxide/dye/electrolyte (TiO_2/Ru-sensitizer/iodide-triiodide) interface for DSSC under working conditions (Standard 1 Sun) [44]

2.5.1 Design of test specimens

As was said earlier, the monolayer of the dye that has been grafted onto the semiconductor surface contributes to the absorption of most of the solar spectrum that reaches the surface of the Earth. The molecule in its ground state (S) absorbs [17] a photon with energy, which elevates it to a state of excitement (S^*) (Equation 2.5). Relaxation [45] to the ground vibrational state has the potential to dissipate the extra energy (10^{-12} s), after which it would be emitted [46] (fluorescence 10^{-8} s - or phosphorescence, when there is inter-system crossing involved) (Equation 2.5). The production of electrons in the conduction band of the semiconductor is not helped by these activities in any way.

$$S^* \rightarrow S^+ + e_{cb}^- \tag{2.5}$$

2.5.2 Electron injection

On the femtosecond timescale, one of the fastest known physical events [47] takes place: the injection of electrons [18] from the excited state of the dye molecule into the conduction band of the semiconductor (Equation 2.5). It is at this point that the charge separation occurs, making it a key stage. In most cases, the dyes are created in such a manner that the process can be quantified. This is accomplished by positioning the LUMO of the dye in such a way that it lies sufficiently high above the edge of the conduction band. It is possible to change the position of the conduction band edge by either the local adsorption of certain species (for example, tert-butyl pyridine, which is responsible for the shift in the upward direction) or the intercalation of very small cations, such as Li^+.

2.5.3 Electron transport

For the injected electrons to reach the external contact, they must first traverse the mesoporous network. The thickness of the film is between 3 and 12–15 μm, but the charge must travel a much longer distance because the mesoporous network of nanocrystallites makes the path twisted. Since electrons are charged molecules, it makes sense that the electric field gradient is the main way they move. However, the ions in the electrolyte around the particles hide the electric field, so it is said that electrons that are connected to these ions go through ambipolar diffusion. Further, the presence of electron traps within the band gap—the electrons encounter several trapping and de-trapping processes - increases the time spent in the film before being removed. Transport occurs on a timescale of milliseconds to sub-milliseconds.

$$2S^+ + 3I^- \rightarrow 2\mathrm{S}{+}\mathrm{I}_3^- \tag{2.6}$$

2.5.4 Reduction of the redox mediator

Counter-electrodes [48] collect electrons from the external circuit [49] and use them to reduce the oxidized form of the redox mediator (Equation 2.7). Ions move slowly toward the electrode via diffusion. The hopping Grotthus-like mechanism [49], in which chemical bonds in the momentarily formed associates are established and broken, is only capable of enhancing transport in a viscous media with a significant concentration of the redox species. This would include an ionic liquid or gel electrolyte. When an oxidized substance reaches the counter-electrode, it is converted back to its reduced form. Putting a catalyst on the counter-electrode surface should speed up the process.

$$2e_{cb}^{-} + I_3^{-} \rightarrow 3I^{-} \tag{2.7}$$

$$e_{cb}^{-} + S^{+} \rightarrow S \tag{2.8}$$

2.5.5 Electron recombination

Recombination of electrons with oxidized redox species in the electrolyte [49, 50] and, much less frequently, with oxidized dye molecules [51] can both significantly impede DSSC performance. Even in high-efficiency cells, it is thought that around 10% of supplied electrons readily recombine with the electrolyte (Equation 2.7). A lower output voltage is the direct consequence of this because the quasi-Fermi level is determined by the number of electrons in the trap states and the conduction band. The production of radicals or the engagement of molecule I_2 in a multistep process have both been hypothesized as possible mechanisms for the reaction, although neither has been definitively proven [52, 53]. Electrolyte recombination happens in a time frame like electron transport, but it must be significantly slower than transport to get a high-performance device. Since 1-electron cobalt complexes undergo a quick reaction, it is imperative that this process be blocked as effectively as possible. This is achieved by including bulky complexes (to impede diffusion on the TiO_2 surface) and inserting the shielding groups on the dye molecules.

Because most dye molecules are designed to allow for efficient charge separation, the second recombination channel is rarely seen in devices. In many cases, dye regeneration via the electrolyte is outcompeted by recombination with the dye (Equation 2.8), also known as geminate recombination, making it essential to have carefully thought-out designs for dye molecules (the distribution of the electron cloud).

2.6 The Fundamental Manufacturing Processes Utilized by DSSCs

Multiple parameters, including production volume, size, shape complexity, capital investment, production flexibility, energy demand, the human factor, etc., influence the selection of the optimal manufacturing technique for DSSC. The manufacturing process that is chosen has a significant impact on the final product in terms of its characteristics. Some production techniques are illustrated in Figure 2.5. A comparison of the spin coating technique and the doctor blade approach has been carried out, and the researchers have reached the conclusion that the doctor blade technique is superior to the spin coating technique because of its inexpensive capital investment, easy operation, reduced material wastage, and rapid production rate [54, 55]. Despite the many benefits, it offers in comparison to spin coating, it does have a few drawbacks, the most notable of which are its low particle concentration and low evaporation rate. Design and selection of fabrication methods are always a compromise between qualities and cost, so it is crucial to have a thorough understanding of numerous kinds of processes [54, 56].

In this section, basic information regarding production techniques will be presented, followed by a discussion of the methods employed in the thesis.

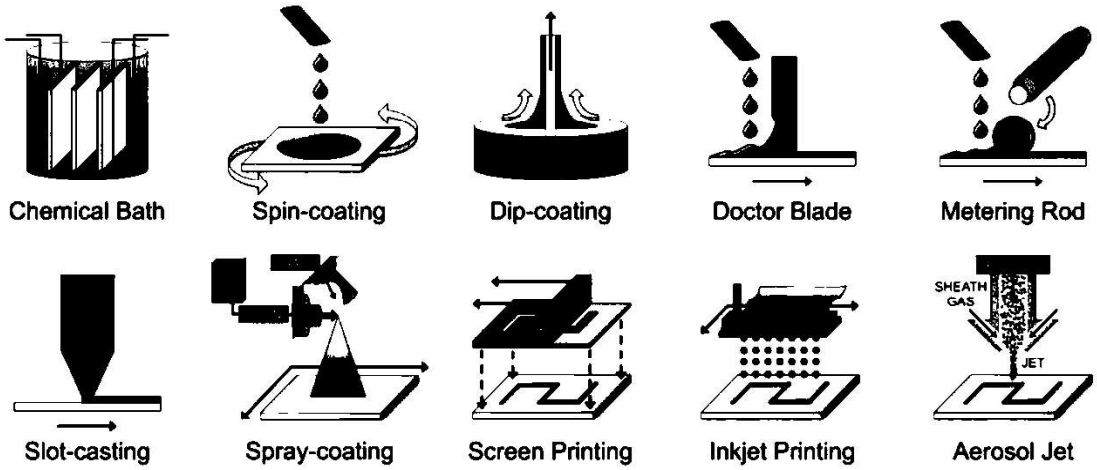


Figure 2.5 Some production techniques used for DSSC.

2.6.1 Spin Coating

Centrifugal forces are utilized in the spin coating procedure in order to deposit the needed material onto the substrate [54, 57]. In most cases, a substrate that has been cleaned is maintained on the chunk of the spin coating machine. It does this by producing a vacuum beneath the substrate, which fixes it in place and enables high-speed rotation of the substrate.

On the rotating substrate, the solution and/or suspension of nanoparticles are carefully placed, drop by drop. The solution tends to spread out over the substrate and completely cover it because of the high centrifugal forces. Figure 2.5 provides an illustration of a schematic representation of the spin coating procedure. The following steps are involved in the process of spin coating:

- deposition,
- spin up,
- spinoff,
- evaporation.

The overloaded solution is deposited onto the revolving substrate, and then, after the solution has completely evaporated, a thin coating of nanoparticles is left behind. It is possible to manufacture layers with a thickness that ranges from nanometers (nm) to millimeters (mm) by employing this coating method [58]. It is essential to keep the

following factors in mind when carrying out a spin coating process: volume of dropped solution, spinning speed, spin time, viscosity, acceleration time, and solution concentration. Spin-coating technique has advantages such as a film thickness that can be adjusted, uniformity, low operating costs, and practicality, among other benefits.

2.6.2 Doctor Blading

Tape casting is a relatively new method that was initially developed in the 1940s as a means of producing thin layers of piezoelectric materials and capacitors. This was the first application of the process. It is also known as tape casting, and it is the coating technique that is most utilized for the manufacture of lab scale DSSCs [57]. This is likely owing to the fact that it has a low cost, an extremely straightforward operation, and fewer moving parts than other techniques. Amateurs have been known to employ it on occasion because it is both adaptable and economical. A stage, on which the substrate is stored, a sharp moving blade, and a few different fixtures make up this piece of equipment. The substrate is then positioned on the stage, and each blade is then positioned on the substrate with the needed amount of space between each blade. This space is ultimately what determines the thickness of the coating. On the substrate, a paste containing the necessary nanoparticles is dropped, and then the paste is distributed using a sharp blade. This technique can be carried out numerous times in order to build up a layered structure or enhance the material's thickness. The flowchart of the process can be found in Figure 2.5.

After dropping a paste consisting of nanoparticles onto the substrate, the blade is pushed back and forth in order to spread the material out evenly. Following the completion of the uniform spreading step, the substrate is removed from the stage in preparation for the drying step that comes next. This technique can also be used to manufacture films for a variety of devices, including perovskite solar cells (PSCs), organic solar cells (OSCs) and dye-sensitized solar cells [59, 60]. The Doctor-Blade Technique is suited for coatings with a broad range of wet film thicknesses between 10 and a few hundred micrometers and can cover up to a few meters per minute. Large-scale productions are made possible in this circumstance.

2.6.3 Chemical bath deposition

Chemical bath deposition, also known as CBD, is said to be the oldest known process for the creation of thin films using a chemical solution. It dates back to 1884, when PbS was deposited using thiourea as the solvent. In its most simple form, it requires the use of heating and stirring equipment in addition to solution containers and substrate holding fixtures. In other words, it can't be done without these things. In most cases, the precursor solution is heated and mixed after the substrate is initially submerged in it. After the hydrolysis step, the solution is then heated again before being mixed. Particles begin to nucleate and develop near the surface of the substrate, which is also where the process begins. In order to comply with the CBD requirements, the sum of the concentrations of the metal ions and the chalcogenide must be greater than the solubility of the end product. Therefore, the availability of the reactants in the solution is the primary factor that determines the maximum thickness that can be achieved. Complex management of the solution's composition, pH, and temperature is required in order to achieve the desired control over the film's thickness, morphology, composition, and density. Using this method, one may finally generate films that are consistent throughout, homogeneous throughout, and adherent throughout, all while having good repeatability (See Figure 2.6).

The production of a wide variety of metal-oxide materials has been accomplished with the help of this technology. In particular, LPD silica has found application in the field of semiconductor technology as well as in other fields, such as solar cells [61].

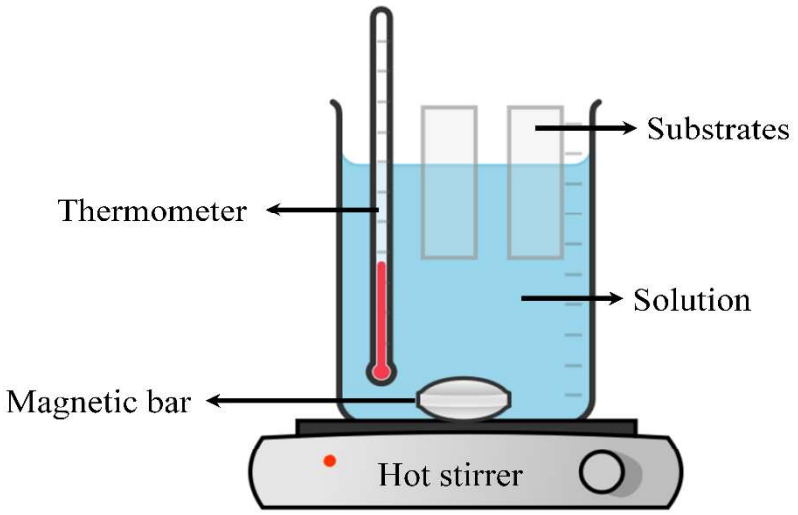


Figure 2.6 Schematic of chemical bath deposition technique [61]

2.6.4 Template method

The template method is not really a coating technique; rather, it is a process that offers a structure, texture, or platform that may be removed and then the appropriate material can be put on top of that. After the required material has been successfully deposited, the template can be eliminated either by heating it or by leaching it with acid. The desired nanostructure can be fabricated on the substrate using this approach, which is an advantage.

2.6.5 Realizing the Limits of Dye-Sensitized Solar Cells

Standards for DSSCs have evolved over the decades following the early researchers' efforts in the last century. Collaborative research efforts have led to the creation of low-temperature (≤150°C) technologies based on cheap materials, despite theoretical estimations promising power conversion efficiency of up to 20%. Power conversion efficiency has significantly increased over the past ten years because of a better understanding of the functional limitations of DSSC components. In this section, the fundamental understanding and breakthroughs related to components such as the electron-transporting anode, light-absorbing dye sensitizers, redox mediators, and hole-transporting materials are described. These components are essential to the operation of the solar cell.

Extrinsic and intrinsic energy losses are the two most significant types of energy loss that can occur in solar cells. For instance, series resistance and recombination losses are two types of losses that fall under the first category, which refers to losses that, in theory, may be avoided and, as a result, aren't considered when talking about basic constraints. Even with perfect cell design and material optimization, solar cells still experience some amount of loss due to the physics of solar cells.

Intrinsic losses can be caused by five basic factors. Only photons with an energy greater than Eg will be transformed into an electron-hole pair when light interacts with the absorber in a solar cell. This happens because photons with lower energies are not able to interact with the photo absorber. This indicates that all photons that do not fulfill these requirements will be lost as a result of the device's transmission of them. In addition, photons with energies that are higher than the bandgap will produce what are known as "hot carriers," which are pairs of electrons and holes that have a significant amount of energy.

As these heated carriers cool off and move closer to the edge of the conduction band, this surplus of energy will be dissipated through a process called thermalization. This relaxing process offers an additional source of solar cell efficiency-reducing losses. The third intrinsic loss results from Kirchhoff's law, which stipulates that at equilibrium temperature, the absorptivity and emissivity of a body are identical [62]. These emission losses can be predicted using the following application of the Plank equation [63]:

$$F(\mathrm{E},\mathrm{T},\mu,\Omega)=\frac{2\Omega E^2}{c^2h^3\left(exp\left(\frac{E-\mu}{k_BT}\right)-1\right)} \tag{2.9}$$

where μ is the chemical potential and Ω, the solid angle of the emitting surface. The second source of losses is the transfer of heat between the sun and the atmosphere, which is referred to as the Carnot loss. Similarly, in a Carnot engine, in order to maintain energy balance, work must be lost. The Carnot engine in this instance would be the solar cell. Performance-wise, these losses degrade the V_{OC}. The final

contribution comes from an anisotropic redistribution of the photons that have been emitted in relation to the flux that has been absorbed. This entropic phenomenon is referred to as Boltzmann loss.

A case study is shown in Table 2.1 below [64], in which a solar cell with an E_g value of 1.31 eV is primarily hindered by photon losses of 25% and thermalization losses of 30%. As a means of improving the PCE, several potential solutions are currently being investigated. Examples of this include multijunction solar cells, which help cut down on photon losses, as well as multi-exciton solar cells and hot carrier solar cells, which address the issue of thermalization losses [65].

Table 2.1 Estimated PCE and loss efficiencies for a device with Eg=1.31 eV

	PCE	Photon loss	Thermalization	Boltzmann	Carnot	Emission
η (%)	33	25	30	9	2	1

2.7 Literature Review

As illustrated in Figure 2.7, each subsystem contributes positively to the cell's performance. As a result, in order to propel synergistic effort, each subsystem have to be solely improvised and well coupled by mechanically, chemically, and electrically. At first look, it appears that traditional TCO needs to be replaced in order to boost sheet resistance, which is ultimately responsible for the prevention of FF. The utilization of 2D materials is therefore a potential solution to the difficulty. Next subsystem blocking layer has the potential to be qualitatively satisfied by optimal doping that is applied using the electrospinning approach Further research demonstrated that anatase TiO_2 crystal facet control is important for successful molecular interaction. Optimized heterostructures inserted into a TiO_2 network have always exhibited promising properties for establishing a scattering effect, recombination resistance, and electron injection medium with greater efficiency. By utilizing unique 2D materials and quantum dots, additional tests should be conducted to simultaneously fulfill high specific surface, light scattering effect, efficient

electron transport, and decreased recombination rate. Utilizing bacterial pigments, numerous efforts have been done to create green solar cells. However, more research is required to uncover the presence of functional groups recognized for efficient coupling with TiO_2 in these pigments. Moreover, their connectedness could be enhanced by combining dye additives or by integrating natural co-adsorbents. Despite having a strong ionic conductivity, liquid electrolytes are always suspect for cell deterioration, stability, and durability [66]. As a result, the development of a solid-state electrolyte based on biodegradable promising materials has gained speed. In addition, biopolymers derived from living organisms, such as starch, chitosan, carrageenan, agarose, and cellulose, have garnered exponential interest in the production of green quasi-solid-state electrolytes. The catalytic activity of the counter electrode fundamentally requires hybrid architectures that were tuned. Finally, the outcome of our study encourages further research for the development of environmentally friendly solar cells, for which various chances exist in each subsystem for the construction of an eco-friendly ecosystem.

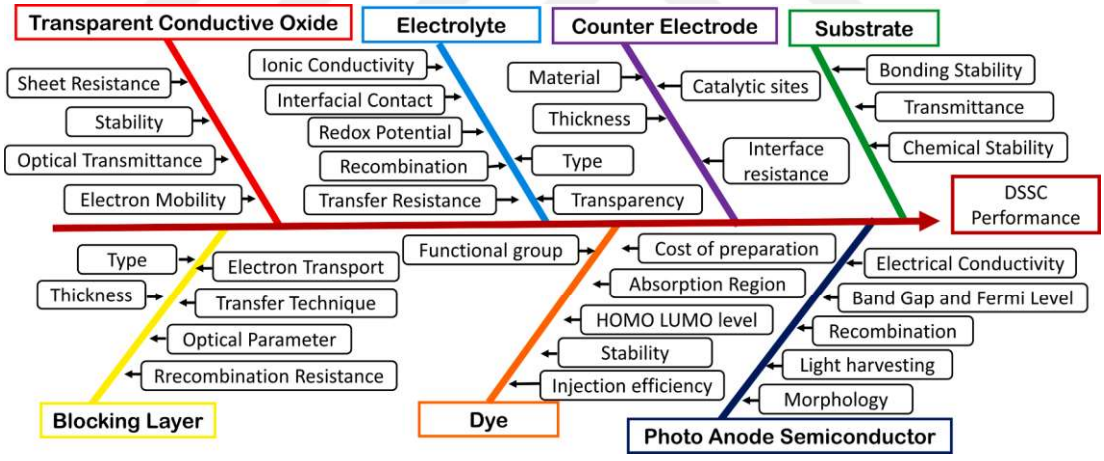


Figure 2.7 Fishbone diagram for DSSC performance enable research scope at various levels [67].

2.7.1 An Ideal Blocking Layer for DSSCs

The ideal blocking layer should cover the entire surface of the FTO and TiO_2 to prevent recombination, however, should not prevent electron injection [68, 69]). Blocking layer's thickness is significant because it may impede electron injection, therefore outweighing the impact of lowering recombination or increasing the cell's

voltage due to an increase in the conduction band [70].The slower recombination kinetics skew the rivalry between electron transport and recombination in favor of electron transport, leading in improved charge collection [68, 69]. Various defects can take place on the surface of the TiO_2 nanoparticles due to the presence of oxygen vacancies, bridge-bonded oxygen, hydroxyl groups, and fivefold coordinated Ti atoms [71, 72]. $TiCl_4$ treatment has been proven by photoluminescence studies to decrease these. The $TiCl_4$ treatment causes a 100 mV positive shift in the TiO_2 conduction band. This has the consequence of decreasing the voltage despite the decreased recombination, while boosting the injection efficiency as a result of the increased driving force from the dye LUMO to the TiO_2 conduction band. The outcome is a film coated with $TiCl_4$ that has a reduced V_{OC} but a much bigger J_{SC} and a greater total power conversion efficiency [73]. $TiCl_4$ treatment has important effects on recombination and surface electric field, and possibly some effect on transport [74].

By comparing the behavior of Al_2O_3-coated substrates with and without $TiCl_4$ treatment, we gain insight into $TiCl_4$'s mechanism of action. Thick TiO_2 substrates are used to probe the effect of lengthened electron collection distances, and our results indicate that even when the active layer thickness is doubled, recombination is not significantly exacerbated, and high device efficiencies are possible [75].

2.7.2 Effect of TiO_2 nanoparticle characteristics

In addition to the dye's light absorption and chemical stability, the qualities of TiO_2 nanopowders play a major role in the performance of TiO_2 photoanodes. Particle size and morphology [76-78], crystallinity [79, 80], phase content [79, 80], band gap [78], chemical composition (doping) [81], and surface groups [82, 83] are just a few of these properties that have been studied in depth and have been shown to be important for DSSC efficiency. For the semiconductor film to have a high surface area (to maximize dye loading) and an average porosity in the mesopore range (2-50 nm average pore size), the particle size and particle size distribution must first be balanced. This will allow for the diffusion of dye and electrolyte in the

semiconductor film. Miranda et al. reported that the overall performance of DSSC devices was optimized with photoanodes produced from powders with bimodal crystal size distribution consisting of two nanocrystal classes, 5 and 50-100 nm in size, by contrasting the overall performance of DSSC devices with photoanodes based on powders with single-mode crystal size [84]. Additionally, since it directly affects the bandgap [78] and electron diffusion length [85] of the film, particle size has to be carefully taken into account. On the one hand, the bandgap of TiO_2 nanocrystals is known to grow with decreasing average crystal size, offering the possibility of raising the open-circuit voltage in DSSC devices. On the contrary, Nakade et al. [85] discovered that using tiny nanoparticles had a negative impact on the duration of recombination and the diffusion length of electrons. Second, critical characteristics of TiO_2 powders that are known to influence DSSC effectiveness include crystal grade and phase composition. TiO_2 particles' strong crystallinity encourages electron transport while minimizing charge recombination losses. Due to its wider band gap, pure crystal anatase nanoparticles are often selected for DSSC applications. However, Li et al. recently discovered that anatase nanoparticles' total solar conversion efficiency and light collecting efficiency were both greatly increased by the addition of 10-15% rutile nanoparticles [79]. Finally, considerable research has been done on the impacts of the mass and surface chemical composition of TiO_2 nanoparticles. Ko et al. showed improved performance of DSSCs combined with W and/or Al-doped TiO_2 nanoparticles as a result of electrical surface state alterations brought on by metal ion additions [81]. A better photocurrent may result from the presence of hydroxyl surface groups (Ti-OH) owing to an enhanced dye adsorption process on TiO_2 nanoparticles, according to recent research [82, 83].

2.7.3 Impact of the paste's composition

The creation of TiO_2, mesoporous thin films with high homogeneity, porosity, and mechanical qualities depend in large part on the paste formulation [86-88]. TiO_2 nano powders that have already been dispersed in a solvent are often combined with a binder and a rheological agent to create screen printing paste. Once a proper viscosity and TiO_2 concentration are attained, the resultant mixture is further concentrated by evaporation. Each component of the paste has a distinct purpose.

The voids between the particles are created by the binder. It also has a significant impact on the sintering process because it changes the film's viscoelastic characteristics, which in turn alter the sintered film's ultimate strength, porosity (density), and topological structure [89, 90]. Typically, too much binder will make the film difficult to adhere to the substrate, while not enough binder will cause the film to fracture. The rheological agent influences both the viscosity and particle dispersion of the paste [86]. Adding more surfactants will improve the paste's steric stability and reduce particle aggregation, resulting in greater particle dispersion [91, 92]. To date, most studies have used ethanol as a solvent, α-terpineol as a rheological agent, and polyethylene glycol (PEG) or ethyl cellulose as a binder [20, 21, 23, 24, 86, 90, 92-97]. Few studies have been done [88] on making water-based pastes, which are better for large-scale manufacturing, contain fewer chemicals, and are more ecologically friendly [87, 98].

2.7.4 Effect of the structure of the film

Numerous research teams have also looked at ways to optimize the film's thickness and structure [77, 92, 99]. To ensure that the greatest number of electrons injected into the CB of TiO_2 may reach the conductive surface of the anode, the ideal thickness of the film should be less than the electron diffusion length. There is no optimum layer thickness since electron lifespan or diffusion length depend onfactors like TiO_2 particle size and shape. For instance, Lao et al. [98] discovered that 6 nm is the best film thickness for photoanodes prepared with an average particle size of 10 nm, while Ito et al. [99] reported that the best light-to-current conversion efficiency results were obtained for 12-14 nm TiO_2 films prepared with an average particle size of 20 nm. The performance of DSSCs is significantly influenced by the film's structure. The photocurrent of DSSCs has been observed to rise with the addition of a scattering overlayer comprising bigger diameter (150-500 nm) TiO_2 particles onto the transparent layer [99, 100]. The purpose of the scattering layer is to increase the photoanode's capacity for light absorption by allowing incoming photons to pass through the transparent layer without being absorbed by the dye. The addition of a top layer with scattering centers, such as micro-voids, may also result in scattering effect [101].

2.7.5 The influence of sintering temperature profile and $TiCl_4$ post-treatment

Other manufacturing factors, including the sintering temperature profile and the addition of a $TiCl_4$ post treatment to the film, were shown to have a significant impact on the performance of DSSCs. Typically, sintering is accomplished by progressively raising the temperature [102]. Lee et al. [103] investigated the influence of sintering temperatures in the range of 400-600 °C and discovered that the overall cell efficiency was maximized for films sintered at 500 °C owing to particle necking. Above 500 °C, crystal growth occurred, which decreased the film's surface area and, therefore, the quantity of adsorbed dye, resulting in a smaller photocurrent. Often, the photocurrent of the cell is increased by treating the film with an aqueous solution of $TiCl_4$ [98, 103, 104]. Initially, it was thought that $TiCl_4$ post treatment improved particle necking via chemical sintering (the formation of a thin layer of Ti-oxo/-hydroxo species on the surface of the particles, which transforms into crystalline TiO_2 during sintering), thus improving electron conduction within the particle network [99]. Yip et al. showed that post-$TiCl_4$ treatment was responsible for an increase in the surface area of the film, which contradicts this idea [104]. In addition, Sommeling et al. hypothesized that the $TiCl_4$ post-treatment caused a change at the conduction band edge of TiO_2, resulting in a more efficient injection of electrons from the dye into TiO_2 [73].

CHAPTER 3

THEORETICAL CALCULATIONS

This section describes how the data obtained from the characterizations contribute to the evaluation of the film or device's performance in the light of theoretical knowledge.

3.1 XRD Analysis

Most crystal structures in solids are studied using X-ray diffraction, which is the most common diffraction technique. XRD is based on the notion of X-ray diffraction in a distinctive order, which is determined by the precise atomic sequences of each crystal phase. Each phase of a crystal can be identified by its unique diffraction profile. This approach is ideal for thin film examination for two primary reasons:

- X-rays are suitable to structural research because their wave lengths are determined at atomic distances in condensed materials.
- X-ray diffraction methods are nondestructive and have no effect on the studied material.

Atoms in a crystal structure scatter X-rays because of their parallel planes, which cause the rays to travel from the solid surface through the tiny incidence angles with complete reflection. The Bragg Law describes X-ray diffraction inside the crystal structure. In its simplest form, the Bragg Law says:

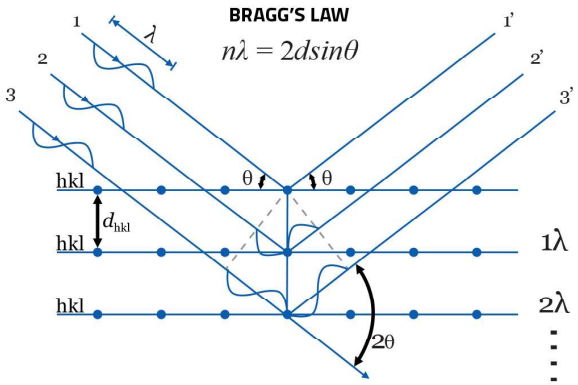


Figure 3.1 Bragg's law diagram

where λ is the wavelength of the radiation used, d is the inter-planar spacing involved, and θ is the angle between the incident (or diffracted) ray and the relevant crystal planes; n is an integer, referred to as the order of diffraction, and is often a unit.

The source releases X-rays that strike the crystal at an angle of θ, and the detector analyzes the dispersed radiation at a distance of 2θ from the source. The XRD operating principal diagram is seen in Figure 3.1 and 2. X-rays impact the atoms in the crystal plane, scattering the rays in various directions. For diffraction to be possible, scattered radiation must be consistent, with scattering being adaptable.

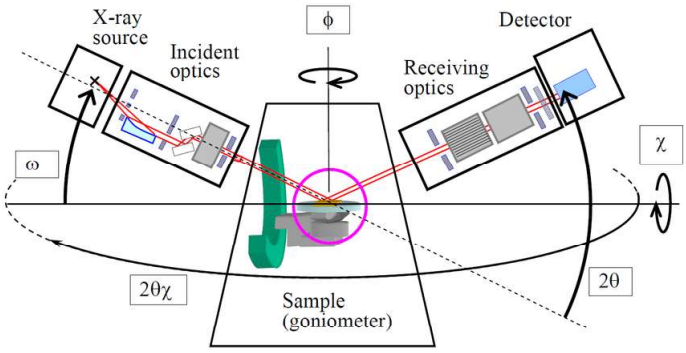


Figure 3.2 Working principle of X-ray diffraction (XRD)

The intensity of the diffuse rays is measured and marked based on 2θ, and the angle of the source varies in the relevant range depending on the location of the detector. There are many kinds of detectors. Using this plot of 2θ of the scattered, you can get

an XRD pattern. On a scale of 100, the point where the peak density is highest is changed, and the rest of the peaks are changed in the same way. The associated Miller indices are used to match the peaks to a certain group of lattice planes.

In this study, a Rigaku Miniflex 600 Tabletop Powder X-ray diffractometer was used with Cu anode material at 40 kV and 15 mA to look at the crystal structure of the photoanodes. With a step size of 0.02 °, the diffraction patterns were taken.



Figure 3.3 Rigaku Miniflex 600 XRD

3.2 AFM Analysis

Thin-film coatings of conductive glass doped with FTO and then doped with TiO_2 for use in DSSC sandwich fabrication are topologically characterized using AFM. AFM scans the surface of the sample using a cantilever and a very tiny needle at the tip. When the needle gets close enough to the surface, gravitational forces between the surface and the needle cause it to deflect toward the cantilever surface. As the needle approaches and contacts the surface, the thrust rises, and the console departs from it. Figure 3.4 depicts the operating principle of the AFM.

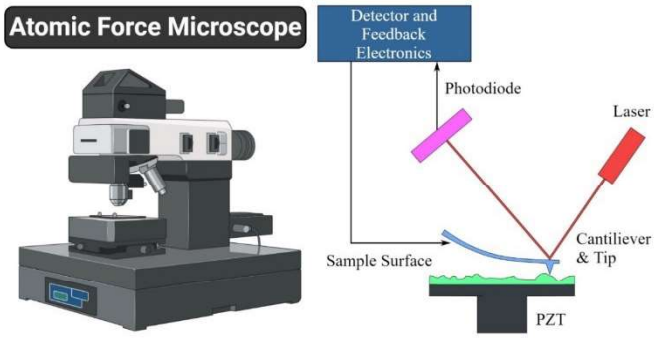


Figure 3.4 Working principle of AFM

The needle used in the probe's tip differs depending on the surface being studied. AFM operates in two modes based on the tip position: contact and non-contact. The contact mode may cause surface damage to the sample. In non-contact mode, when the tip is near enough to the surface, the AFM starts to oscillate at the resonance frequency and begins scanning the sample in the x-y direction with the help of a laser beam. The console's material reflects the laser beam. As the console moves, the reflected beam's angle varies. In addition, a position-sensitive photo diode is employed to detect these alterations. With these variations in the laser beam, nanoscale surface depressions and projections are recorded. In addition to analyzing the deviations from the laser beam, surface location information is also captured. The findings of the analysis are reminiscent of debossed maps. As with debossed maps, the nanosurface being studied is mapped based on differences in height at the same spot. The result is a topographic picture of the nanosurface. Figure 3.4 depicts an AFM from the Quesant Ambious Q-scope series that was used to measure a 5x5 μm^2 sample area.



Figure 3.5 Q-Scope™ 250AFM

3.3 SEM Analysis

SEM is a kind of electron microscope that employs a concentrated stream of electrons that react with the material to give a topological picture as well as a relative composition. When the concentrated beam of electrons comes into contact with the sample, it produces secondary electrons (SEs), backscattered electrons, and subsequently distinctive X-rays, which are recognized by various detectors and ultimately shown on the monitor. The main parts of a standard SEM are the electron source, the column that holds the electromagnetic lenses, the electron detector, the sample chamber, and the computer screen.

SEM image creation is primarily linked with the detection of signals resulting from interactions between electron signals and the scanned materials. In general, two kinds of interactions are possible: elastic and inelastic. After being hit by the main beam electrons, samples release SEs with low energies during the inelastic interaction (energy transfer to the atom in the sample). Conversely, elastic interaction comes

from the deflection of the main electron upon contact with the sample atomic nucleus or electrons of equivalent energy. The deflection of scattered electrons at an angle greater than 90 degrees is known as backscattered electrons (BSE) and may be employed for imaging samples. Figure 3.6 depicts the occurrence of SEs and BSEs.

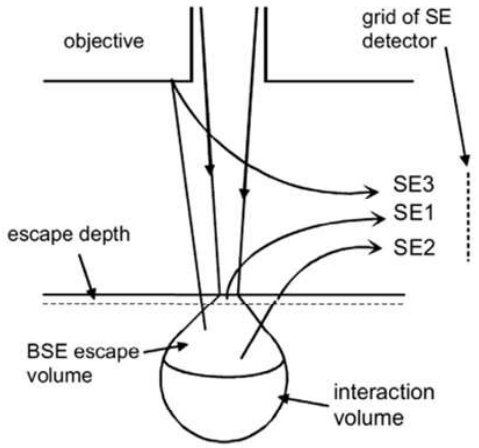


Figure 3.6 Interaction of the electron signal with the specimen upon contact. SE1 corresponds to secondary electron mode, while SE2 and SE3 are employed in back scattered [105]

SE mode is the most prevalent signal for SEM image processing. Due to the comparatively low energy of the incoming electrons, detection is only possible within a few nanometers of the sample's surface. Therefore, the topological contrast of a sample, such as its surface texture or roughness, may be accurately determined using SE. Notably, if SEs make it to the detector, only those that do will contribute to the final image, while blocked SEs will produce a low contrast image. In addition, the low-voltage electrons in the main beam will likely create SEs from the sample's uppermost surface, therefore precisely representing the sample's topographic details [105-107].

3.4 EDX Analysis

Utilizing scanning electron microscopy and EDX spectroscopy, the elemental composition of materials may be determined. At a concentration of at least 0.1%, EDX can identify elements with atomic numbers greater than those of boron. The EDX program can be used to evaluate and identify materials, identify contaminants,

analyze spots up to 10 cm in diameter, and scan for quality control, among other things.

In a normal SEM, materials engage with the electron beam and generate distinctive X-rays upon impact. Because no two atoms have the same X-ray emission spectrum, their concentration in a sample may be distinguished and quantified. The X-ray is produced when the mainstream of electrons interacts with the atom's nucleus. The main electron beam will excite the electron inside an atom's nucleus, removing it and generating an electron-hole. An electron from the atom's outer shell (with more energy) will replace the expelled electron, emitting unneeded X-rays. Figure 3.7 shows that the emitted X-rays are made up of the X-ray continuum, which is made when an electron slows down, and characteristic X-rays, which are made when electrons from the upper shell fill the electron hole in the core shell.

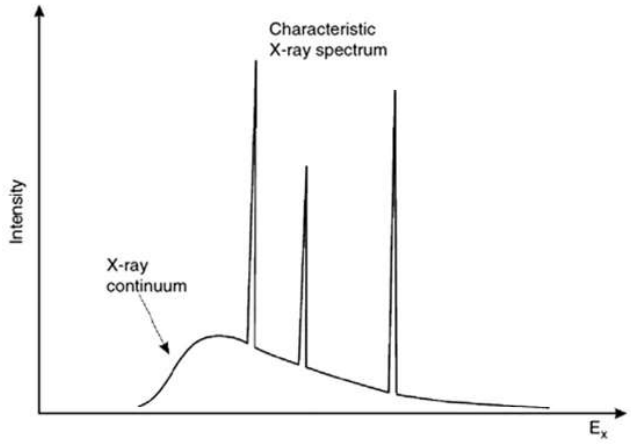


Figure 3.7 X-ray spectrum types shown schematically as a result of rapid electron bombardment [105]

X-ray continuity is not necessary for the identification of sample elements, but it must be detected to differentiate them. Factors such as the probe current, the accelerating voltage given, and the atomic number of the sample contribute to the intensity of the X-ray continuum. On the other side, the X-ray energy dispersion spectrometer will record the elemental composition measurement characteristic of the sample [105-108].

3.5 Transmittance and absorbance analysis

The transmittance of a surface or substance is the proportion of light that passes through to the opposite side of the surface. Light may be transmitted, reflected, or absorbed while passing through any surface or substance. The notions of transmittance and reflectance are closely connected. Transmittance is defined as the ratio of incident light intensity (I_0) to the quantity of incident light intensity that passes through an item (I). Transmittance is indicated by the letter T. I_0 is the incident light intensity. This light transmits through glass or any other substance. I is the light intensity that can flow through a substance. The transmittance is the intensity ratio. Consequently, the transmission has no unit.

$$T = \frac{I}{I_0} \tag{3.1}$$

The ratio of radiant flux transmitted by a surface (ϕ_t) to radiant flux received by that surface (ϕ_i) (T) is defined as transmittance. Therefore, the transmittance formula is;

$$T = \frac{\phi_t}{\phi_i} \tag{3.2}$$

Transmittance may be used to quantify the quantity of radiation absorbed. Beer-Lambert law (Beer's law) specifies the relationship between transmittance (T) and absorbance (A). According to Beer's Law, the formula for calculating absorbance is:

$$A = \log_{10} {}^{I_0}\!/_{I} \tag{3.3}$$

$$A = \log_{10} {}^{1}\!/_{T} \tag{3.4}$$

$$A = \log_{10} {}^{100}\!/_{T\%} \tag{3.5}$$

$$A = \log_{10}(100) - \log_{10}(\mathrm{T}\%) \tag{3.6}$$

$$A = 2 - \log_{10}(\mathrm{T}\%) \tag{3.7}$$

The transmittance of a substance measures the quantity of light that can flow through it. The definition of percentage transmittance is the proportion of light that can be transmitted from the opposite side of the surface. The formula for percentage transmittance (%T) is as follows:

$$T\% = 100T \tag{3.8}$$

The % transmittance number gives information on the surface or substance utilized in a variety of applications. If the percentage transmittance is high, the surface will allow more light to pass through. Similarly, if the % transmittance number is low, it indicates that the surface absorbs more light. For a fully transparent substance, 100 percent of light will flow through to the other side, and the material's transmittance is 100 percent. For a substance that is entirely opaque, light cannot penetrate through it. As a result, the transmittance is zero. Transparency is proportional to the substance's percentage transmittance; hence, a material with a high transmittance percentage is more transparent.

3.6 Figure of Merit

Transparent conductive coatings can be described in terms of their electrical and optical properties using the electrical sheet resistance R_{sh} and optical transmission T, respectively. Sheet resistance is given by:

$$R_{sh} = 1/\sigma t \tag{3.9}$$

where σ is the electrical conductivity in Ω^{-1} cm^{-1} and t is the coating thickness in cm. The dimension of R_s is customarily quoted in Ω /square to indicate that it measures

the resistance of a square surface area whereby the square area is independent of dimension and absolute value.

The optical transmission is given by the ratio of the radiation I_0 entering the coating on one side to the radiation I leaving the sample on the opposite side, so that

$$T = e^{\alpha t} \tag{3.10}$$

where α is the optical absorption coefficient measured in cm^{-1}. It has been proposed to define a figure of merit F_{TC} [109] by

$$\phi_{TC} = T^{10} / R_s \tag{3.11}$$

When their electrical sheet resistance and optical transmission are determined, the figure of merit φ_{TC} is a valuable tool for comparing the performance of transparent conductive coatings. In addition, the developed formulas for φ_{TC} may be used to estimate the transparent electrode qualities of a prospective material based on its basic parameters.

3.7 JV Analysis

Light is converted into electricity by solar cells. Solar cell performance is determined by short circuit current (I_{SC}, mA) and open circuit voltage (V_{OC}, V). J_{SC} (short-circuit current, $mAcm^{-2}$) may be calculated by dividing Isc by active area of cell. In a similar manner, the current Voc value is calculated from negative to positive. Figure 3.8 depicts Jsc against Voc. Pmax is the greatest conversion efficiency of DSSC to produce energy from sunlight. FF equals the ratio of maximum power output ($J_{max} \times V_{max}$) to product ($J_{SC} \times V_{OC}$).

$$FF = \frac{Area_B}{Area_A} = \frac{J_{mp} \times V_{mp}}{J_{sc} \times V_{oc}} \tag{3.12}$$

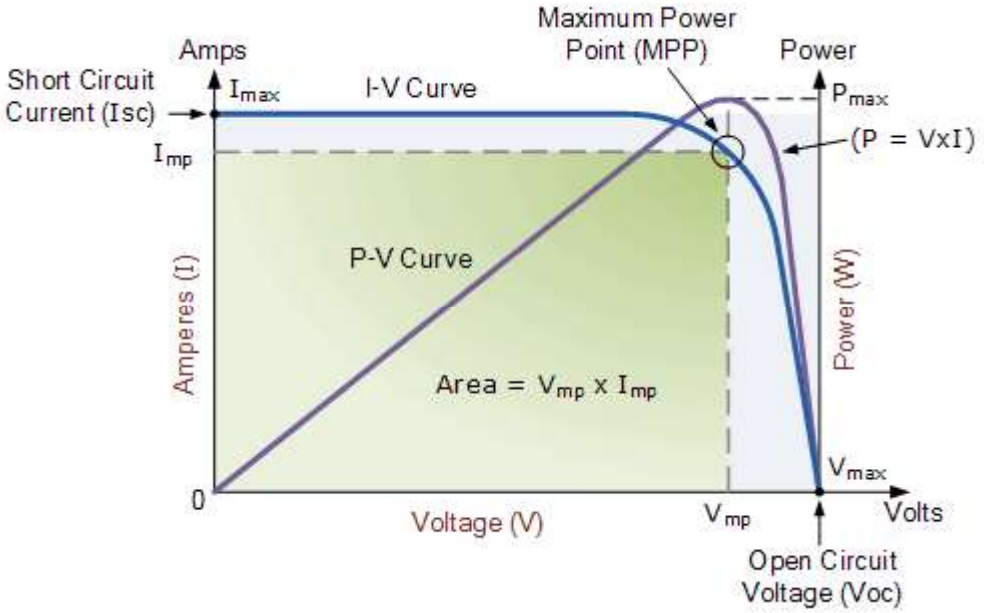


Figure 3.8 I-V curve to evaluate the cell performance [110]

In addition, the total efficiency (%) is the proportion of solar energy (which shines on a photovoltaic [PV] device) that is converted into electrical energy, where rises with decreasing J_{SC} value and increasing V_{OC}, FF, and molar dye coefficient values [110].

$$\eta(\%) = \frac{J_{SC} V_{OC} FF}{P_{in}} \tag{3.13}$$

External quantum efficiency (also known as IPCE) is the ratio of photons occurring at the cell surface at any wavelength (λ) to electrons flowing in the external circuit. The formula is as follows [111]:

$$IPCE\%(\lambda) = 1240 \times \frac{J_{SC}}{\lambda P_{in}} \tag{3.14}$$

3.8 EIS and Bode Analysis

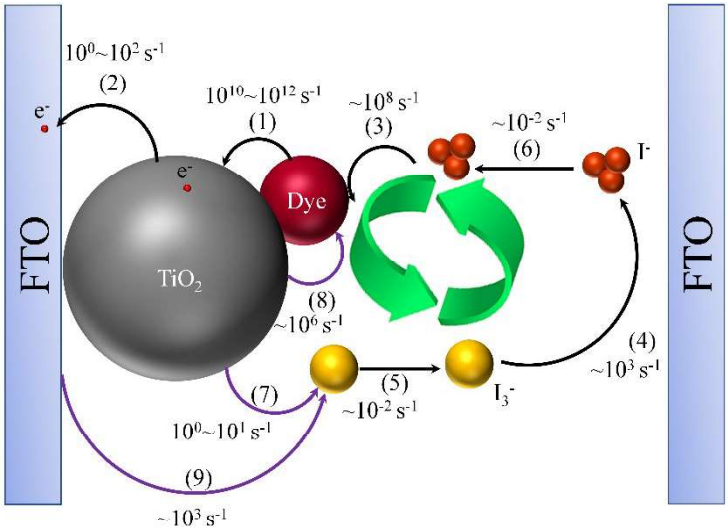


Figure 3.9 (a) Charge transfer kinetics involved in dye-sensitized solar cells where dark arrow shows loss mechanism: (1) injection of electrons, (2) diffusion of electrons in the TiO_2, (3) regeneration of dye, (4) regeneration of redox mediator (I_3^- / I^-), (5) diffusion of I_3^-, (6) diffusion of I^-, (7) back reaction of TiO_2 conduction band electrons with I_3^-, (8) recombination of electrons with oxidized dye, and (9) back reaction of electrons from FTO to I_3^- [112].

Figure 3.9 depicts the process involved in the charge transfer and electron loss mechanism of DSSC. Pathway (1) displays the electron injection process (see Equation.3.15-16). The performance of charge injection is determined by the energy gap between the dye's LUMO level (the lowest unoccupied molecular orbital) and the TiO_2 conduction band, as well as the capacity of the dye molecules tethered to the surface of the TiO_2 nanoparticles. These characteristics limit the timing of electron injection at the contact between the dye and TiO_2. Following the injection procedure, the electron is transported to the FTO glass through the diffusion process (2). The electron's capacity to diffuse inside the TiO_2 nanoparticle network is determined by the diffusion resistance given by the TiO_2 network, which is dependent on the electron recombination process occurring on the TiO_2 surface (TiO_2/electrolyte; T-E interface) or within the stack TiO_2. It may be assumed that

there are equal amounts of electrolyte ions (I_3^-/I^-) in solution. The triiodide redox electrolyte diffuses toward the oxidized dye molecules, regenerates them by route (3), and then self-oxidizes to the iodide ion (see Equation 3.17).

This dye reduction process raises the concentration gradient of iodide ions, which enhances their propensity to transport iodide towards the Pt-coated FTO glass, therefore reducing to create triiodide ions (route (4)) to sustain the kinetics of dye regeneration in the cell (see Equation 3.18). To maintain redox reactions in the cell, it is readily apparent that the electrolyte solution must include electrolyte ions with enhanced diffusion characteristics for pathways (6) and (5). In terms of electrical quantity, it follows that the electrolyte solution should offer electrolyte ions with a reduced diffusion resistance. Reduced diffusion resistance accelerates redox processes, hence facilitating regeneration of the redox mediator (I_3^-/I^-). By trapping electrons from the TiO_2 network through route (8), oxidized dye molecules may also be reduced, and this pathway can be termed the recombination pathway (see Equation 3.18). However, the primary electron loss process is electron capture by triiodide ions through route (7), which is influenced more by the kinetics of charge recombination at the TiO_2/electrolyte contact (see Equation 3.19). Charge recombination kinetics also governs charge recombination across the TiO_2/electrolyte interface, i.e., the greater the charge transfer barrier at the TiO_2/electrolyte interface, the lower the electron recombination through route (7), and vice versa. The preceding discussion demonstrates that the performance of DSSCs produced with different electrode thicknesses (L = 3μm-12μm) may be described in terms of the impedances in the stack and cell interface areas.

$$S_{dye} + h\nu \rightarrow S^* \tag{3.15}$$

$$S_{dye} \rightarrow S^*_{dye} + e^{TiO_2}_{cb} \tag{3.16}$$

$$S^+_{dye} + 3I^- \rightarrow 2S_{dye} + I_3^- \tag{3.17}$$

$$e_{Pt} + \frac{1}{2} I_3^- \rightarrow \frac{3}{2} I^- \tag{3.18}$$

By applying the AC input voltage V(ω,t), the EIS determines the current response as a function of frequency; hence, Nyquist plots often contain three semicircles (I-III) due to various charge management at the interface and inside the DSSC components. Typically, a DSSC comprises of a photosensitive dye adsorbed on an FTO glass substrate covered with a mesoporous layer of nanocrystalline TiO_2 serving as the working electrode, an I_3^-/I^- derived redox pair, and a Pt-FTO glass substrate serving as the counter electrode. The EIS has conducted substantial research on photo-electrochemical processes, particularly the electronic and ionic processes (diffusion and recombination) involved in DSSC.

$$S_{dye}^+ + e_{cb}^{TiO_2} \rightarrow S_{dye} \tag{3.19}$$

$$I_3^- + e_{cb}^{TiO_2} \rightarrow 3I^- \tag{3.20}$$

A suitable frequency distribution of several time constants for diverse charge transfer pathways (1-8 paths) results in three distinct arcs, as seen in Figure 3.10. (a), or three distinct peaks on the Bode plot of the EIS of a DSSC. (see Figure 3.10.(b)). These semicircles in the EIS spectrum have been attributed to the relevant charge transfer mechanisms using a theoretical and experimental method [113-117] Figure 3.10. (a) clearly illustrates the three semicircles. Moving in the direction of ω= 0 rad/s, the semicircle – I (about ω~ ∞ rad/s) reflects the charge transfer processes occurring at the Pt/electrolyte interface with the characteristic frequency CE. The second (II) or middle semicircle relates to electron transport in the TiO_2 film and electron return reaction with I_3^- at the TiO_2/electrolyte interface at the characteristic frequencies ωd and ωk, respectively. Lastly, the third (III) semicircle drawn close to the low frequency area represents the diffusion of I_3^- ions in the electrolyte solution at a frequency ω_D.

All distinctive frequencies except ωD are shown on the Bode plot (Figure 3.10.(b)), where ωd is the II of the Nyquist plots at certain steady-states, appears as a break point as the high frequency limit of its semicircle, yet it is not apparent in Figure 3.10. (b).

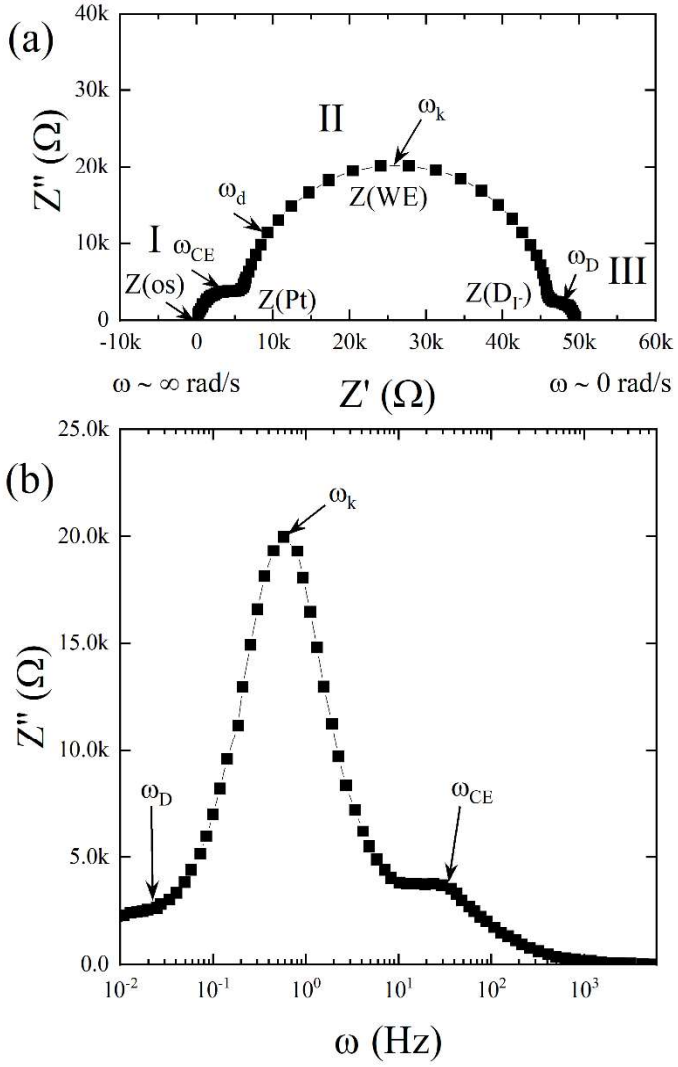


Figure 3.10 (a) Nyquist plot of DSSC (b) bode plot of DSSC

3.9 Mott-SchottkyAnalysis

Mott-Schottky offers an experimental method for determining not only the type and concentrations of primary carriers, but also the location of the flat band based on the formation of the Schottky barrier at the semiconductor/blocking electrolyte interface [118, 119]. The measurement necessitates the use of a blocking interface. Therefore,

it necessitates the absence of any potential interface redox reactions under the applied bias voltage, which might impact the capacitance of the electrode's intrinsic material. Band bending occurs under these circumstances due to the stability of the Fermi level in the semiconductor and the chemical potential of the electrolyte (Figure 3.11). It involves the depletion of the principal charge carriers (electrons) under the electrode surface, generating a Schottky barrier at the semiconductor/electrolyte interface. Due to the repulsion of positively charged ions and the attraction of negatively charged ions in the electrolyte to the electron-depleted surface, the Helmholtz layer forms on the electrolyte side. This is accurate for n-type semiconductors and incorrect for p-type semiconductors.

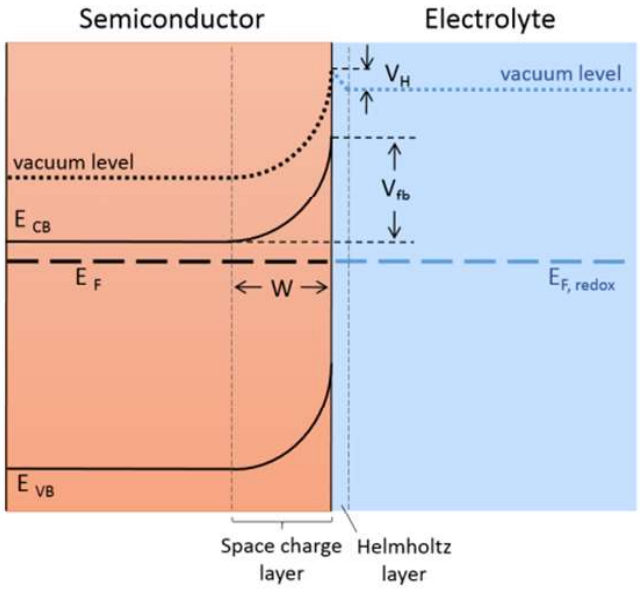


Figure 3.11 Schematic illustration of band bending at the n-type semiconductor/electrolyte interface.

The Mott-Schottky equation is

$$\left(\frac{A}{C_{bulk}}\right)^2 = \frac{2}{\varepsilon_r \varepsilon_0 e N_D}\left(E - E_{fb} - \frac{k_B T}{e}\right) \tag{3.21}$$

where C_{bulk} is the capacitance of the space charge region, A is the active surface area, ε_r is the dielectric constant, ε_0 is the permittivity of vacuum, e is the elementary

charge, N_D is the charge carrier concentration, E is the applied voltage, E_{fb} is the flat-band potential, k_B is the Boltzmann constant, and T is the absolute temperature [120]. The validity of the Mott-Schottky equation is contingent upon three hypotheses. First, two capacitances must be considered: the space charge area in Fe_2O_3 and a Helmholtz bilayer in the electrolyte. Since the Helmholtz bilayer is connected in series with C_{bulk}, its capacitance must be much higher than that of C_{bulk} for its effect to be small. Second, all charge carriers must be ionized and uniformly dispersed in space. Lastly, the space charge region's diameter must be much less than the width of the semiconductor [121]. $(A/C_{bulk})^2$ is displayed as a function of applied potential on a Mott-Schottky graph. If the three aforementioned assumptions hold true, the Mott-Schottky plot will be linear, and the concentration of charge carriers may be estimated as follows:

$$N_D = \frac{2}{\varepsilon_r \varepsilon_0 e N_D} \tag{3.22}$$

where S is the slope of the Mott-Schottky plot [121]. The flat-band potential can also be determined by extrapolating the Mott-Schottky plot to its x-axis intersection. At the intersection, the relationship

$$E_{fb} = E - \frac{k_B T}{e} \tag{3.23}$$

is used to get the flat-band potential.

CHAPTER 4

MATERIALS AND METHODS

This chapter covers the exact experimental protocols for the deposition of the films and the fabrication phases of the devices that were used in this work. It also presents the chemicals that were used in the work. In addition, this section details the application steps of various experimental procedures, including chemical bath deposition and spin coating, among others.

The materials used and their optimization significantly affect the performance of optoelectronic devices such as dye-sensitive solar cells. FTO cleaning, blocking layer thickness, paste and ionic liquid recipe, dye loading time, and the preparation of the counter electrode all affect the performance of the device. The individual performance of these layers is not sufficient for device performance, and good performance while in a combination depends on their compatibility. The best way to test this harmony is to compare both individual and device performances. In this section, the methods and contents used in cell production are clearly indicated.

4.1 Chemical Materials Used in Experimental Studies

Fluorine doped tin oxide (fluorine-doped tin oxide, FTO) used as substrates were obtained from Teknoma and its surface resistances is ~10 ohm/sq. The Hellmanex solution used in the cleaning of FTO substrates was supplied from the Hellma GmbH company, while the necessary acetone and ethanol was used in technical quality.
The spin-coating solution for the compact TiO_2 (c-TiO_2) layer contained titanium (III) chloride solution (Sigma Aldrich) and isopropyl alcohol (Sigma Aldrich). An average of 21 nm of grain-sized Degussa P25 TiO_2 (Evonik-Degussa GmbH), ethyl cellulose (Sigma Aldrich), and terpineol (99%, Sigma Aldrich) were utilized in the paste prepared for the mesoporous TiO_2 (m-TiO_2) layer. The precursor used for nickel dopant is nickel (II) nitrate hexahydrate (97%>, Sigma Aldrich). 1-Propyl-3-methylimidazolium iodide (BMIMI, 99%, SigmaAldrich), Lithium iodide (≥ 98.0 %, Merck), 4-tert-Butylpyridine (96%, SigmaAldrich), Guanidine thiocyanate (≥97%,

SigmaAldrich), Iodine (≥99.8, SigmaAldrich) and Copper(I) thiocyanate (99%, Sigma Aldrich) was used for electrolyte solution as precursors. In electrolyte solution, valeronitrile (99.5 percent, SigmaAldrich), acetonitrile (99.9 percent, SigmaAldrich), and 3-methoxypropionitrile (98.0 percent, Sigma Aldrich) were utilized as solvents. For the counter electrode solution, chloroplatinic acid hydrate and isopropyl alcohol were used. The chemicals employed in the thesis study were also used without even being purified.

4.2 Cell Production

4.2.1Cleaning of FTO substrates

FTO substrates with a size of 1.5 cm x 2.5 cm, a thickness of 3.2 mm, and a resistance of less than 10 ohm/sq were employed as substructure in the cell fabrication. Follow the methods below to effectively clean substrates:

- Sonication for 5 minutes in hot Hellmanex III
- Rinse twice with hot deionized water.
- Sonication in IPA for 5 minutes
- Rinse twice with hot deionized water.
- Using an air gun to dry.

Following the cleaning process, the substrates were treated at 500 °C for 30 minutes to totally remove the organic residues from the surface. It was exposed to a 15-minute UV-O_3 process to activate the surface before the coating.

4.2.2 Production of the compact TiO_2 layer

The compact TiO_2 (c-TiO_2) layer is applied to the surface of the FTOs using a spin-coating process, the thickness of the coating layer is around 90 nm. Titanium (III) chloride solution (15%) and isopropyl alcohol were used in the spin-coating solution for the compact TiO2 (c-TiO_2). The molarity of the prepared solution, spin-coating rotational speed, coating cycle, annealing time, and annealing temperature have all been examined. Table 4.1 shows the parameters for the optimization process for the c-TiO_2 layer.

Table 4.1 Optimization parameters of c-TiO_2 layer.

Sample	Rot. Speed (RPM)	Ann. Temp. (°C)	Ann. Time (min)	Drop Cyc. (pcs)	Molarity (mg mL^{-1})	Test
AB0	Bare FTO					
AB1	1600	450	30	16	100	RPM test
AB2	3200	450	30	16	100	
AB3	6400	450	30	16	100	
AB4	3200	350	30	16	100	Temp.
AB5	3200	550	30	16	100	
AB6	3200	450	15	16	100	Time
AB7	3200	450	60	16	100	
AB8	3200	450	30	8	100	Drop cyc.
AB9	3200	450	30	32	100	
AB10	3200	450	30	16	50	Molarity
AB11	3200	450	30	16	200	

4.2.3 Production of the mesoporous TiO_2 layer

Before beginning this experiment, a 10% wt. ethyl cellulose solution was made as a stock solution for subsequent usage. The 10% wt. ethyl cellulose mixture contains two types of ethyl cellulose. The first one accounts for 4.4 percent of the total weight of the mixture and has a viscosity of 7-15 mPa.s. It is composed of 5.6% wt. ethyl cellulose with a viscosity of 30-70 mPa.s. The preparation of stock solutions is due to the dissolving of ethyl cellulose in ethyl alcohol after around 12 hours.

The paste employed for the mesoporous TiO_2 (m-TiO_2) layer is made up of 13% wt. Degussa P25 TiO_2, 40% wt. EC stock solution, and 47% wt. Terpineol. The prepared mixture was homogenized for 10 minutes at 3500 rpm with a Speed Mixer. The produced paste was velvety and smooth. Following this, the cake was rolled for one

day using the Roller Mixer at roughly 50 RPM. The pastes were spin-coated (2000 rpm, 30 s and 3000 rpm, 30 s) on the blocking layers. Following deposition, the PAs were held at 500 °C for one hour.

4.2.4 Production of the electrolytes

A drop of the electrolyte consisting of I_2 (0.05 M), LiI (0.1 M), 1-butyl-3-methylimidazolium iodide (BMII, 0.6 M), 4-tert-butylpyridine (TBP, 0.5 M) and acetonitrile was put between the PA and CE components.

Table 4.2 Receipts of electrolytes.

	EL#4	**EL#5**	**EL#6**	**EL#7**
	Chemicals (M)			
BMII	0.6	0.6	0.6	0.6
TBP	0.5	0.5	0.5	0.1
GuSCN	0.1	0.05		
I_2	0.03	0.05	0.03	0.01
LiI		0.1		0.1
CuSCN			0.1	
	Solvents (mL)			
Acetonitrile	8.5	8.5	8.5	
Valeronitrile	1.5	1.5	1.5	
MNP				10

4.2.5 Dye loading the working electrodes.

0.3 mm N719 paint was dissolved in methanol and agitated at 500 RPM for 2 hours at room temperature. The electrodes were immersed in a N719 solution for at least 18 hours after cooling to room temperature. The dyed working electrodes were rinsed with ethanol and left to air dry.

4.2.6 Counter electrode preparation

5mm $H_2PtCl_6.xH_2O$ was dissolved in 2-propanol and stirred at room temperature for 30 minutes at 500 rpm. For 15 minutes, a UV-O_3 treatment was applied. Dripping 20 µL solutions on the FTO surface and spin coating (2000 rpm, 5rpm/s, 30s) were used. For activation, the counter-electrodes were annealed at 475 °C for 30 minutes.

4.2.7 Cell assembly

All components were sandwiched together to form the structure. Between the working and counter electrodes, electrolyte was poured. Utilizing a solar simulator, I-V measurements were taken from contacts using crocodile cables under 1 sun (100 mW/cm^2) intensity test circumstances. Each electrode's FTO glass edge was coated with high purity silver paint to boost conductivity and increase electrical contact.

CHAPTER 5

RESULT AND DISCUSSION

Based on the publication “Atilgan, A., and Yildiz, A. (2022). Ni-doped TiO_2/TiO_2 homojunction photoanodes for efficient dye-sensitized solar cells. International Journal of Energy Research, 46(10), 14558-14569, this section is reproduced (or “reproduced in part") with permission from International Journal of Energy Research. Copyright © 1999-2022 John Wiley & Sons, Inc. All rights reserved.

5.1 $TiCl_3$ Based Blocking Layer

The general requirements of an ideal blocking layer in DSSC can be defined as follows. Between the TCO and the photoanode, the compact and dense layer will accumulate as a blocking layer. As the compact blocking layer builds up, it will completely cover the TCO's surface, reducing electron leakage. In addition, the compact layer also helps to improve the connection between porous nanoparticles and TCO. Since the porous particles are closely connected to one another, the electron can move more quickly. In DSSC, the electron life is prolonged by the effective electron path, which also decreases resistance and recombination rate. It should be thin enough to allow the electron to flow. To effectively transfer the electron to the absorption element like titania or dye, the incoming light of an ideal blocking layer must have a higher light transmittance and a low surface roughness. Figure 5.1 provides the requirements of an ideal blocking layer in DSSCs.



Figure 5.1 The requirements of an ideal blocking layer.

It is also available in a few functions attributed to the blocking layer. To improve DSSC performance, it is recommended to insert a dense block layer between the interface and the FTO/electrolyte interface [122, 123]. This layer will block both FTO/electrolyte interactions and reverse electron flow. Further, the incorporation of a dense BL creates a potential barrier between the FTO and the semiconductor material, preventing the FTO's electrons from recombining with those of the semiconductor [124, 125]. The introduction of BL also diminished the interfacial resistance of porous TiO_2. In addition, the BL provides improved contact between FTO and TiO_2, which enables efficient electron transfer and collection and ultimately improves the efficiency of the device [126].

Without a doubt, characteristics such as the precursor concentration, the thickness, and the morphological structure of the blocking layer must be considered, as they may have an impact on the result of the DSSCs' efficiency. A high concentration of the precursor will reduce the thin film's transmittance and raise the energy barrier,

resulting in a negative impact on the device's performance. The thick blocking layer, on the other hand, will result in an increase in device resistance as well as a suppression of charge recombination. Controlling some of the important factors is therefore critical for the development of an effective DSSCs [126].

The blocking layer's primary role is to act as a potential barrier to recombination, while it can also increase the amount of adsorbed dye molecules in some instances. Insulators are the only materials that can be used for the blocking layer. All the data on blocking layers in the literature is on insulating oxides like Al_2O_3, NiO, SiO_2, ZnO, ZrO_2, Nb_2O_5, and rare earth oxides. On the other hand, it is well known that a semiconductor's electronic properties can be controlled as a function of size, a phenomenon known as “quantum size effect”, which can sometimes extend to the insulator domain. Because the blocking layer must be thin, it appears that some semiconductors, even if they are ohmic conductors and/or have strong colors in their bulk states, could be employed as the blocking layer material [127].

$TiCl_4$ pre-treatment is utilized to create the blocking layer on the FTO substrate to reduce recombination processes in TiO_2-based DSSCs. The necessity for a novel approach was highlighted by the time-consuming and hazardous nature of $TiCl_4$ pre-treatment.

A considerable amount of literature has been published on blocking layers. These studies have helped determine the parameters of an ideal blocking layer. In the first stage, the variables that could impact the requirements were identified. Using the $TiCl_3$ precursor with spin-coating technique, the following factors have been found to provide an optimum blocking layer:

- molarity of the solution,
- rotational speed of the spin coater,
- number of coatings,
- annealing temperature,
- annealing time.

Three different forms of pinholes exist: closed channels, keyholes, and open channels [128]. Keyholes and closed channels do not result in a short circuit between layers,

although they increase surface resistance and decrease recombination resistance. On the other hand, keyholes and closed channels have a detrimental effect on the ideality factor of the device, which in turn causes a drop in the device's overall performance [96, 129]. However, craters, cracks, and open channels result in a short circuit between layers, which significantly lowers the device's performance [130].

5.1.1Surface examination of the blocking layer by SEM

The coated surfaces were first investigated by FE-SEM. The top view FESEM image of the samples given in Figures 5.2-6 revealed the types and densities of pinholes/cracks. The blocking layer is morphologically similar, as seen in the pictures. Like a thin blanket, it has fully covered the surface. The test criteria were effective on crack, hole, or crater density and types even though the coated layer does not differ morphologically.

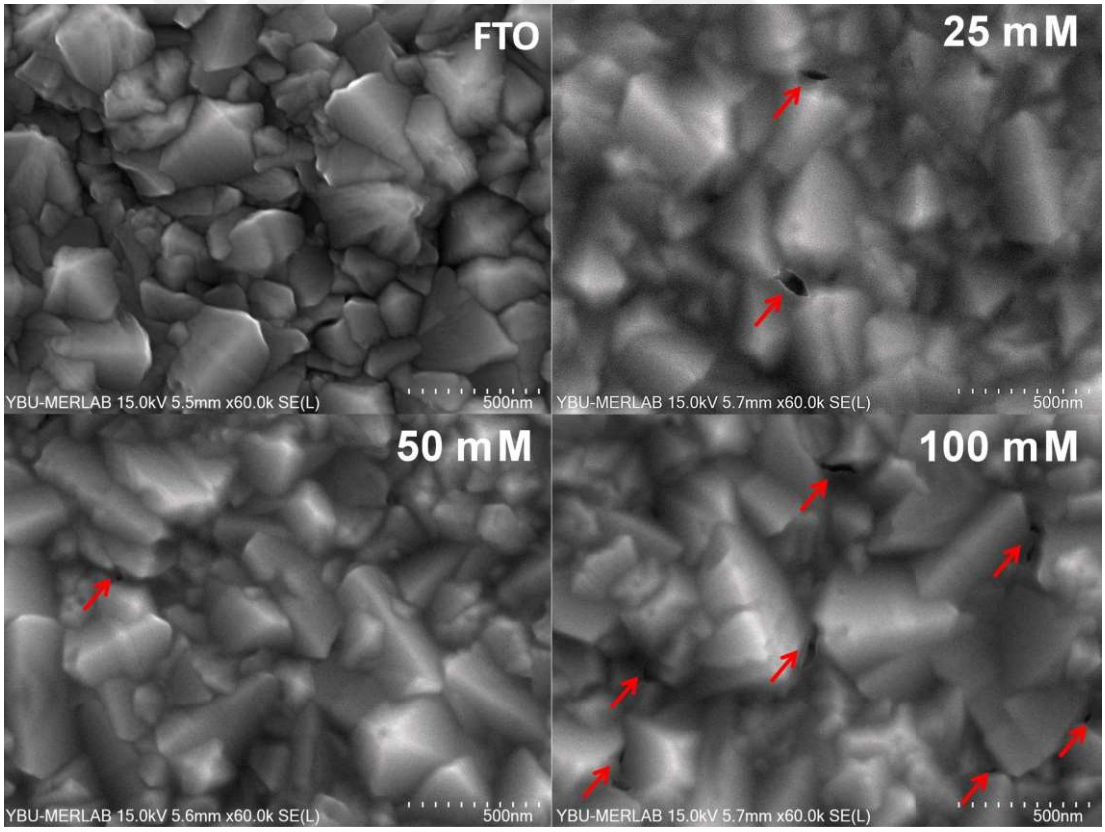


Figure 5.2 SEM topographies of (a) bare FTO, (b) 25 mM , (c) 50 mM, and (d) 100 mM solution of $TiCl_3$ aqueous was spin-coated onto clean FTO substrates.

In accordance with Figure 5.2, 25 mM, 50 mM, and 100 mM aqueous $TiCl_3$ solutions were spin-coated onto clean FTO substrates. FTO substrates coated with a 25 mM $TiCl_3$ solution are greater and wider than crack regions, although the number of cracks is lower and narrower than substrates spun with a 100 mM solution. The surface morphology has not been drastically affected by alterations to the molarity. However, the change in the fracture and crater structure has exposed the significance of the coating's solution concentration. It has been said that the most important thing for making a blocking layer without holes and cracks is concentration.

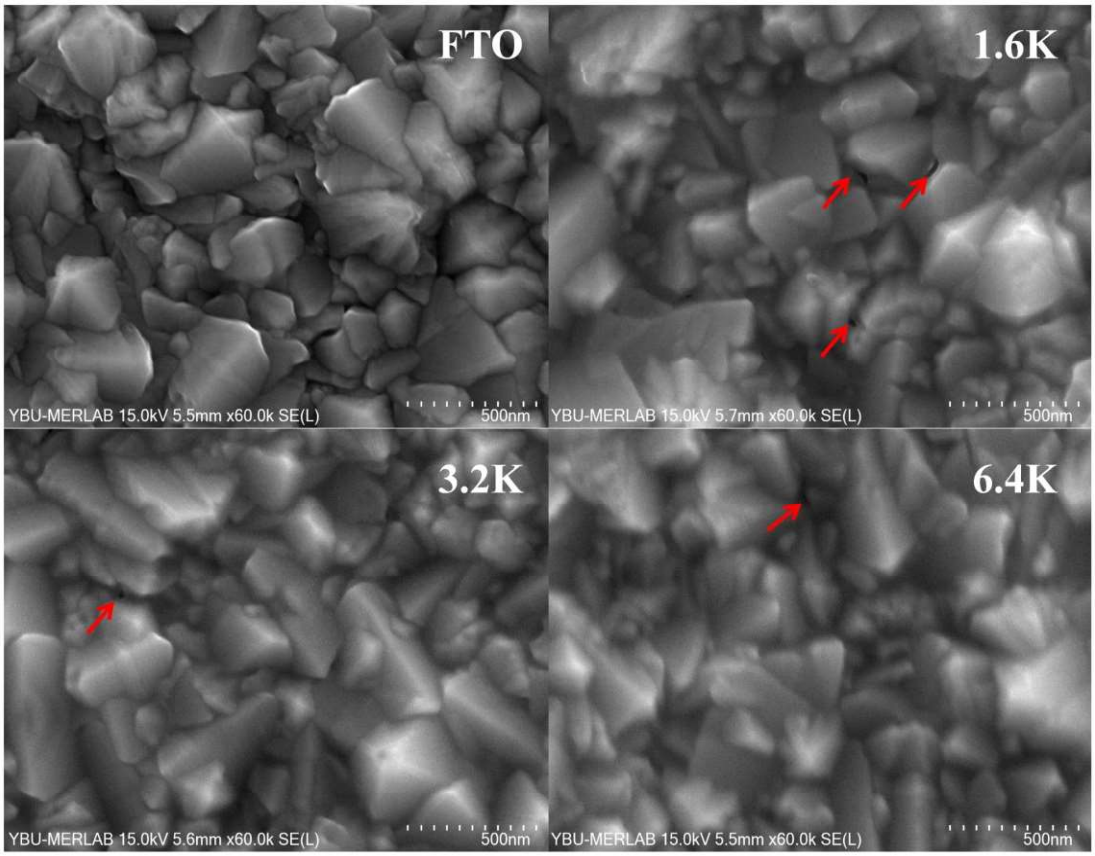


Figure 5.3 Comparison of the FE-SEM images of bare and coated FTOs under various spinning speed.

As shown in Figure 5.3, the higher the spinning speed, the rougher the surface becomes, and the crack size shrinks. All of the layers are quite thin; however, as the spinning speed increases, so does the coating thickness. The cracked form changes with increasing spinning speed; in the form of a tear at 1.6K RPM, relatively larger

cracks, and a larger number of them appear. The number of cracks reduces, and they transform into pinholes for 3.2K and 6.4K RPM.

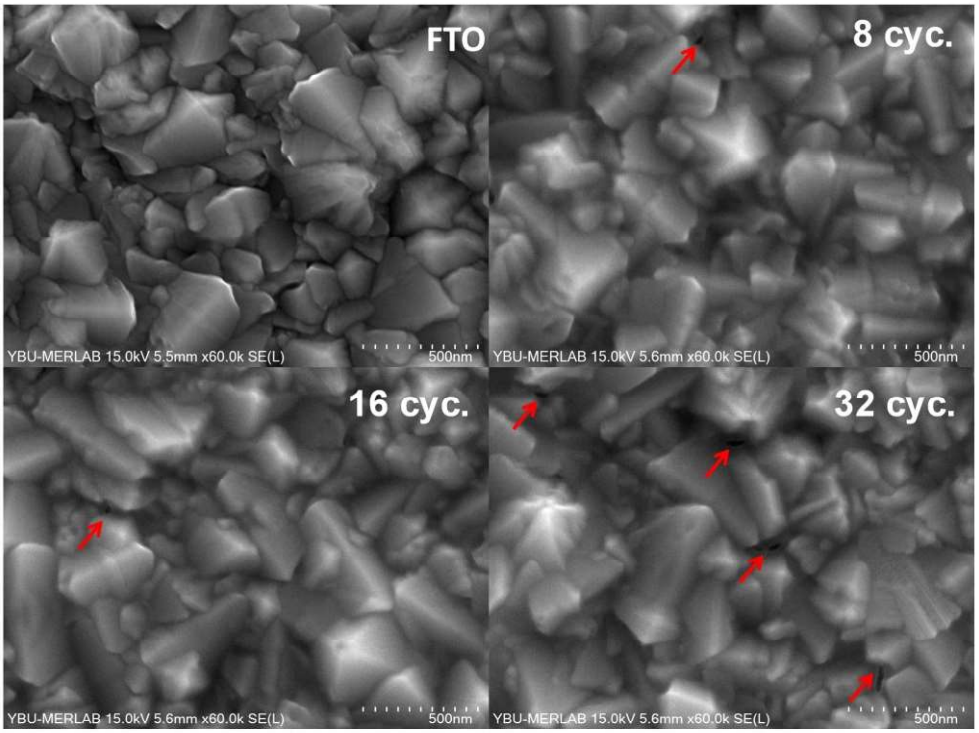


Figure 5.4 Top-view SEM image of bare and coated FTOs under various drop cycles.

The surface morphology of bare and TiO2-coated surfaces under various drop cycles was investigated by FE-SEM images. As clearly observed from the surface images in Figure 5.4, TiO2 layers were uniformly deposited on the FTO substrates. In addition, 8 and 16 cycle-covered surface defects are in the form of pinholes, and the number of defects is less than 32 cycle-coated surfaces. For sol-gel applications involving spin-coating, the coating thickness is controlled by the number of coating cycles [131, 132].

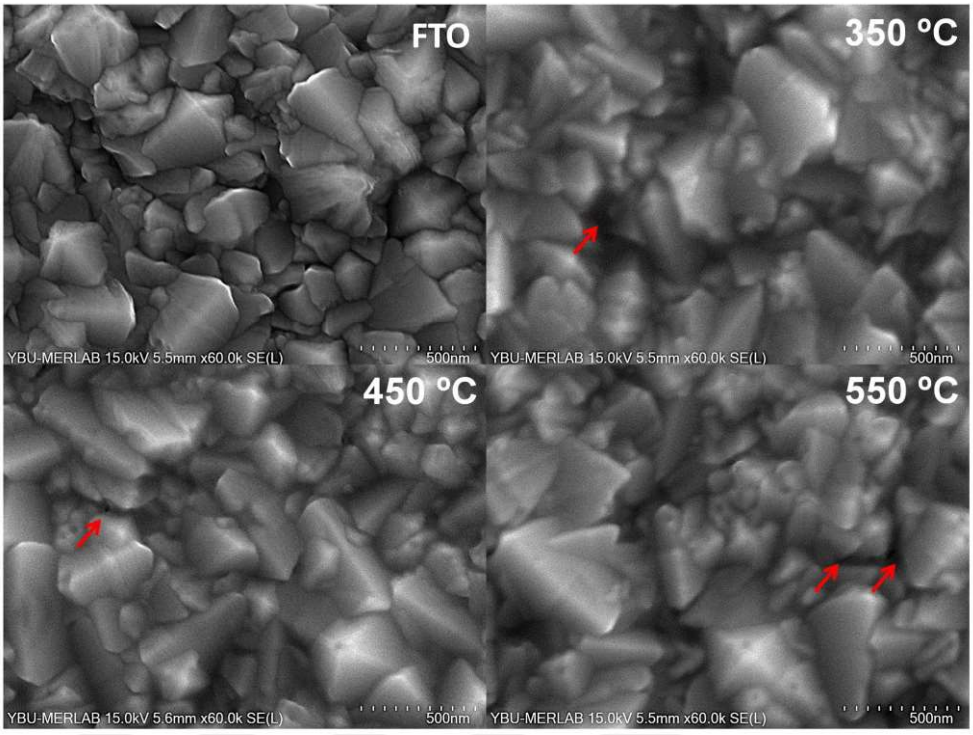


Figure 5.5 Comparison of the FE-SEM images of bare and coated FTOs under various annealing temperatures.

The images obtained from FE-SEM analysis can be compared in Figure 5.5. The concentration of the solution used during coating is 100 mM. The FTOs are covered at 3.2K rpm, and the spinning cycles are 16. Annealing temperatures are 350, 450, and 550 °C respectively, and the annealing time is 30 minutes. Changes in temperature have little effect on the form of cracks, although at 550 °C, the largest crack was found, relatively.

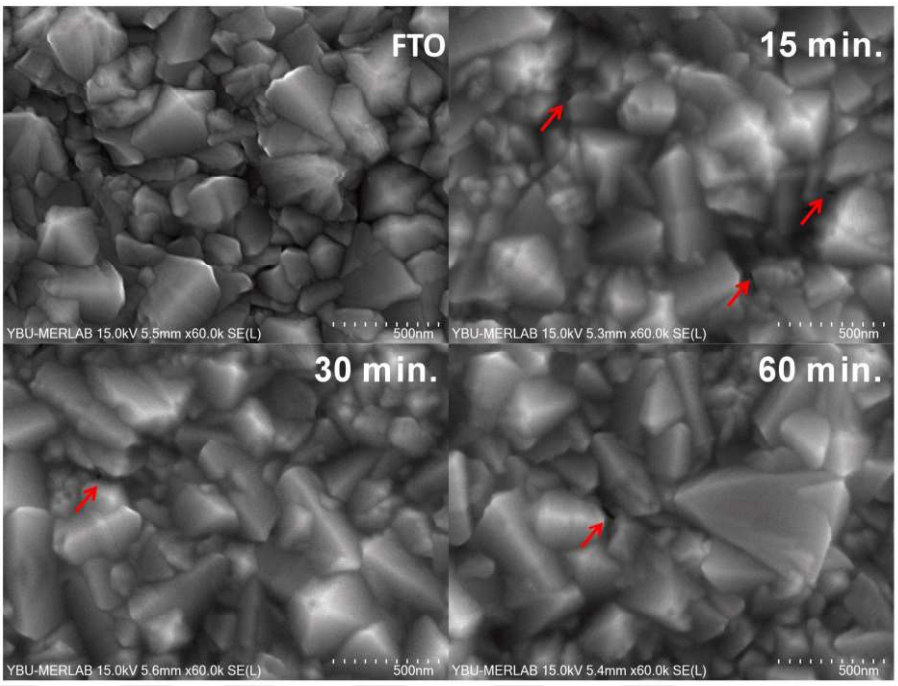


Figure 5.6 FE-SEM surface morphologies of uncoated and coated FTOs sintered at 450 degrees Celsius for 15, 30, and 60 minutes.

Figure 5.6 indicates that annealing time has not dramatically modified the surface morphologies. However, the research indicates that extending the annealing time improves particle size and crystallinity. Crystallinity refers to a solid's degree of structural order. In a crystal, the arrangement of the atoms or molecules is uniform and periodic. The degree of crystallinity has a significant impact on the material's hardness, density, transparency, and diffusion. These parameters are essential for an effective blocking layer.

5.1.2 UV-Vis and AFM results $TiCl_3$ based compact layer

The blocking layer, among the various materials and interfaces, refers to the layer between the transparent conductive substrate and the light-absorbing layer. The fact that the blocking layer covered by FTO has a low absorbance permits it to better transmit incoming light to the dye, which confers a significant advantage. In other words, the transition rate of the blocking layer should be high. In this part, bare FTOs and FTOs coated with a blocking layer are contrasted, and the UV, visible, and infrared (IR) regions are described in relation to the following parameter changes. Visible zone, UV zone at 400 nm, and IR region above 800 nm comprise the 400-800

nm wavelength range. Typically, the range of dyes used in DSSCS falls within the visible spectrum. Numerous experiments have created cells that can function in the dark and are tailored to absorb IR-region photons. In fact, however, the IR rays cause thermalization in the cell and prevent it from functioning properly, and the UV rays harm the dye, which is made of organic material, resulting in significant performance losses. In this regard, it is crucial to identify the region created by the tested parameters. A total of 49.4 percent of the light that reaches Earth's surface comes in the form of infrared radiation, while the remaining 42.3 percent is visible light. A little over 8 percent of the sun's rays are ultraviolet. Though the radio spectrum covers a larger area, it is the visible section of the sun that has the maximum intensity.

Titanium dioxide (TiO_2) is commonly used as a white pigment in coatings. It has a great degree of whiteness and opaqueness. The fundamental principle has two-ways. First, the micro TiO_2 particles effectively spread visible light due to the material's high index of breaking. Second, titanium dioxide absorbs very little visible light. Therefore, the human eye perceives particles as white. TiO_2 absorbs UV rays effectively, particularly when pigment particles are small. Small particles have a high -specific surface area and, as a result, contain many surface molecules that absorb radiation most effectively. Nano-sized titanium dioxide, with a particle diameter far below 100 nm, is utilized as a UV absorber in coatings and sunscreen. A nano-TiO_2 coating is transparent because visible light is neither scattered nor reflected.

Like other metal oxides, the optical properties of TiO_2 nanoparticles are dependent on particle size. Numerous studies in the scientific literature have concentrated on this topic and demonstrated the efficiency of a mesoporous absorber layer with a particle size of 21 nm and a scatter layer particle size of 400 nm. Although there is no particle size value for the blocking layer, studies on the thickness of the various blocking layers have been conducted.

Figure 5.7 illustrates the variations in light transmittance and the average transmittance that occur in the ultraviolet, infrared, and visible regions because of changes in the concentration of the solution. The observed blue-shift is correlated with solution concentration and particle size, with the blue-shift occurring as particle

size decreases. The average UV region transmittance has improved in all solutions, but the significant rise was recorded as 16% in a solution containing of 25 mM. At each concentration, the IR region has been negatively affected. The typical visible area development is 25 mm, but 50 mM and 100 mM are promising.

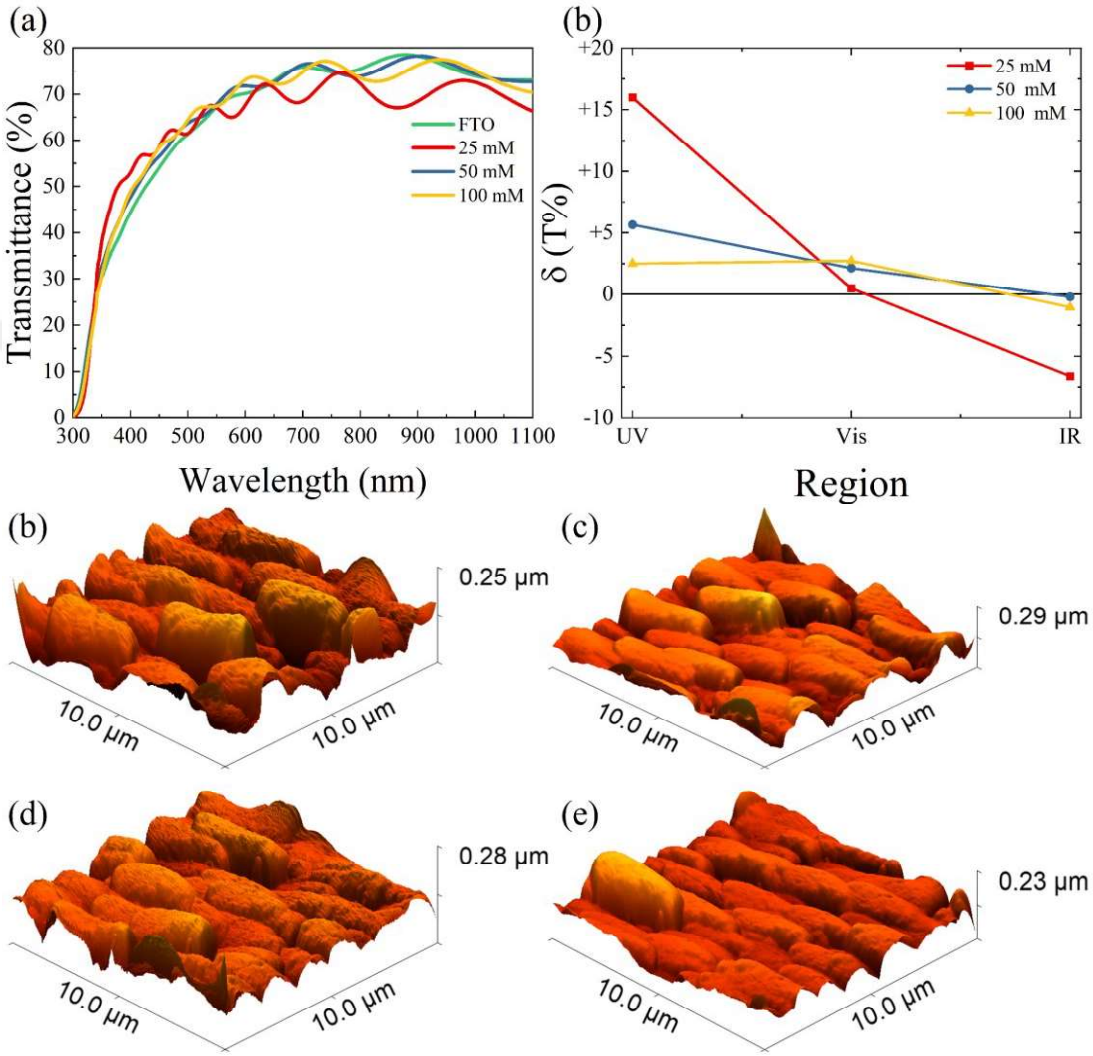


Figure 5.7 a) Transmittance spectra b) relative changes against FTO according to concentration of precursor, surface topologies of c) bare FTO, and coated FTOs with solution of d) 25 mM, e) 50 mM and f) 100 mM $TiCl_3$ in isopropanol.

The RMS values are also affected by the decreasing particle size, resulting in a decrease as the particle size continues to decrease. The roughness of the film surface may be affected by the sizes of the coated particles. It will decrease surface

roughness by filling small-sized particle surface cavities and gaps at a higher rate. The particles above a critical particle size cause a limited decrease or increase in roughness. The RMS value of uncoated FTO is calculated at 45.2 nm. The RSM values from the lowest solution molarity to highest were observed as 44.9 nm, 33.01 nm, and 39.8 nm, respectively. The smallest value of surface roughness was found at a solution concentration of 50 mM. These results hint that the ideal concentration of solution will be between 25 mM and 50 mM, and near 50 mM.

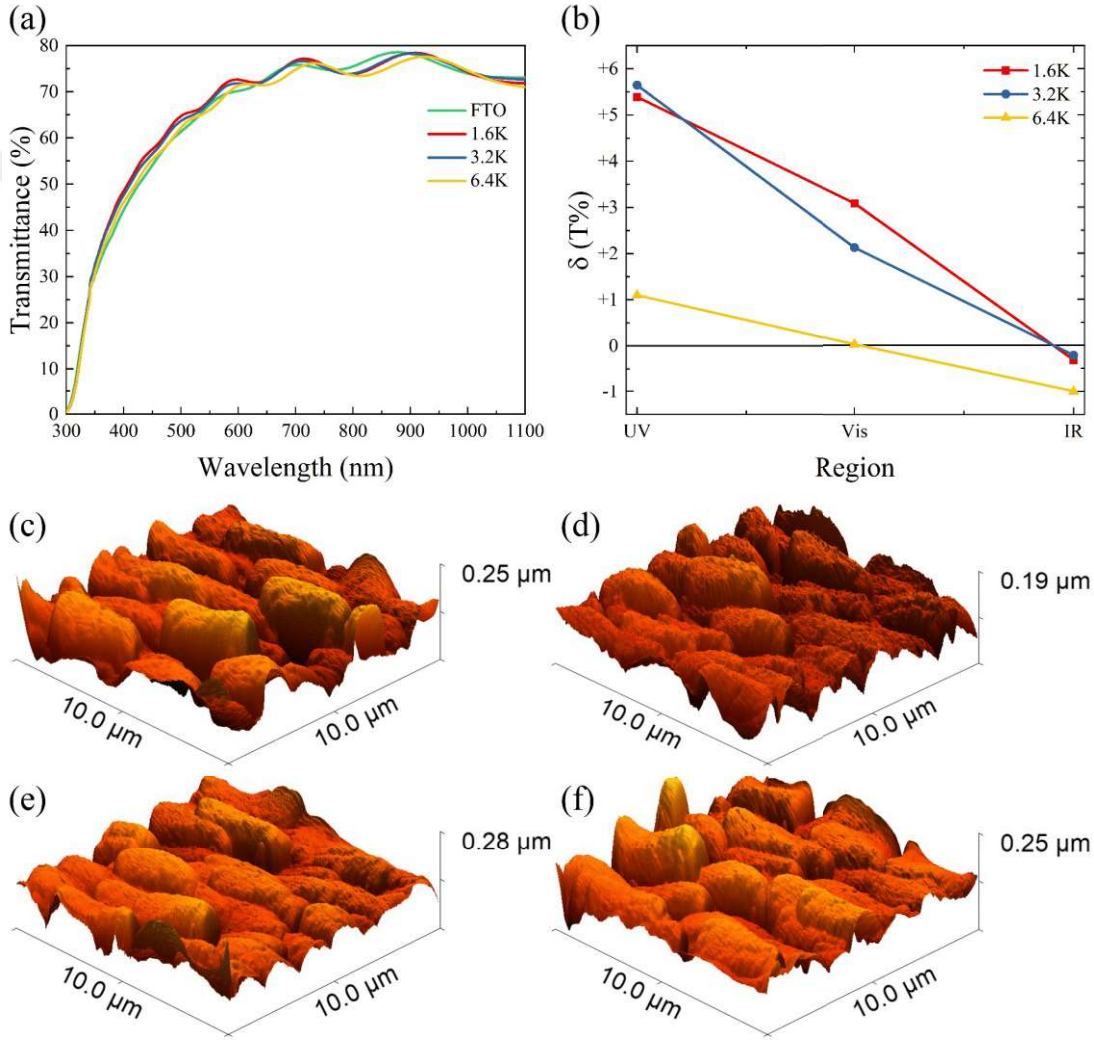


Figure 5.8 a) Transmittance spectra b) relative changes against FTO according to roational speed, and surface topologies of c) bare FTO, and spin-coated FTOs at d) 1.6K , e) 3.2K and f) 6.4K rpm.

Figure 5.8 depicts the graphical representation of the influence of the rotation rate of spin coated FTOs on light transmittance and surface roughness. In fact, the ultimate thickness of the film is inversely proportional to the linear with the square root of angular velocity. In other words, the more the angular speed increases, the more the final film thickness decreases. For example, if the angular speed is increased four times, the end film thickness will be halved. We already mentioned that the final thickness of a film depends on the material concentration, solvent evaporation rate, and other variables. In our study, it will not be a problem to use this pattern due to other operations using the same solution. In addition, the thickness of the sample, which is covered with an angular speed of 3.2k, is about 10 nm. However, the development in the UV region increased by 1% for 6.4K, a different trend than the others. The biggest increase in transmittance values in the visible region was observed in a sample with a 1.6K angular speed, and the value is approximately 3%. Considering the transmittance spectrum, the sample with an angular velocity of 3.2K has an average maximum transmittance increase of 2.1%. RMS values are 41.70, 33.04, and 47.57 nm, respectively, for low angular velocity. A smoother surface was noticed at higher RPM values accepted in the literature, whereas the best value was recorded at 3.2k RPM. Parallel to average transmittance, the lowest RMS value was observed in the sample with an angular speed of 3.2k RPM.

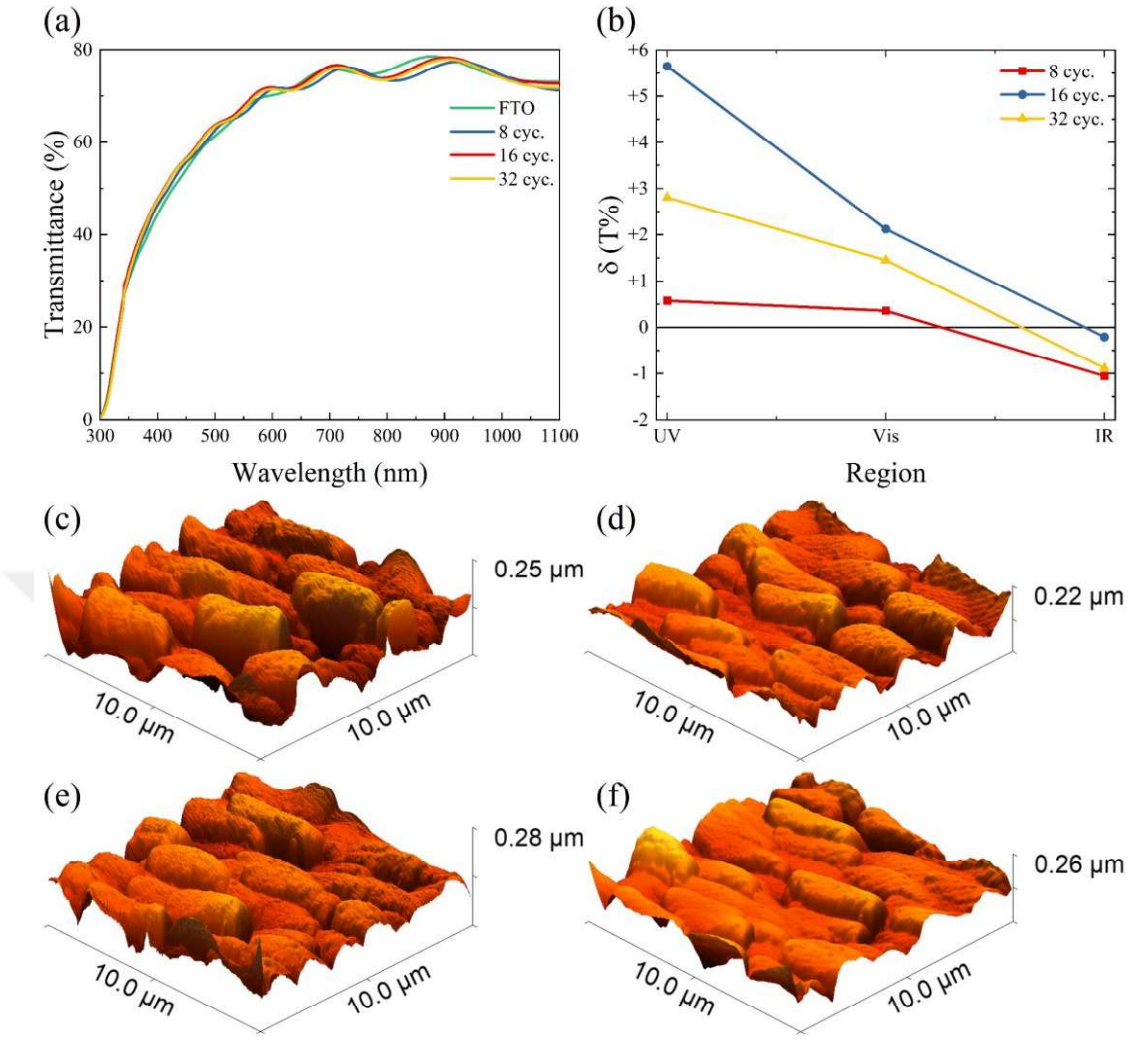


Figure 5.9 a) Transmittance spectra and b) relative change against FTO according to various coating cycles, and surface topologies of c) uncoated, coated for d) 8, e) 16 and f) 32 cycles.

Coating cycle is one of the primary parameters that determines coating thickness. Recent research indicates that increasing the number of coating cycles enhances the crystallite size and photoluminescence emission density of spin-coated oxide thin films [133]. In a separate investigation on InN and AlN, it was found that the number of coating cycles influences numerous characteristics, including crystal structure, surface morphology, element composition, and optical band range. In these findings, they demonstrated that the relationship between closure thickness and coating rotation numbers is linear. [134]. In brief, 8 times covered sample has a similar trend in transmittance as 6.4K. The specimen covered sixteen times has the highest

transmittance value in the visible spectrum. The number of low coatings yields RMS values of 44.99, 33.04, and 39.80 nm. Lee and his buddies have determined that the optimal number of coatings for the film, which they analyze in a variety of ways, is 20, which is quite close to the optimal value we discover. According to the findings of this research, the sample including 16 cycles had the largest increase in visible-spectrum development. In addition, the root-mean-square (RMS) values for their samples were determined to be 42.6, 33.0, and 39.1 nm, respectively, after coating them for 8, 16, and 32 cycles.

Literature claims that increasing annealing time lowers optical transmittance, increases dislocation density and micro-tensions, and decreases crystal size [135]. In addition to these results, the authors found a reduction in film porosity and thickness [136-138]. They noted that the removal of organic and solvent residues from the surface of the film during annealing may be the cause of this reduction in thickness [139]. There is evidence that particle size rises as annealing time increases, perhaps owing to nanoparticle aggregation. It has also been suggested that applications of temperatures over 500 °C may enhance the conversion from anatase to rutile [140]. Although there is published research indicating that increasing the annealing time increases the surface roughness, the temperature and annealing periods used here have a substantial effect on the outcome. In contrast, Khan et al. demonstrated that the crystal quality of films coated with a lengthy annealing time improves, perhaps owing to the reduction of flaws between surrounding crystals; as a result, the gaps will fill, and the film thickness will decrease [141, 142]. In addition, they reported that subjecting the film to heat for up to 90 minutes would improve its heat absorption capacity, which in turn would increase its light absorption capacity.

Our blocking layers were annealed in this section of the research at intervals of 15, 30, and 60 minutes, which are routinely utilized in the literature. All annealing periods were found to follow a similar pattern in the transmittance graphs. While there was a rise in transmittance value, particularly in the UV zone, there was a reduction in the IR region. In the visible area, the sample that was annealed for 30 minutes showed the greatest improvement. Due to the absorption qualities of TiO_2, which are made possible by the enhanced crystal quality, it is believed that the

average transmittance value, particularly in the UV region, rises and subsequently falls with an increase in annealing time. Additionally, the RMS values showed a declining tendency as time went on, which was completely consistent with the literature. From low to high, these values were determined to be 45.76, 33.04, and 29.88 nm, respectively.

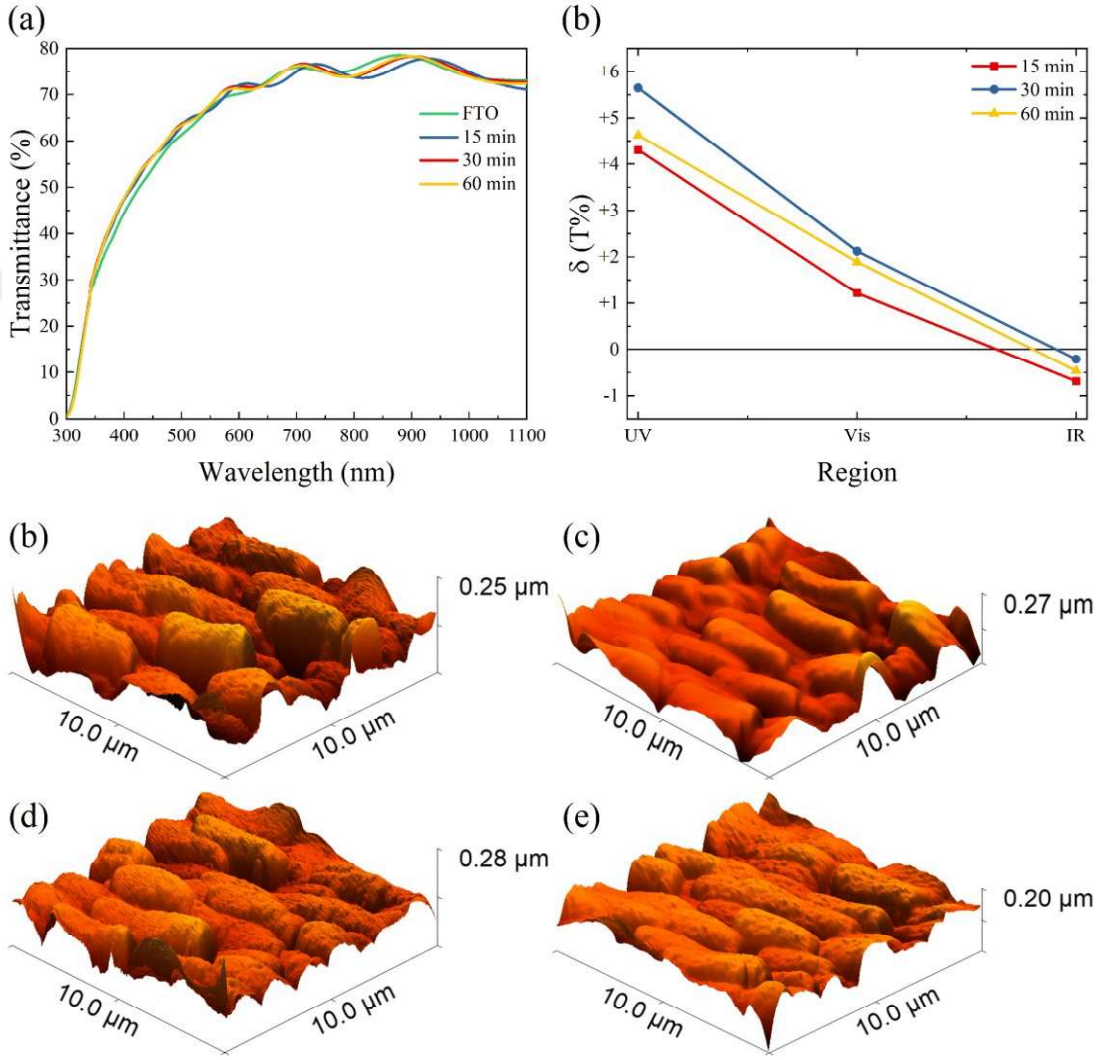


Figure 5.10 a) Transmittance spectra and b) relative change against FTO according to various annealing time, and surface topologies of c) uncoated, anealed for d) 15, e) 30 and f) 60 minutes.

In the literature, the impact of temperature has received comparatively greater attention. Phase change is the first concept that comes to mind when considering the impact of temperature [143, 144]. Three changes were noted: a reduction in pore

structure, an increase in particle size because of agglomeration, and a reduction in film thickness. Additionally, as the lattice spacing shrank, an oxygen vacancy-related decrease in the XPS peak was seen during the annealing processes at temperatures between 300 and 500 °C. However, at higher temperatures, such as 800 and 900 °C, this peak completely vanished, leading to the conclusion that the high-temperature annealing process had reduced the oxygen vacancy [144, 145].

The increase in annealing temperature resulted in a larger grain size, which decreased the film's optical band. Gradually, the UV absorbance rose [146]. However, when the annealing temperature rose, the grains tended to aggregate [147]. Due to the reduction in voids in the film and the rise in density, the refractive index rose [147, 148]. The extinction coefficient rose as the annealing temperature climbed from 300 to 500˚C. When the annealing temperature above 400°C, FT-IR spectroscopy revealed the production of the hydroxyl group. The hydroxyl-containing surface coating may readily establish hydrogen bonds with H_2O molecules, resulting in a hydrophilic conversion. This indicates that the water contact angle will decrease [149, 150]. Due to synergistic annealing effects, when the annealing temperature was raised from 300°C to 500°C, the band gap shrank, and recombination was successfully minimized. Consequently, raising the annealing temperature enhances the visible light absorption and photocatalytic activity of TiO_2 thin films [150, 151] Annealing temperature influence on the structural, optical, and photocatalytic activity of nanocrystalline TiO_2 films produced by the sol-gel technique and employed in solar cell applications [151]. In experiments, it was discovered that raising the annealing temperature from 0 to 600˚C shifted the crystal plane (101) by 2 theta degrees. In addition to the rise in particle crystallite size, the XRD peak intensities also rose. At 400˚C, Lukong et al. found the particle size to be 4.77 nm [152]. In addition, a red shift in emission band maximums and an increase in green emission are noticed as the annealing temperature rises. The index of refraction of a film depends on its thickness and annealing temperature. The optical characteristics of the film fluctuate significantly with annealing temperature, which may be a result of changes in the surface morphology, crystal structure, and film density [153]. The dislocation density and number of crystallites per unit surface area of the anatase phase drop increase as the annealing temperature rises from 300°C to 350°C. At low

temperatures, dislocation density and crystallites per unit surface area vary fast, but at high temperatures (over 450°C), the density of dislocations and crystallites decreases gradually.

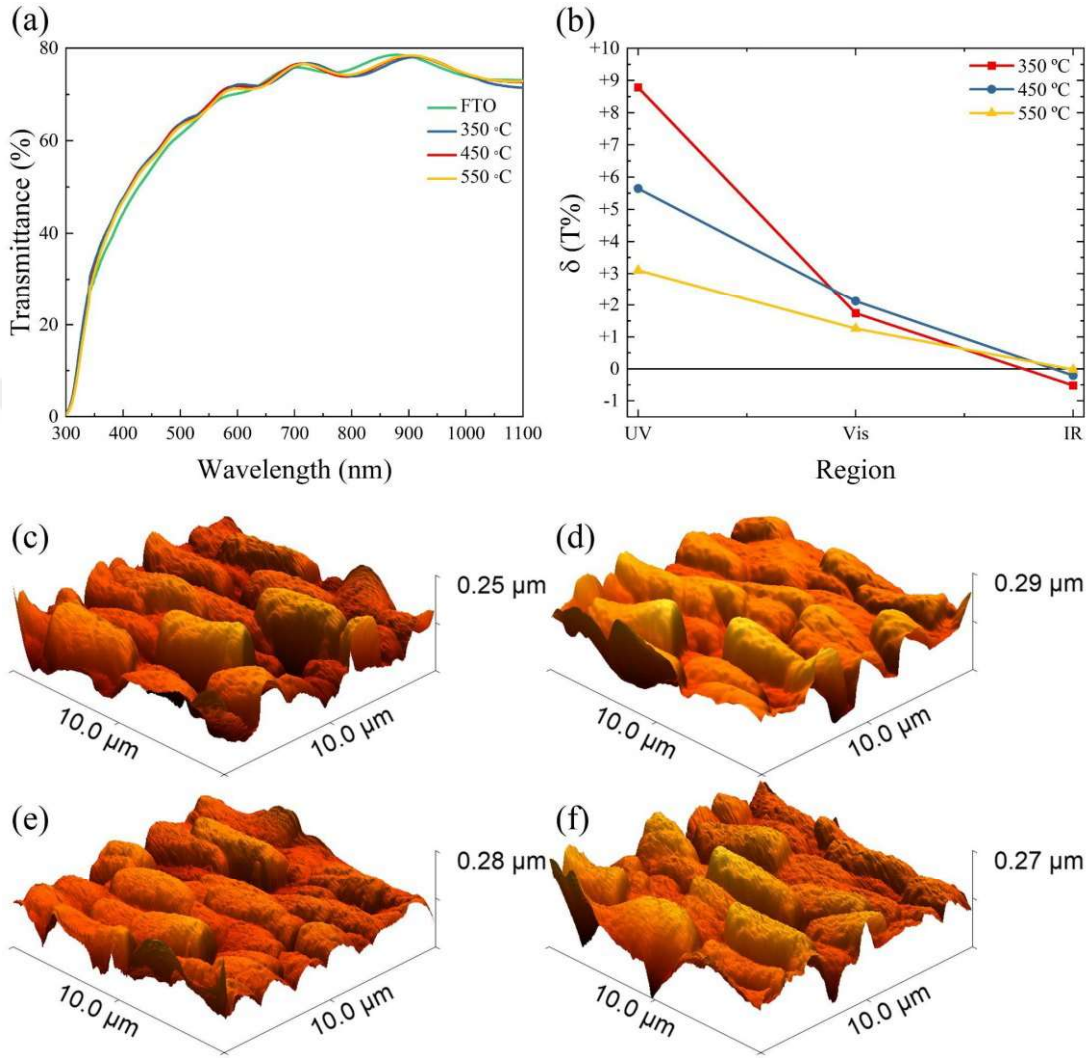


Figure 5.11 a) Transmittance spectra and b) relative change against FTO according to various annealing temperature, and surface topologies of c) bare, anealed at d) 350, e) 450 and f) 550 C°.

5.1.3Change of resistivity of FTO/TiO_2 under various test parameters

The resistance of the FTO obtained from Teknoma and cleaned using the methods previously obtained is7.55 Ω/sq. When the TiO_2 layer is placed on the cleaned FTO, it is anticipated that the resistance will rise. Long annealing times reduce conductivity. Since resistivity is inversely proportional to conductivity, an increase in

annealing time results in an increase in thin film resistivity [139, 147]. Khan et al. found that when the annealing period rises, the external energy (thermal energy) that increases the conductivity of the TiO_2 film is transferred to the conduction band of TiO_2 through excitation [141]. This growth persisted until the end of the 90-minute annealing period, when the maximum conductivity was reached. The magnitude of this enhancement is MΩ [137].

Table 5.1 Comparison of the sheet resistance of FTO/TiO_2 layers formed to that of FTO and other coated films.

Sample	R_{sh} (Ω/sq.)	δ (%)	Sample	R_{sh} (Ω/sq.)	δ (%)
FTO	7.55	-			
1.6K	8.58	+13.7	8 cyc	7.90	+4.7
3.2K	8.33	+10.4	16 cyc	8.33	+10.4
6.4K	7.72	+2.4	32 cyc	9.36	+24.0
350C	7.26	-3.8	25 mg/mL	8.06	+6.7
450C	8.33	+10.4	50 mg/mL	8.33	+10.4
550C	9.45	+25.2	100 mg/mL	8.13	+7.7
15 min	7.31	-3.1			
30 min	8.33	+10.4			
60 min	8.81	+16.7			

According to Mathew et al., the adjustment in annealing temperature reduced the resistivity. They described this phenomenon as follows: grain size rises with temperature, resulting in a reduction in grain boundaries and, hence, resistance. In addition, an ideal annealing temperature exists between 550 and 800˚C, above which the leakage current degrades and the effective dielectric constant drops [147, 154].

In contrast, Khan et al. evaluated the temperature-dependent change in the resistance of TiO_2 thin films exposed to light in their published study [141, 142, 155]. They discovered that the resistance value was reduced by a factor of 50, 100, and 200 at 300, 400, and 500˚C, respectively. They indicated that this would lead to a reduction

in grain boundaries and resistivity [147]. In reality, grain boundaries are the primary resistance source in metal oxides. Electrical resistance decreases as grain size increases and the number of grain boundaries decreases [156].

In this section of the research, the influence of test parameters on sheet resistance was explored. Increased coating speed and a shorter coating cycle result in thinner coatings. Thinner TiO_2 coatings on the conductive layer result in decreased resistance. The 1.6K and 32 cycles sheet resistance values of the thick samples were determined to be 8.58 and 9.36 Ω /sq, respectively. The FTO/TiO_2 resistances tend to decrease as the thicknesses diminish.

Temperature and annealing time influence not only the physical qualities, such as the increase in film density and decrease in film thickness, but also the morphological features, such as the increase in grain size and number of grain boundaries. The resistance values of the sheets grew linearly as the annealing temperature and duration increased. The resistance value decreased after 15 minutes of annealing at 350˚C. This could be due to the Cl-ions in the $TiCl_3$ precursor not being completely separated from the surface.

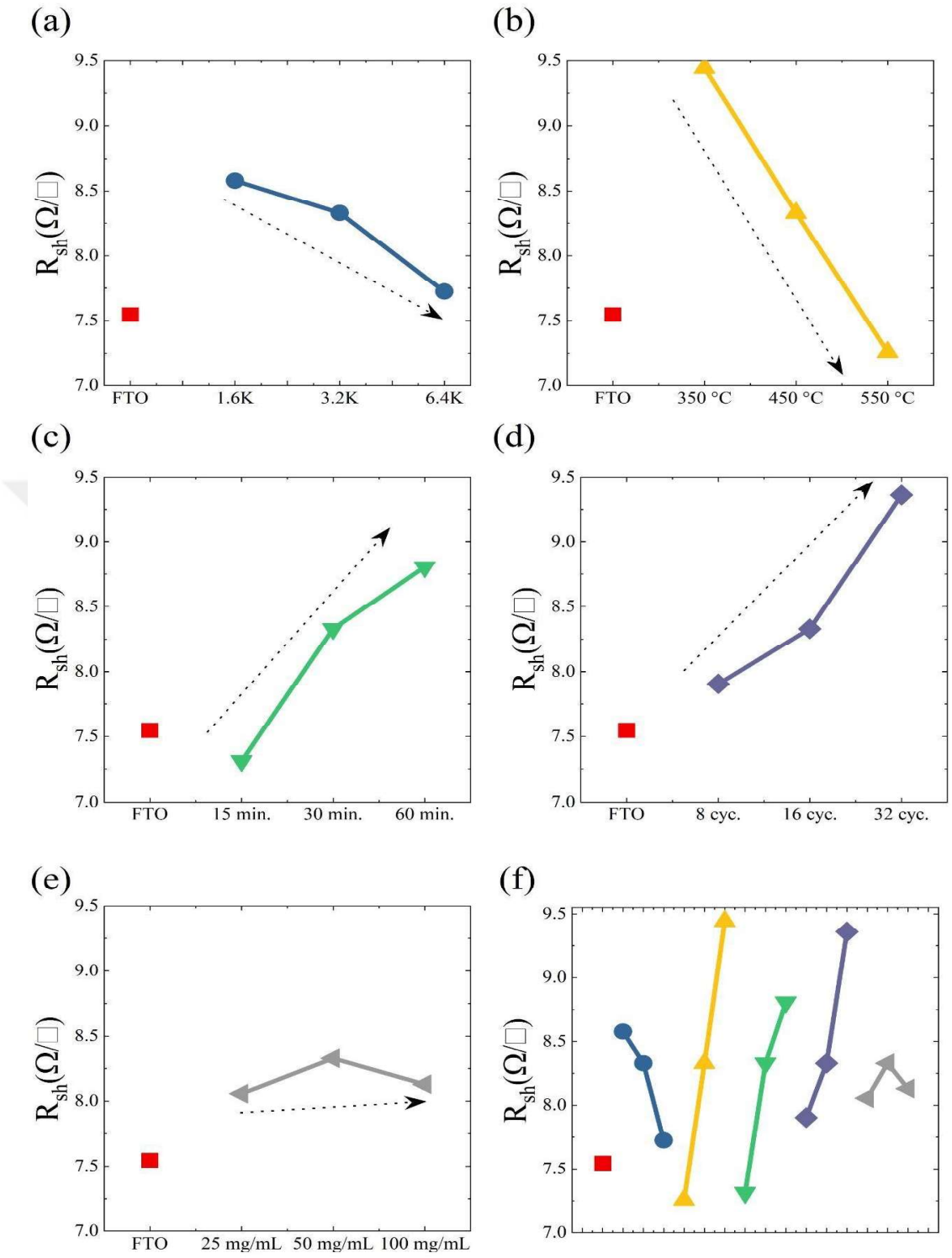


Figure 5.12 Comparison of the sheet resistance of FTO/TiO_2 layers formed to that of FTO and other coated films.

The sample annealed at 550˚C exhibited the greatest resistance increase, at 25.2%, followed by the sample coated 32 times, at +24.0%. The sample with a 16.7% annealing time of one hour follows. The sample coated with a rotation speed of 1.6K induced a +13.7% resistance increase. We've already mentioned that when particle size increases, resistance tends to decrease. The sheet resistance values we examined ranged from 8.06 and 8.33 Ω/sq, with no net increase being recorded. It is believed that this is due to the difference in thickness while operating in a very low molarity region where the difference is negligible.

5.1.4 EDS Analysis for Annealing Time and Temperature

The decrease observed in the resistance values brought into account the possibility that the chlorine group would not be completely removed. At this stage, EDS analysis was performed, and the mass analysis of the chlorine amount was performed. The exchange rate implies how much chlorine is removed from the environment. The counter map of the analysis results is presented in Figure 5.13. According to the results, samples annealed at 350 °C for 30 minutes and at 450 °C for 15 minutes contain relatively concentrated chlorine. Thus, the minimum temperature and time required to completely remove chlorine from the environment and transform the structure into titanium dioxide were determined as 450 °C and 45 minutes.

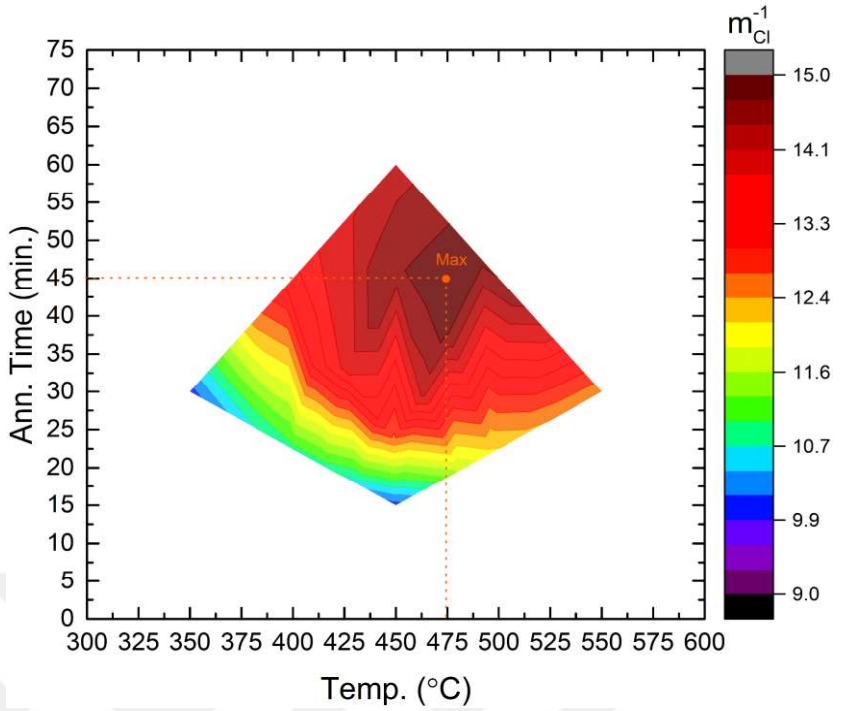


Figure 5.13 The average spectrogram of mCl^{-1} versus annealing temperature with annealing temperature. The point-intersected dashed lines represent the ideal chosen temperature and time to exclude all chlorides.

5.1.5 Figure of merits FTO/TiO_2 films

The figure of merit value (FOM), a typical performance parameter for transparent conductive oxides, was calculated for the FTO/TiO_2 compact layers [96, 157]. Standard FOM calculations are made with three different approaches. These formulas can be listed as follows:

$$\zeta_{Haacke} = \frac{T^{10}}{R_{sh}} \tag{4.1}$$

$$\zeta_{J\&K} = [R_{sh} \times \ln(T)]^{-1} \tag{4.2}$$

$$\zeta_{Gordon} = [R_{sh} \times \ln(T_{vis})]^{-1} \tag{4.3}$$

The relative relevance of transparency versus sheet resistance distinguishes these three techniques. To create an effective TCO material, it is necessary to maximize transparency and minimize resistance. Despite the fact that all equations demonstrate a linear connection with the R_{sh} value, the focus on transparency differs greatly.

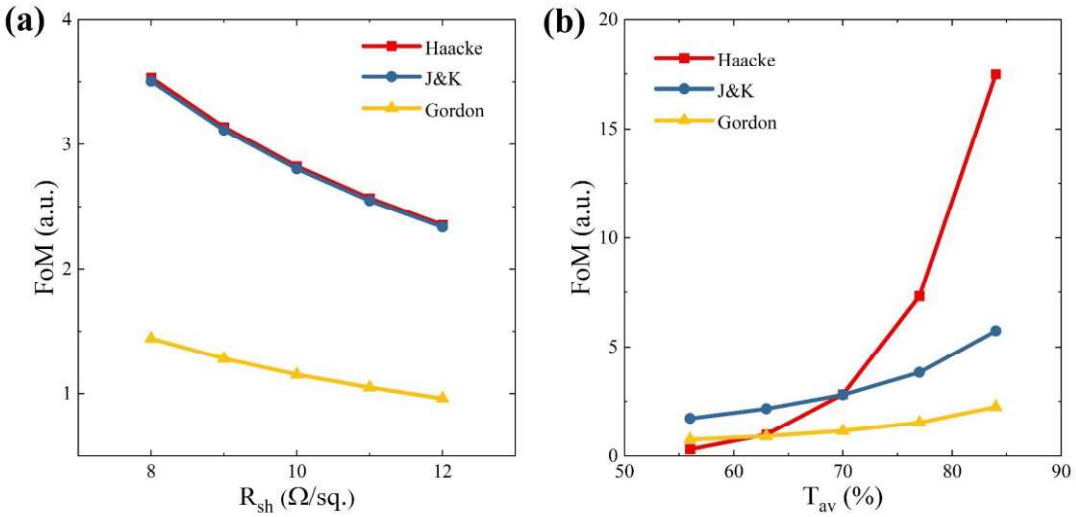


Figure 5.14 a) The effect of 10% Rsh change on FOM value under constant transmittance, b) Effect of 10% transmittance change on FOM under constant R_{sh}.

For instance, a 10% drop in R_{sh} increases the FOM value by 11.1%, but a 10% increase in transparency corresponds to an increase of 159.4% in the Haacke equation, 36.5% in the J&K equation, and 33.1% in the Gordon equation. Consequently, the importance placed on transparency differs.

In this section of the research, the FOM values of the FTO/TiO2 blocking layers were determined and shown in Figure 5.14. As previously indicated, because various formulae provide different values to the transparency parameters, the Haacke equation determined that 1.6K, 32 cycles, and 50 mg mL^{-1} were excellent, while 1.6K and 350 °C were superior.

Annealing has been found to have a strong influence on the structural, morphological, and optical properties of nanocrystalline TiO_2 thin films. Spin coating is one of the sol-gel processes, and it comprises numerous process

parameters that directly or indirectly affect the quality of thin films/layers, such as the molar concentration of precursors, spinning speeds, drop cycles, and thermal processing. Hence, optimizing the quality of thin films necessitates a deep understanding of the relationship between process parameters.

Previous research has demonstrated that an increase in precursor concentration results in larger grain dimensions [158] and an increase in surface roughness. With an increase in Spinning Speed, the Crystalline size and Texture Coefficient reduce [159]. According to the authors, a rise in annealing temperature increased the average grain size.

5.2 Ni-doped TiO_2/TiO_2 homojunction photoanodes

5.2.1SEM analysis of modified and bare particles

FE-SEM was used to investigate the morphologies of both photoanodes. As illustrated in Figures 5.15a and b, interconnected mesoporous films were produced, as evidenced using by the FE-SEM images of the top views of the samples. The particles seem to be spherical and are all the same size. The use of Ni dopant did not seem to have any visible influence on the form of the particles; nevertheless, there was a modest variation in the particle size. When doped with nickel, the findings show that the average particle size shifts from 20.92 nm to 23.09 nm, as shown in Figures 5.15c and d, respectively. Previous studies have shed light on how important it is to have an upper layer with a larger diameter than the TiO2 layer at the base of the structure. Therefore, the inclusion of Ni-doped TiO_2 particles on top of a layer of undoped TiO_2 may help facilitate effective light harvesting in certain circumstances.

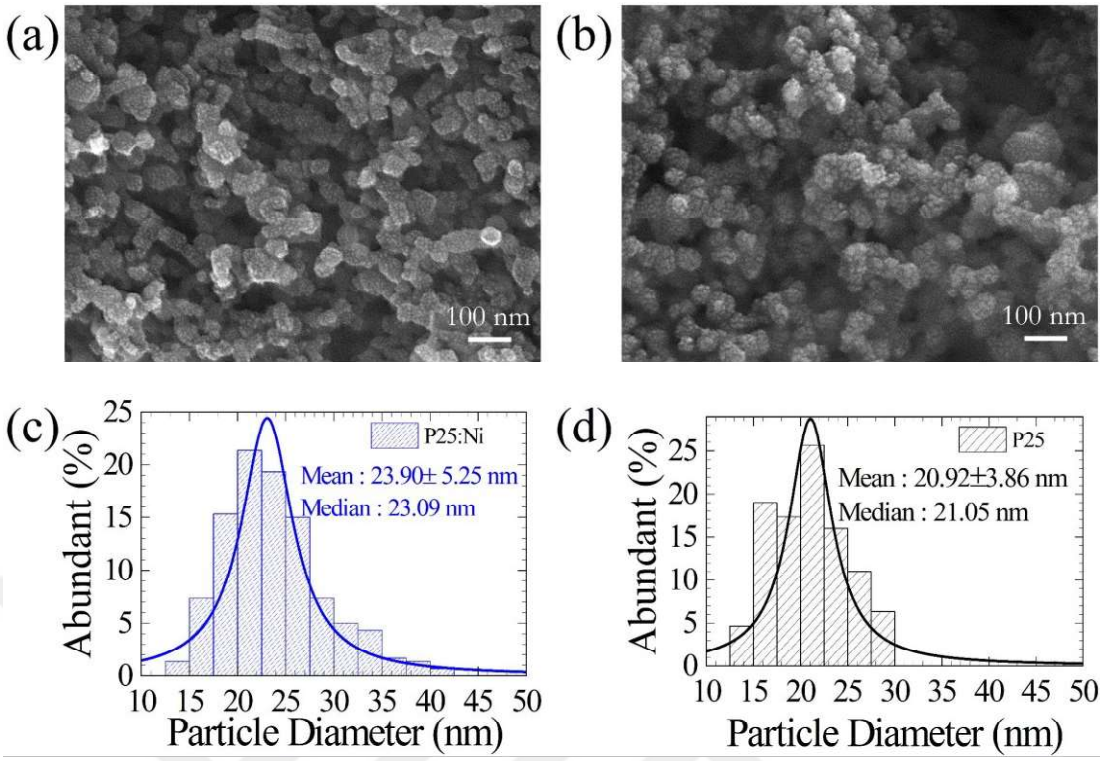


Figure 5.15 FESEM images of (a) Ni-doped, (b) bare P25 nanoparticles, and the particle distribution of (c) Ni-doped, (d) bare P25 nanoparticles. In order to find mean and median of particle sizes the abundant versus particle diameter graphs were fitted to Lorentzian equation

5.2.2 Elemental analysis of bare and modified P25 NPs

Studies using EDX were carried out in order to determine the chemical make-up of the materials. In Ni-doped TiO_2, the EDX spectra presented in Figures 5.16a and b demonstrate the presence of the elements titanium dioxide (Ti), oxygen (O), and nickel (Ni), with atomic ratio of 21.2 at. % (Ti), 78.7 at. % (O), and 0.1 at. % (Ni), respectively. In the other words, the ratio of nickel to titanium atoms is approximately 0.5 at.%. In a similar fashion, an undoped film had 30.3 at. % of Ti and 69.7 at. % of O as their respective elements.

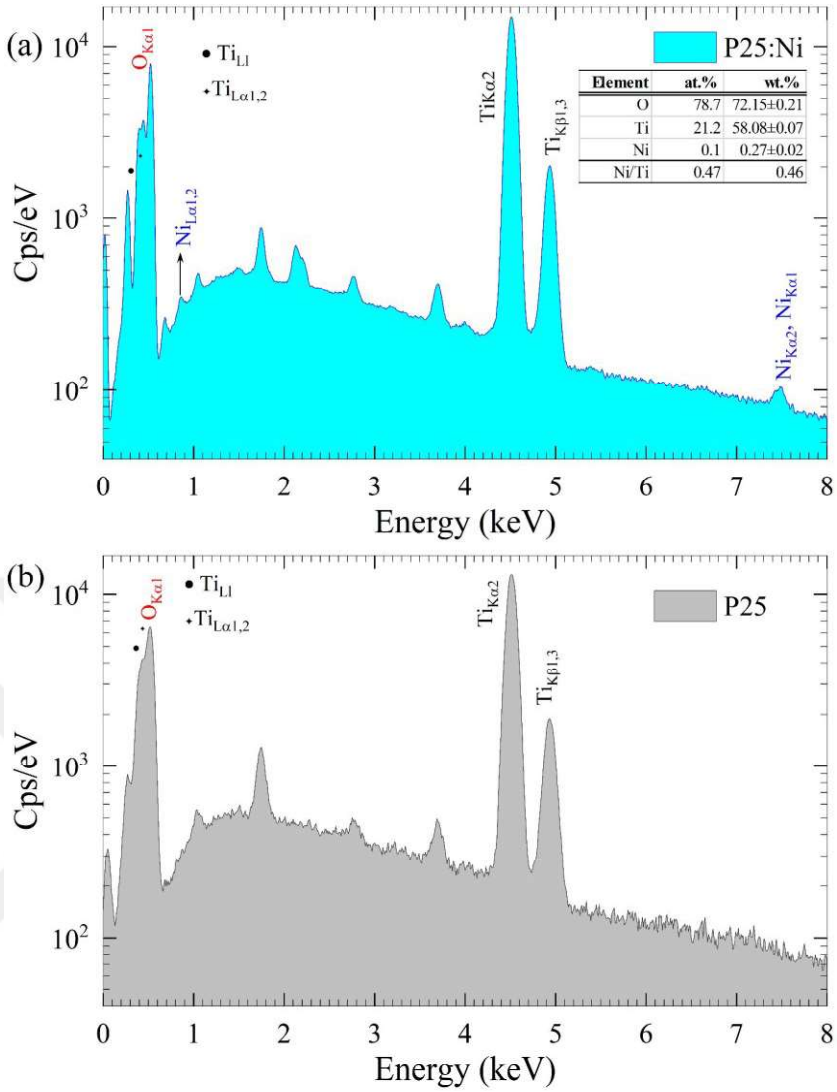


Figure 5.16 EDX spectra of (a) Ni-doped, and (b) bare P25 nanoparticles

The oxygen ratio is slightly higher than the titanium ratio; the excess oxygen may have originated from the substrate made of glass. Silicon, aluminum, calcium, and sodium are present in glass substrates as unmarked peaks in the EDX spectra. The nickel-to-titanium atom ratio is expected to be the same as the observed ratio of 0.5 at%.

5.2.3 XRD Anaysis of NPs

The X-ray diffraction (XRD) patterns of undoped and Ni-doped TiO_2 samples are shown in Figure 5.17. Both the anatase (JCPDS card no.02-0387) and rutile (JCPDS

card no.03-065-0192) phases of P25 have diffraction peaks that may be uniquely identified. The absence of secondary peaks in the XRD analysis indicated that Ni does not produce any secondary phases. This result demonstrated that the Ni atoms were effectively incorporated into the TiO2 crystal structure. Ni-doped TiO_2 sample's A (101) plane diffraction peak intensity was clearly higher than that of the undoped sample. Ni-doped TiO_2 has high crystallinity, as seen by the strong peaks in the XRD patterns.

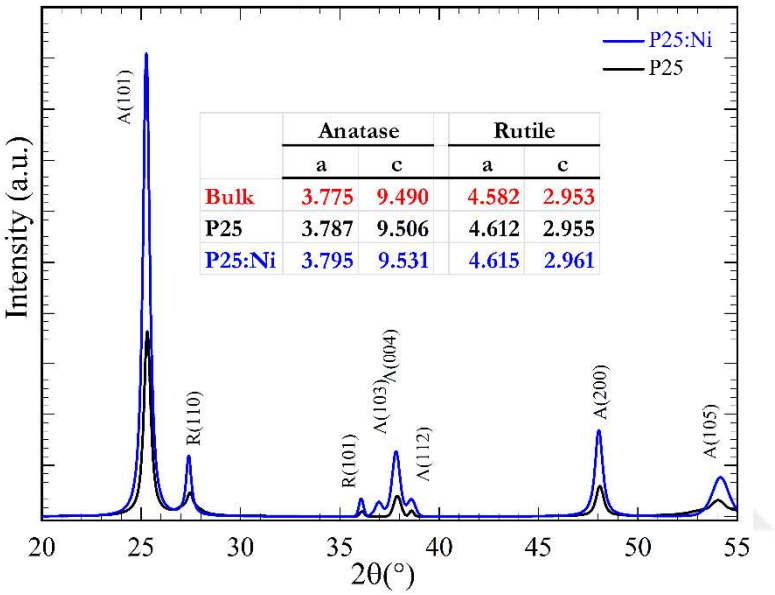


Figure 5.17 XRD patterns of bare and modified P25.

Scherrer's equation [160, 161] allows one to determine the crystallite size of both undoped and Ni-doped TiO_2 samples to be around 21 nm from the FWHM (fitted by the Lorentzian function) of the A (101). Diffraction peaks move to smaller theta values when Ni dopant is present because Ni^{2+} has a greater ionic radius than Ti^{4+} (0.69 vs. 0.61 Å). Sample calculations for the lattice cell parameters a and c in the inset of Figure 5.17 show that both parameters grow with Ni doping. This growth may likely be attributed to Ni^{2+}, which has a larger ionic radius [162].

5.2.4 Raman spectra of particles

Because it is sensitive to the presence of dopants, impurities, and crystal defects in the host-crystal lattice, Raman spectroscopy is a practical approach for investigating

the chemical bonding and solid-state structure of crystals. This method can be used to investigate crystals. Raman spectra of nanoparticles of bare P25 and those treated with nickel are displayed in Figure 5.18. The Raman spectrum of undoped (Ni-doped) TiO_2 has five vibrational modes at 143 (138), 197 (193), 398 (394), 518 (513) and 640 (635) cm^{-1}, which correspond to the Eg_1, Eg_2, B_{1g}, $A_{1g}+B_{1g}$, and Eg_3 peaks, which are comparable with prior literature findings [163, 164]. Since the Ni content is rather low, no phase shift is observed, and Raman studies confirm the efficient incorporation of the Ni dopant into the TiO_2 lattice.

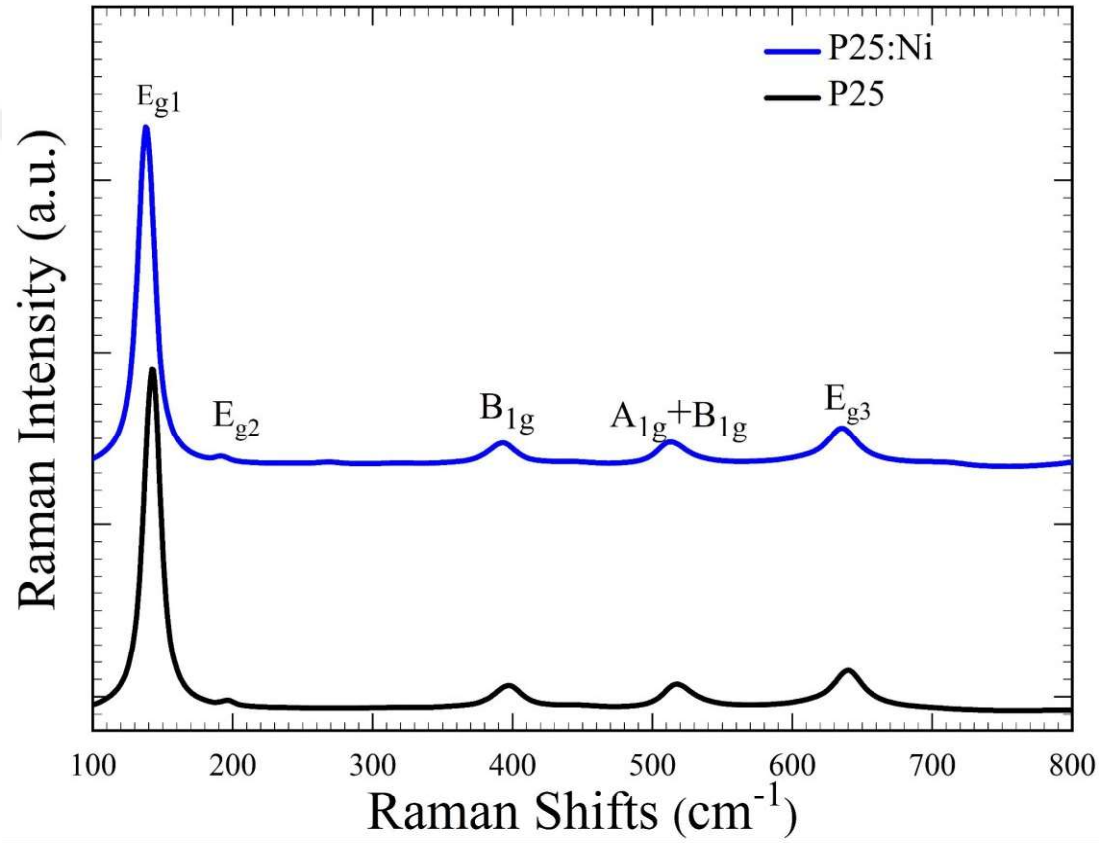


Figure 5.18 Raman spectra of undoped and Ni-doped TiO_2

This demonstrates that the structure remains intact after doping. The peaks shift to a lower wavenumber when Ni is doped. Xue et al. described a similar instance [160, 161, 164]. This change was responsible for a decrease in surface flaws. These results indicate that after Ni dopant reaches the lattice of TiO_2, surface defects [165] may be suppressed.

5.2.5 UV-Vis Spectra of PAs

In order to determine the optical absorption capacity of the undoped and Ni-modified P25 samples, UV-Vis absorption measurements were performed. Using the transmittance values of samples coated on microscope lamellae, the Tauc plot was utilized to calculate their band gap values (E_g). E_g is found to be 3.16 eV for undoped and 2.92 eV for Ni-doped TiO_2 samples, respectively. Eg drops was shrinkage with nickel doping.

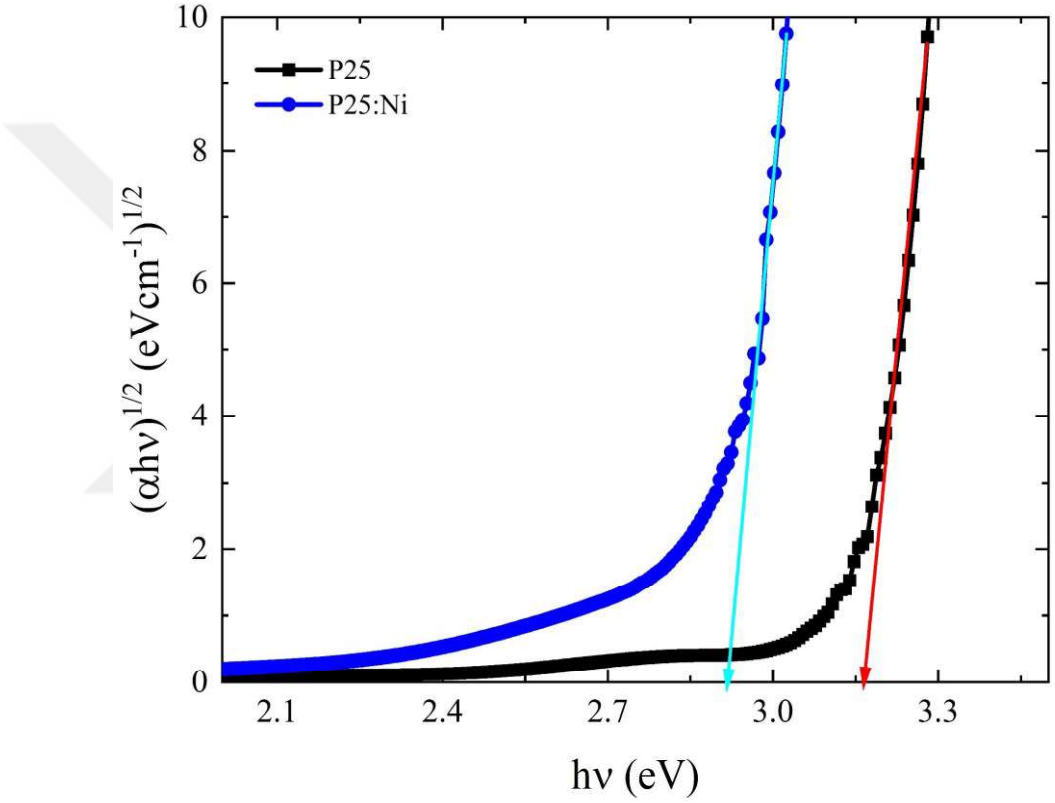


Figure 5.19 The Tauc's plots to determine the band gap value of undoped and Ni doped TiO_2

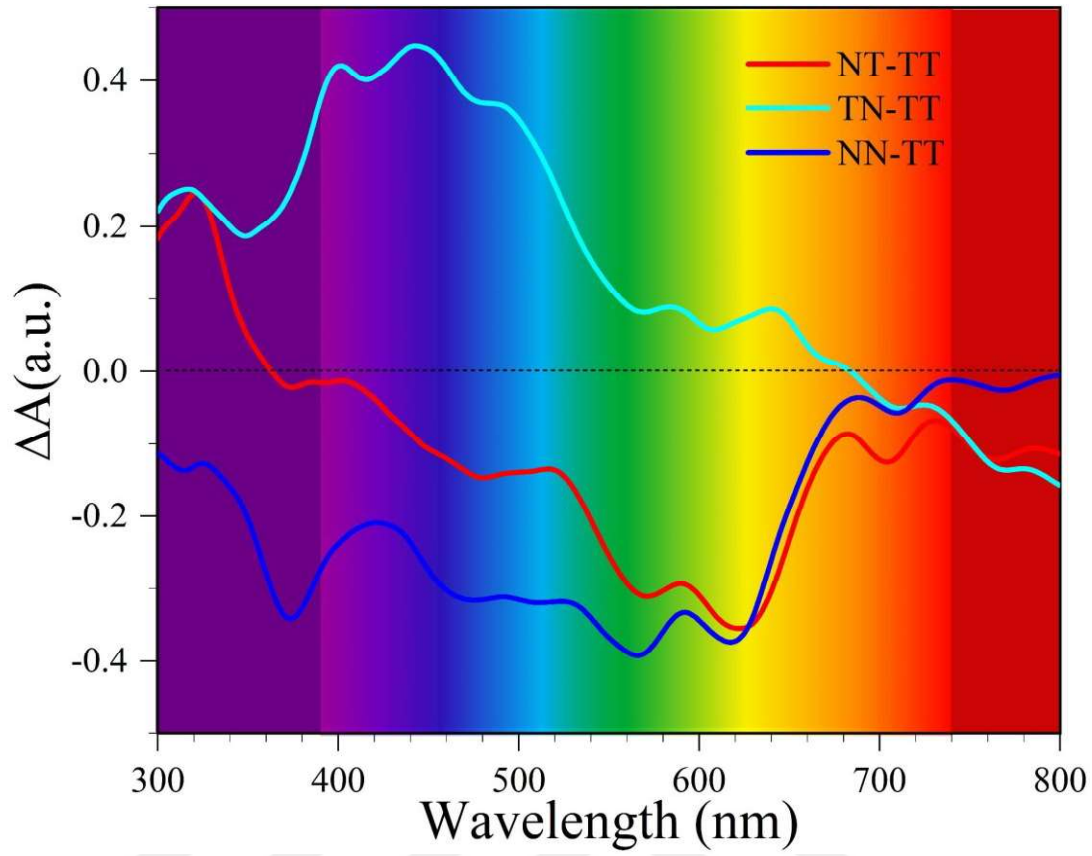


Figure 5.20 Relative UV-vis absorption spectra of the dye loaded photoanodes

UV-vis absorption spectroscopy may also be used to determine the optical characteristics of the bilayer composed of bare and modified TiO_2 in a variety of combinations. Figure 5.20 shows a comparison of the optical absorption spectra of four dye-loaded photoanodes. Here, ΔA represents the change in absorbance caused by modifying the bilayer structure combination in relation to TT. Figure 5.21 depicts the relative variation in absorbance between NT and TT, TN, and TT, and NN and TT as NT-TT, TN-TT, and NN-TT, respectively. For DSSCs to be more efficient, the light gathering must be enhanced. Instead of using thicker sheets, increased absorption may be achieved by enhanced light trapping [166].

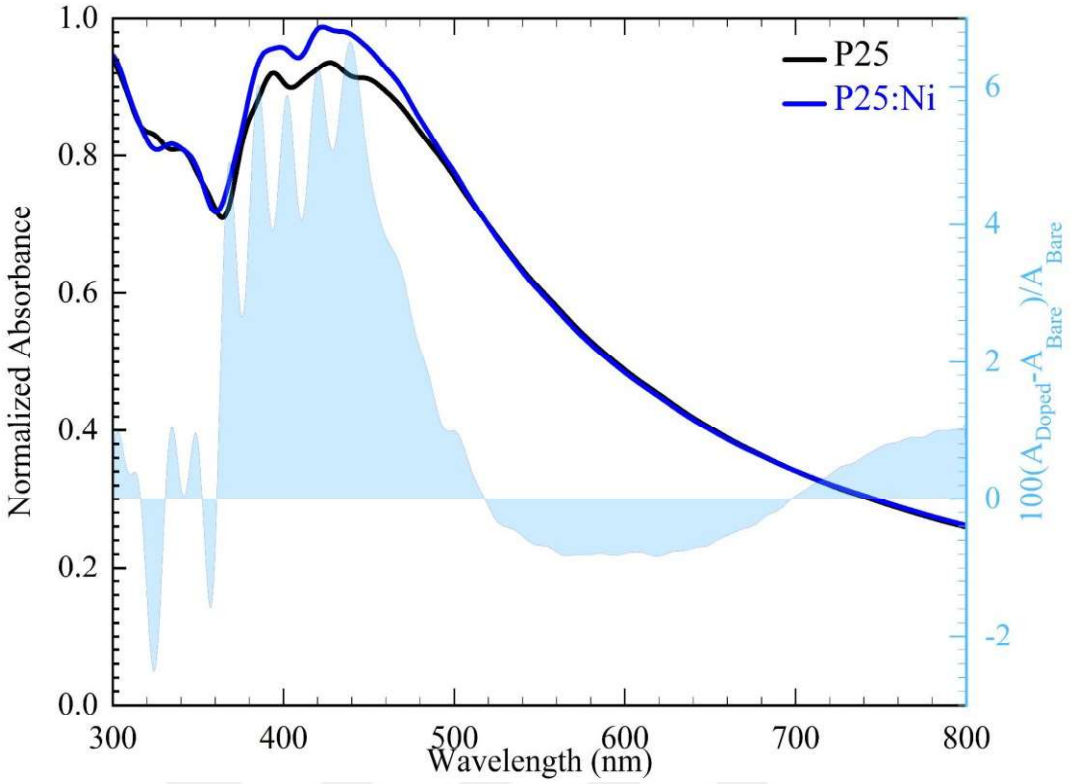


Figure 5.21 The absorption spectra and relative change according to wavelength of undoped and Ni doped TiO_2 mono layer thin films

The absorption spectrum may also be manipulated by altering the bilayer's mix and placement. Notably, the existence of a Ni-doped layer at the correct location may be compared to customizing absorption properties. Compared to the TT sample, the TN sample exhibited enhanced light absorption over the visible spectrum, particularly below 684 nm. This increases the amount of light that is absorbed, which is a key advantage for improving the short-circuit current of the devices [167]. The likely reason for the increase in light absorption is that the logically designed bilayer structure causes more light to scatter. In our particular instance, the larger particles (Ni-doped layer) in the top layer are able to both absorb more light and scatter it more uniformly, both of which are beneficial for the photoanode. So, adding a layer that scatters light (a Ni-doped layer) makes solar cells work better because they can absorb more light. Because of this, the absorption values of both the NN and NT samples are lower than those of the TT sample between 360 and 800 nm. This is mostly because there is no scattering layer on top of the NN and NT samples. Even though the size of the crystals changes when Ni is added to TiO_2, there is a big

difference in how well it absorbs. Similar things have been said about Ni-doped TiO_2 and other metal-doped TiO_2 [167, 168]. With just a 2 nm change in the size of the Ni, the absorbance of TiO_2 changed in a big way [169]. This change in absorbance was also thought to be caused by changes in the samples' reflectance and roughness on the surface [169].

5.2.6 The flat-band potential

The flat-band potential (V_{fb}) of these PAs in various combinations is determined via MS analysis, as shown in Figure 5.22, in order to better understand the physical causes of the changes in their attributes. The following equation may be used to fit the Mott Schottky curves:

$$\frac{1}{C^2} = \frac{2}{\varepsilon\varepsilon_0 A^2 e N_d}\left(V_{app} - V_{fb} - \frac{k_B T}{e}\right) \tag{4.5}$$

where C, ε, ε_0, A, e, N_d, V_{app}, k, and T denote the differential capacitance of the space-charge region, the dielectric constant of TiO_2, the permittivity of free space, the active area, charge of electron, electron density, applied voltage, Boltzmann's constant, and temperature, respectively. The values of V_{fb} and N_d can be extracted by extrapolation to $1/C^2 = 0$ and from the slope of the curve, respectively. The fitting parameters are V_{fb} = -0.14, -0.17, -0.26 and -0.49 V; N_d =1.78×1021, 3.37×1021, 3.40×1021 and 3.72 ×1021 cm-3 for TT, NN, NT, and TN, respectively. Ni-doped photoanodes (NN, NT, and TN) have a greater N_d value than their undoped analogues (TT). The greater N_d value may enhance the performance of a cell.

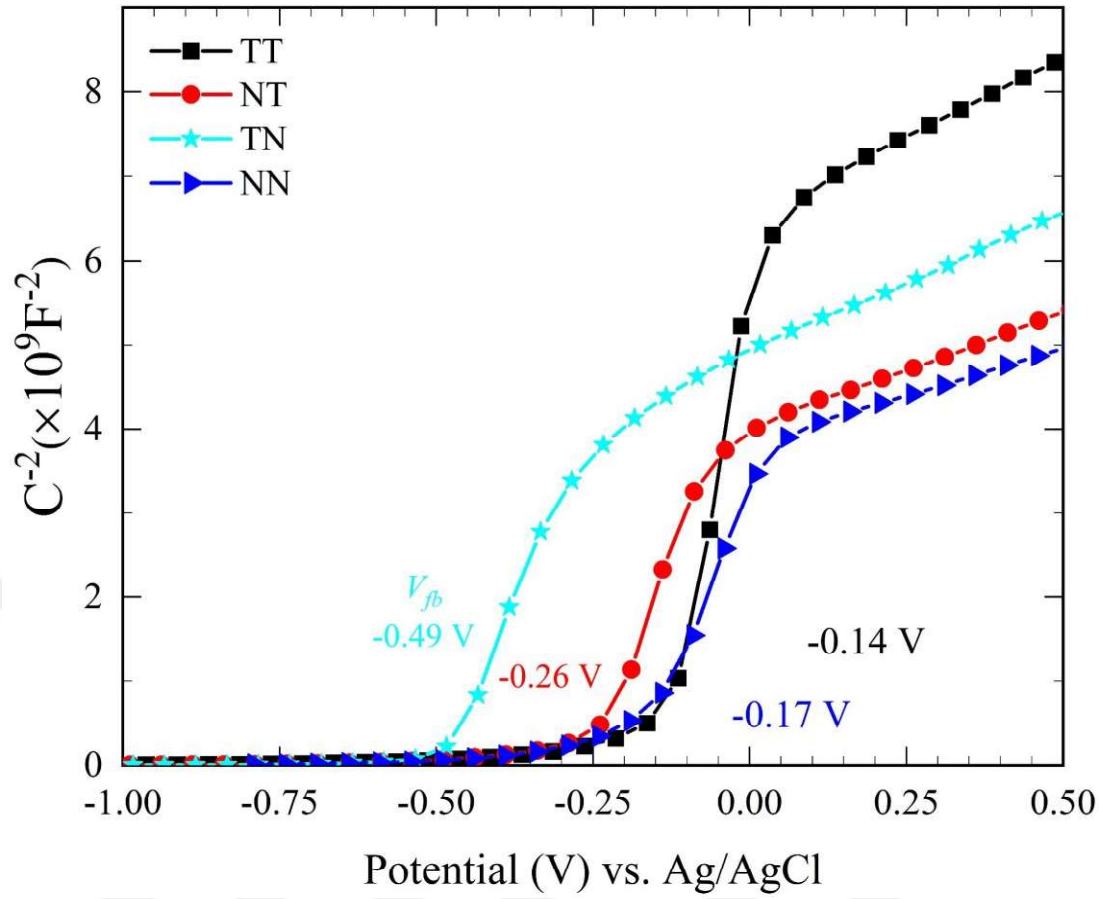


Figure 5.22 Mott-Schottky curve of photoanodes

Due to the tiny quantity of Ni dopant, the rise in Nd implies that the carrier type (n-type for TiO_2) of photoanode material stays unchanged [170]. The fitting curve demonstrated a negative shift of the V_{fb}, confirming an increase in the conduction band edge (E_c) from undoped (TT) to Ni-doped photoanodes (NN, NT, TN). This also verifies the upward movement of the Fermi level. Likewise, Archana et al. showed that Ni doping causes E_c to change to a negative value, which considerably increases the open circuit voltage (V_{OC}) [165]. In TiO_2, the 3d (Ti) and 2p (O) orbitals create the conduction and valence bands. Ec and the valence band edge (E_v) are shifted higher by the Ni (3d) orbitals [165]. Ni doping reduces the band gap from 3.21 to 2.92 eV at a rate of 0.5 Ni/Ti [162]. By adjusting E_c to higher negative values, the disparity between the Fermi level of the photoanode material and the redox potential of the electrolyte increases, so V_{OC} should rise. Moreover, a rise in E_v indicates a rise in short-circuit current (J_{SC}). In contrast, for other dopant materials, attaining both E_c and the valance band edge (E_v) changes simply needs the addition

of Ni doping, which in most instances has a significant impact on both increased V_{OC} and J_{SC}, hence enhancing the device's conversion efficiency.

5.2.7 Photovoltaic performance parameters

To evaluate the photovoltaic performance of dye-sensitized solar cells manufactured with TT, NT, TN, and NN PAs, the J-V characteristics of the devices were analyzed With a TN photoanode consisting of undoped TiO_2 and Ni-doped TiO_2 as the bottom and top layers, respectively, optimal photo-conversion capabilities were attained. The J-V characteristics of the optimized cells are shown in Figure 5.23, and Table 5.2 provides a summary of the device parameters. Notable is that the values of our calculated parameters for devices constructed with various photoanodes are in good accordance with those published in the literature [141, 171-173]. Devices with TT, NT, TN, and NN photoanodes had mean PCE values of 4.38±0.07, 4.35±0.1, 6.04±0.06 and 4.08±0.04 with Voc values of 0.585, 0.639, 0.627, and 0.586 V, respectively.

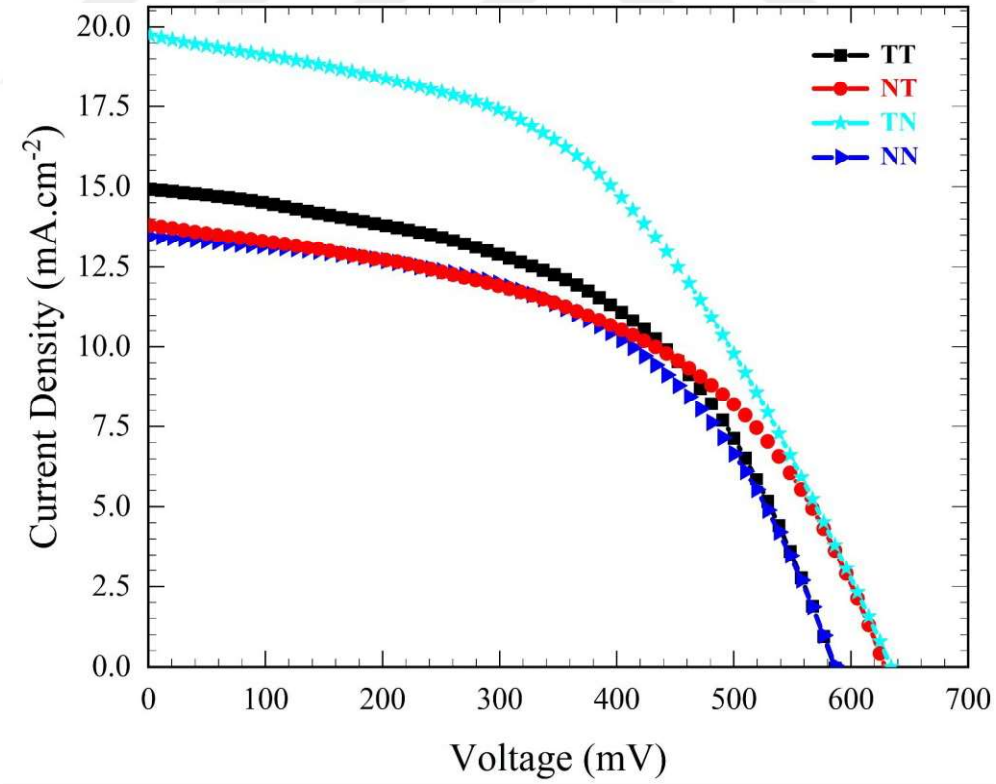


Figure 5.23 J-V curve of the devices based on various photoanodes.

The trends in V_{OC} values mostly correspond to those predicted from an assessment of Mott-Schottky analysis revealing energy differences across possible flat-bands. However, a built-in potential might arise at this junction of undoped and Ni-doped layers despite the fact that the concentration gradient between the layers is not very large [141, 174]. This differential may still limit the back recombination of dye-injected electrons with E_c. Due to the difference in location of Fermi levels, a homojunction is created when an undoped layer meets a Ni-doped layer. To balance their Fermi levels, a band bending is formed, which enables the flow of electrons from the Ni-doped layer to the undoped layer. Such an inherent voltage facilitates electron transit and inhibits charge recombination. The higher open-circuit voltage of NT and TN in comparison to TT and NN indicates the benefit of TiO_2 homojunction with the existence of an inherent voltage at the homointerface. Therefore, electron recombination is inhibited, and recombination resistance increases, leading to a greater V_{OC}.

Compared to the values of V_{OC} and FF published in the literature for DSSCs, their levels in our situation are comparatively low. For V_{OC}, this can be explained by the quality of the crystal in the photoanode and the level of redox potential in the electrolyte. The poor FF of the devices is most likely the result of low V_{OC} and a high defect concentration inside the structures [142]. The J_{SC} values for devices having TT, NT, TN, and NN were 14.96, 13.01, 20.58, and 13.46 $mA \cdot cm^{-2}$, respectively. These J_{sc} values correspond nicely to the trend in light absorption (Figure 5.23). Due to incorrect band alignment, photogenerated electrons cannot be readily transmitted from the undoped to the Ni-doped layer for NT and then to the back electrode via the undoped layer. Consequently, J_{SC} will decline. The device containing the TN photoanode with the greatest J_{SC} value has the maximum absorbance. Based on the above studies, the TN photoanode plays an essential role in achieving increased performance.

Table 5.2 Photovoltaic performances of the DSSCs based on different photoanodes measured under simulated 100 mW/cm^2 AM 1.5 illumination. *Average values from 5 devices.

Photoanode	J_{SC} (mA/cm^2)	V_{OC} (V)	FF	η (%)*
TT	14.96	0.585	0.51	4.49 (4.38±0.07)
NT	13.01	0.639	0.54	4.47 (4.35±0.10)
TN	20.58	0.627	0.47	6.08 (6.04±0.06)
NN	13.46	0.586	0.52	4.13 (4.08±0.04)

5.2.8 EIS measurements

To further investigate the electron transport kinetics and recombination in devices with differently built photoanodes, an EIS analysis is performed, and the related parameters are reported in Table 5.3. To estimate EIS parameters, we used a circuit equivalent shown in the inset of Figure 5.24b.

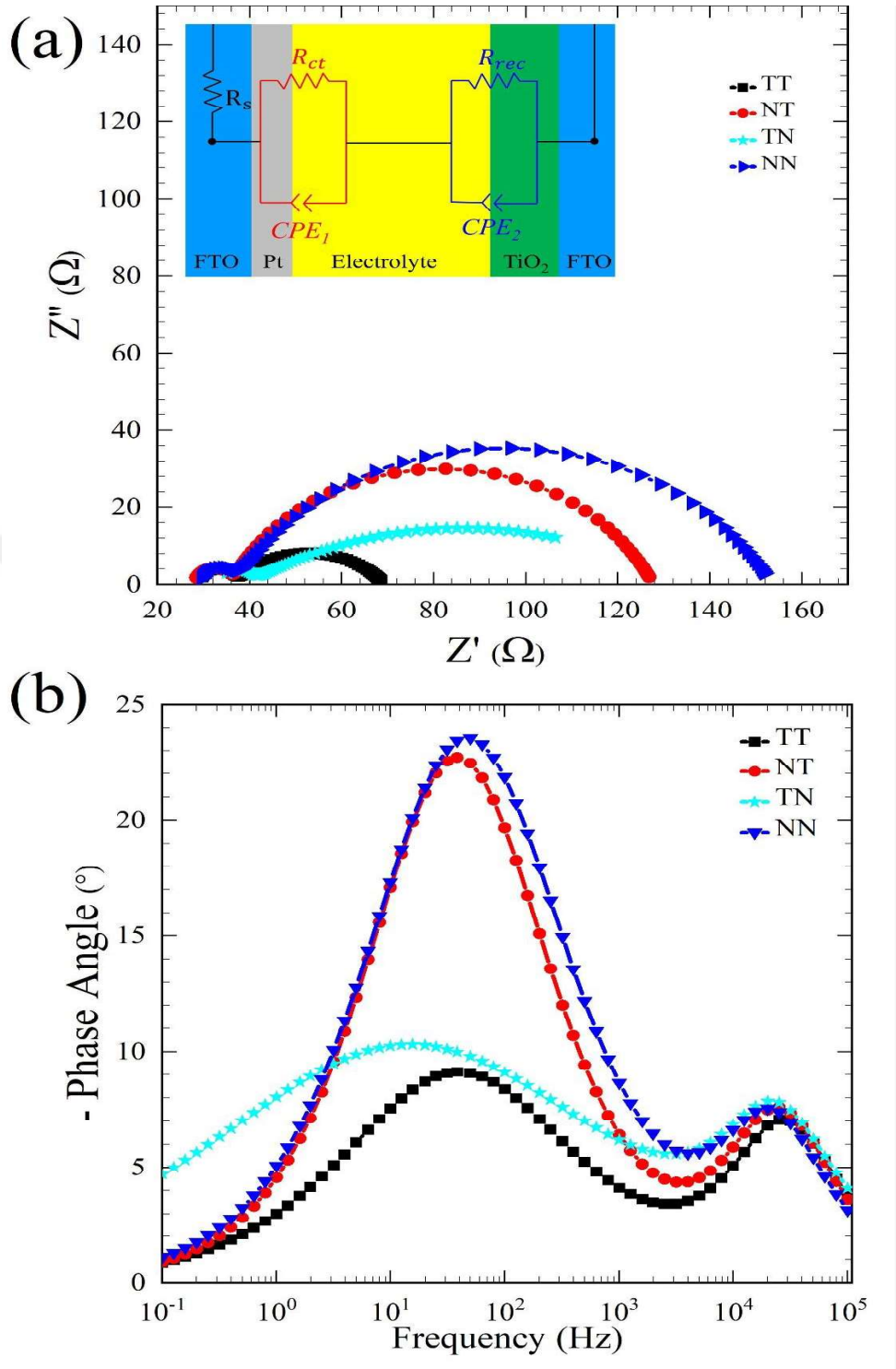


Figure 5.24 (a) On the basis of various photoanode Nyquist plots, EIS measurements for the devices were performed. (b) Plots of Bode phase angle versus frequency.

In Figure 5.24a's Nyquist plots of EIS spectra, all devices exhibit two well-defined semicircles in the low and high frequency areas. The high frequency offset is also attributed to the device's series resistance (R_s), which is typically derived from the FTO resistance. In our situation, it is around 30 Ω, which has a bad impact on the FF of the devices [175, 176]. In the higher frequency area of the Nyquist plot, smaller semicircles developed, which correspond to the charge transfer resistance (Rct) at the counter electrode/electrolyte and FTO/electrode interfaces. As seen in Table 5.3, the Rct value fluctuates somewhat depending on the photoanode configuration. Since all devices use the same counter electrode and electrolyte, this difference in Rct may be attributed to the FTO/photoanode interface. It falls in a device with a TN photoanode, implying a faster electron transport mechanism, improved charge collection efficiency, and an increase in J_{SC} [108, 177].

Recombination resistance (R_{rec}) at the electrode/electrolyte/dye interfaces accounts for the bigger semicircles seen in the lower frequency area. According to the Nyquist plots, the semicircle for NN, TN, and NT photoanodes is greater than that for the TT photoanode, demonstrating that R_{rec} increases following the introduction of Ni. This data shows that Ni photoanodes have reduced recombination rates at the electrode/electrolyte/dye interfaces. For further study of the charge recombination process at electrode/electrolyte/dye interfaces, the frequency peak position (f_{max}) of the EIS semicircle in the Bode plots (Figure 5.24b) is used to derive the electron lifespan provided by

$$\tau_n = \frac{1}{2\pi f_{max}} \tag{4.6}$$

A longer electron lifespan implies a lower rate of charge recombination. Figure 5.24b demonstrates that the device built with a TN photoanode shifts fmax to a lower value, resulting in a longer electron lifetime of 10.18 ms and a remarkable reduction in charge recombination.

A longer electron lifespan implies a lower rate of charge recombination. Figure 5.24b demonstrates that the device built with a TN photoanode shifts fmax to a lower

value, resulting in a longer electron lifetime of 10.18 ms and a remarkable reduction in charge recombination.

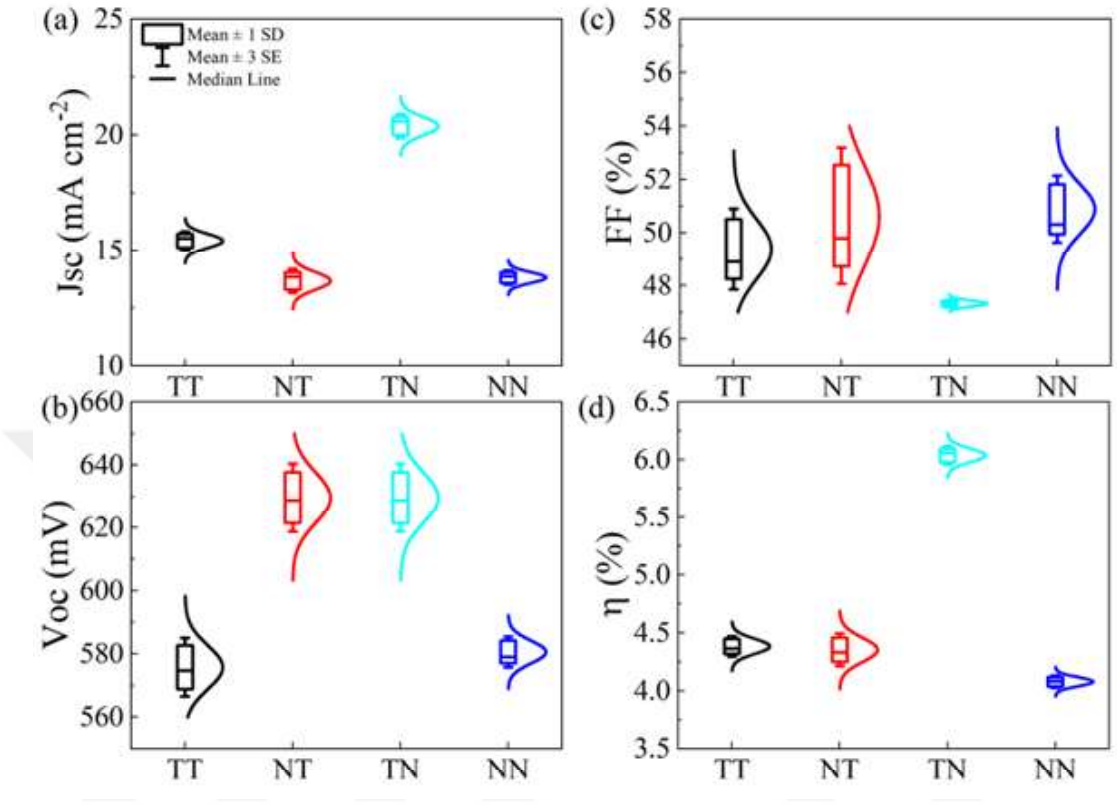


Figure 5.25 The statistical distribution of the photovoltaic characteristics of DSSCs with different placements of modified layer (a) distribution of J_{SC} (b) V_{OC} (c) FF (d) PCE. The J-V curves are used to extract parameters under AM 1.5 conditions. Five 0.16 cm^2 cell active area devices have been produced for each DSSC assembly.

Figure 5.25 (a–d) depicts the statistical distribution of all photovoltaic characteristics for five devices with varying doping layer positions. The device using a TN photoanode has greater photovoltaic characteristics, particularly the J_{SC} and V_{OC}. The dispersions of Jsc clearly illustrate that the presence of an upper nickel modified TiO_2 layer improves the performance of the devices in comparison to other layers.

Table 5.3 Parameters determined by EIS for the devices assembled with different photoanodes

Photoanode	R_s (Ω)	R_{ct} (Ω)	R_{rec} (Ω)	τ_n (ms)	C_μ (μF)	L_n (μm)	τ_d (ms)
TT	29	7.33	33	4.19	68.61	33.9	0.50
NT	28	7.71	92	4.21	42.85	55.3	0.33
TN	33	6.09	95	10.18	19.40	63.2	0.12
NN	29	7.80	117	3.18	23.61	62.0	0.18

In addition to the recombination resistance and lifespan, another essential metric used to quantify electron transport is the chemical capacitance (Cμ), which is therefore a significant figure of merit for DSSCs. The C_μ generated by the buildup of electrons in the metal-oxide layer outlines the fluctuation in electron concentration caused by a modest change in the Fermi level because of doping. Both the overall density of mobile electrons in the Ec and the confinement of immobile electrons in the trap states [169, 178, 179] influence the value of C_μ. Additionally, it aids in comprehending the nature of traps inside the framework. It is anticipated that the value of C_μ with fewer trap states would be reduced due to poor electron trapping. Table 5.3 lists the values of C_μ estimated from EIS for devices constructed with various photoanodes. After Ni inclusion in the photoanode, the C_μ decreases significantly. A portion of this drop is attributable to a decrease in the number of immobile electrons trapped by defect states [178, 180], supporting the enhanced electron transport in Ni-doped photoanodes. Consequently, one might anticipate a rise in V_{oc}. C_μ drops in value in the following order: TN <NN < NT < TT (Table 5.3). The chemical capacitance of the devices constructed with TN and NN photoanodes is drastically lowered. V_{OC} (TN) is likely greater than V_{OC} (NN) owing to the syngeneic impact of the negative shift in V_{fb} and the decrease in C_μ. As previously stated, V_{fb} (NN) is less than V_{fb} (TN), hence the NN photoanode is

inadequate for DSSCs. Ultimately, the study demonstrates that improved performance is possible with a bilayer (TN) architecture, which is advantageous for DSSCs.

We computed the electron diffusion length (L_n) and the electron transport time (τ_e) in order to further characterize the transport properties of the cells. These values may be found in the following equation [181]:

$$L_n = L\sqrt{\frac{R_{Rec}}{R_{CT}}} \tag{4.7}$$

$$\tau_d = R_{CT}C_\mu \tag{4.8}$$

where L is the photoanode layer's thickness. Table 5.3 provides a recap of the derived values. The calculated parameter values are consistent with those of earlier published investigations [108, 182]. L_n is the distance traveled by electrons prior to recombination. L_n must be larger than the PA thickness for PCE performance to be optimal [183, 184]. A longer L_n seen after Ni inclusion may be the result of surface trap states being neutralized by doping [108]. Consequently, the density of photo-injected electrons reaching the back electrode increases as L_n increases. A shorter length suggests a faster electron transport rate, which may also contribute to a greater J_{SC} [173]. It's possible that the eligible junction structure of the device constructed with a TN photoanode is responsible for the device's faster electron transit. Consequently, the device manufactured with a TN photoanode might have a greater charge collection efficiency, which is defined as the proportion of injected electrons arriving at the back electrode without being recombined.

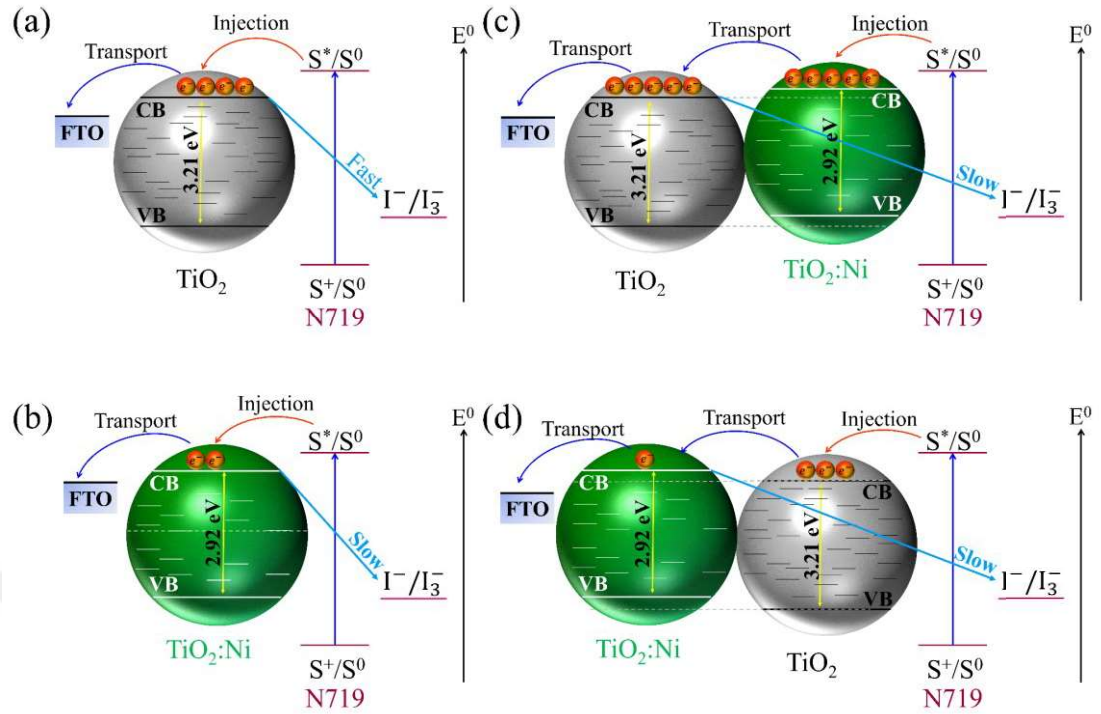


Figure 5.26 Schematic illustration of DSSCs containing different photoanodes of (a) TT, b) NN, c) TN, and d) NT

In order to clarify the band alignment and charge transfer in devices with varied photoanodes, we drew a schematic of DSSCs as shown in Figure 5.26. Ni dopant inhibits the back transport of electrons from the photoanode to the electrolyte, hence delaying recombination. Consequently, R_{rec} increases after the insertion of Ni dopant into the photoanode. R_{rec} grows in value as follows: TT < NT < TN < NN (Table 5.3). Even though the device with NN has a higher R_{rec} value, the change in V_{fb} to more negative values is much smaller, which lowers V_{OC}.The V_{OC} of the device constructed with TT is almost identical to the V_{OC} of the device assembled with NN. In addition, the capacity of NN to absorb TT is diminished (Figure 5.23), hence reducing J_{SC}. Consequently, compared to the device constructed with a single layer of undoped TiO_2 (TT), the device assembled with a single layer of Ni-doped TiO_2 (NN) photoanode has a negative impact on the device's overall efficiency. In addition, we investigated the effect of changing the photoanode structure from a single layer to a bilayer on the performance of the devices. Initially, this merits a higher V_{OC} value. V_{OC} 's value grows in the following sequence: TT ~ NN < NT ~ TN (Table 5.2). Comparing the devices produced with NT and TN photoanodes

reveals that incorrect band alignment between the TiO_2 and Ni-doped TiO_2 layers in the device assembled with the NT photoanode weakens electron transport from the E_c to the back electrode. L_n (TN) = L_n (NT) if the difference in carrier concentrations between two layers of the junction is small and the diffusion lengths are close to one another (NT). V_{oc} (TN) ≈ V_{oc} (NT) despite the fact that V_{fb} (TN) > V_{fb} (NT), since this circumstance likely compensates open-circuit voltage (NT). The capacity of NT to absorb light is similarly inferior to that of TN. Therefore, Jsc (NT) will continue to lag the competition, resulting in decreased efficiency. In contrast, it is noteworthy that the J_{sc} of the device constructed using a TN photoanode is much higher than that of the NT. This value corresponds to those presented in the literature [185]. This high value of Jsc may also be attributed to Ni doping, which may result in fewer structural flaws. It is primarily attributable to proper band alignment, higher light absorption (UV-vis), enhanced injection from dye to E_c, rapid electron transport from E_c to the back electrode, and improved collection efficiency for the device assembled with the TN photoanode, resulting in a notably improved device performance.

5.3 Optimization of Electrolyte

5.3.1 Introduction

While photography initiated the electrochemical process in the early 19th century, research on the electron transfer process of oxide semiconductor material did not begin until the 1960s. The efficiency of these cells was less than 1%, and they were made up of single crystals of tin oxide that had been coated with chlorophyll. TiO_2 nanoparticles featuring a significantly increased surface area and enhanced capacity for dye loading were utilized in the development of this design. Sensitized dyes based on ruthenium or osmium have begun to replace chlorophyll because of their ability to rapidly inject electrons when triggered by sunlight. Following the completion of these innovations in 1991, Gratzel and O'Regan achieved a transformation efficiency of 7.1% for the first time. Since then, the power conversion efficiency of DSSCs has increased to 15.2% thanks to the implementation of new technologies connected to the materials and design processes of the devices.

Electrolyte compositions with alternative redox services have a meaningful effect upon such an increase in PCE [45, 154, 186-189].

Traditional iodide/triiodide redox shuttle-based electrolytes have rapidly been replaced with alternative redox couples to circumvent the inherent bottlenecks that are inherent to these electrolytes. Cobalt and copper redox shuttle-based electrolytes have attracted substantial attention among the numerous possibilities [188, 190, 191]. This is largely because many of their distinctive properties, such as rapid dye regeneration with low driving force, lower absorption in the visible spectrum, the ability to achieve voltages greater than 1 volt, and high compatibility with alternative catalyst materials, have been uncovered.

In the present day, DSSCs that use $[Co(phen)_3]^{2+/3+}$ redox couple-based electrolyte formulations have achieved conversion efficiencies that are greater than 14%. During the development of next-generation DSSC devices, this solar-to-electrical conversion efficiency with Co electrolytes has been claimed to be the highest to date. In a manner analogous to that of cobalt redox shuttles, the capability of modifying the redox potential of copper redox complexes using ligand engineering enables the prospect of improved redox potential matching with the HOMO level of the dye. Therefore, it is possible to obtain a larger V_{OC} (more than 1 V) while still retaining excellent short current densities, as several publications have revealed. The use of $Cu(tmby)_2]^{1+/2+}$ redox couple-based electrolyte has led to the recording of the highest power conversion efficiency to date, which is greater than 15%.

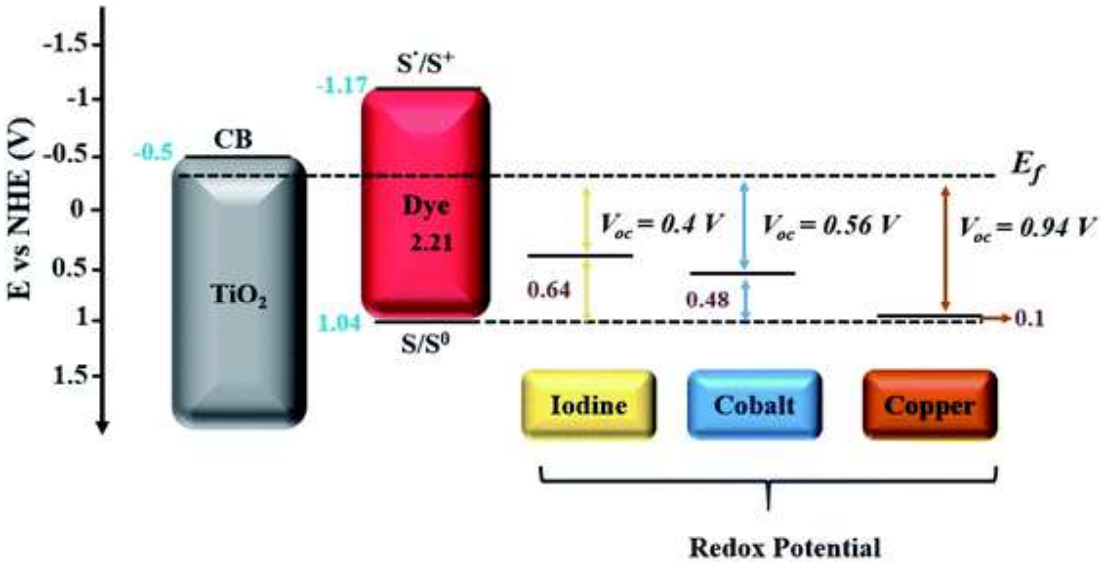


Figure 5.27 The energetics of DSSCs in relation to the redox potentials of each of commonly used redox couples that are employed in DSSCs [191].

Ionic liquid is one of the fundamental components of DSSCs, and it plays a crucial role in determining the open circuit voltage and even the efficiency of power conversion. The V_{OC} value is determined by the difference between the Fermi level of the semiconductor material used in the photoanode and the redox potential of the electrolyte. The estimated minimum driving force necessary for regeneration is approximately 0.1 eV. This indicates that a redox couple has a more positive redox potential than the homo level of the dye. This results in a lower loss of energy during the process of regenerating oxidized dye, which in turn results in a higher open-circuit voltage.

In this section of the thesis, commonly used prescriptions were applied to Ni-doped TiO_2/TiO_2 homojunction photoanodes. JV measurements were used to determine which electrolyte was best suited to the designed structure. The electrolyte used EIS and CV spectroscopies to understand and explain the working mechanism of the assembled cell. Also, UV spectroscopy was used to compare the optical properties of different electrolytes.

5.3.2 Specifications of electrolyte components

Liquid electrolytes rely on the organic solvent, which facilitates the solubilization and transport of ionic conductors. Solvents used in DSSCs should meet the following broad criteria:

i. The melting point must be below -20 °C and the boiling point must be above 100 °C, depending on how the cell works. This is important not only for lab use but also to keep the material from evaporating or freezing in the outdoor environment.

ii. The solvent's chemical stability must be sufficient both in the dark and in the light.

iii. The solvent must have a high dielectric constant. Thus, electrolyte salts are well soluble and are found completely decomposed in the solution.

iv. The solvent must have low viscosity. Thus, redox mediators with high diffusion coefficients and liquid electrolytes will have high conductivity.

v. low light absorption.

vi. inertness with respect to the surface-attached dye, including the dye-metal-oxide (or another semiconductor) bond.

vii. poor solubility to the sealant materials.

viii. low toxicity and low cost.

Noteworthy is the fact that no single solvent can simultaneously fulfill all the requirements; these requirements for a single solvent are frequently contradictory in multiple ways. To achieve optimal DSSC performance, therefore, mixed solvents are frequently employed.

The physical properties of the most commonly used solvents are tabulated in Table 5.4. Due to its low viscosity, good solubility, and excellent chemical stability, acetonitrile (AN) is regarded as the best electrolyte for basic research [192].

However, AN is the preferred solvent for laboratory research on new sensitizers, particularly when it is desired to maximize cell efficiency, as photochemical processes occur in this solvent without mass transport limitations. Utilizing AN, the literature's highest efficiencies, such as 14.3% and 15.2%, were achieved. However, the relatively low floating point can be limiting, so they are combined with high-boiling nitrile group solvents such as VN, BN, and GN to eliminate this drawback. It is another solvent in the nitrile class with low toxicity and a high boiling point, like 3-methoxypropionitrile (MPN). MPN has a melting point of -63 °C, a boiling point of 164 °C, and a viscosity of 2.5 cP; it is one of the most frequently used electrolyte solvents in modern applications. The MPN is remarkably stable, with less than 2% efficiency loss after being subjected to thermal stress at 60 and 80 °C.

Table 5.4 Physical characteristics of commonly employed solvents

Name (abbr)	Formula	MP (°C)	BP (°C)	Viscosity (cp)	Dielectric constant	Donor number
Acetonitrile (AN)	CH_3CN	-44	82	0.33 [a]	36	14.1
Valeronitrile (VN)	$CH_3(CH_2)_2CN$	-96	139	0.78 [b]	21	
3-Methoxypropionitrile (MPN)	$CH_3O(CH_2)_2CN$	-63	164	2.50 [c]	36	16.1

[a] at 30 °C, [b] at 19 °C, [c] at 25 °C

The liquid electrolyte is made up of the redox couple, an additive, and an organic solvent or ionic liquid. Gratzel et al. were the first to employ 4-tert-butylpyridine (TBP) as an additive in electrolytes in 1993, leading to a considerable improvement in the V_{OC} of DSSC [193]. Therefore, nitrogen-containing heterocyclic compounds, including those that are analogues or derivatives of pyridine, alkyl amino pyridine, alkylpyridine, benzimidazole, pyrazol, chinoleine, etc., have been investigated for their potential use as additives in liquid electrolytes. Because these nitrogen-containing heterocyclic compounds demonstrated effects that were comparable to those of TBP, they have emerged as the most popular additions in electrolytes for the purpose of enhancing the V_{OC} [172, 194-199].

According to the findings of Huang and colleagues, the incorporation of TBP and pyridine derivatives has the potential to bring about a 1-2 order of magnitude reduction in the rate of electron recombination [200]. Based on intensity-modulated photovoltage spectroscopy (IMVS) studies, Schlichthorl et al. concluded that the negative shift of the conduction band edge of TiO_2 film was mostly responsible for the substantial increase in V_{OC} [201]. Boschloo et al. discovered that the rise in V_{OC} might be attributable to a combination of the conduction band edge shift of TiO_2 toward higher energy levels and longer electron lifetimes within the conduction band [202]. An in-situ Raman spectroscopy measurement revealed that TBP bonded to the TiO_2 surface, and most likely to iodine or the dye molecules as well [203], which was verified by a surface analysis [204, 205]. Since the nitrogen-containing heterocyclic additive is a type of base, the additives have the same impact and mechanism as the solvent donor numbers previously indicated [172, 194, 199]. The function of the additive for optimizing the photovoltaic performance of DSSCs is more effective than that of the solvent donor number. It is noteworthy that the unnecessary addition will reduce the photovoltaic efficiency of DSSCs. Wu's research also revealed the detrimental side effects of chemicals [192].

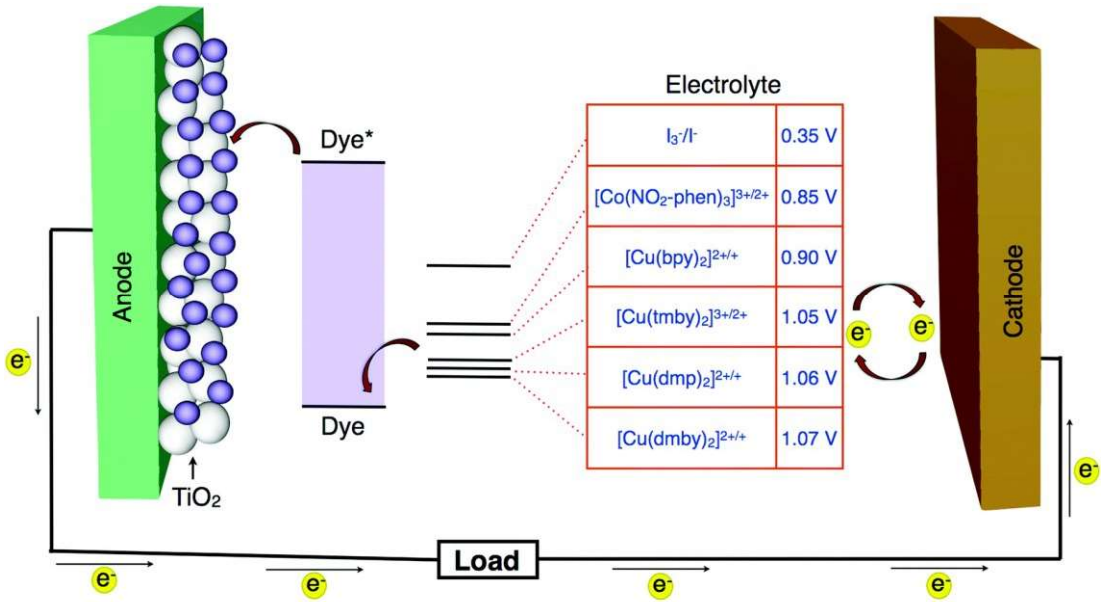


Figure 5.28 Schematic energy level diagram of a dye-sensitized solar cell.

The output voltage of the device is equal to the potential difference that exists between the level of the work function of the electrolyte and the level of the fermi in the mesoporous metal oxide. Figure 5.28 depicts the output voltages corresponding to iodine, cobalt, and copper-based redox pairs. Copper-based electrolytes pass 1 V when only an iodine-based redox couple is used but remain in the 0.35 V band.

5.3.3 Photovoltaic performance parameters

Figure 5.29 shows the effect of electrolytes commonly used in the literature on photovoltaic performance. MNP was used as a solvent in EL7, and MNP was preferred because of its high boiling point. Electrical conductivity increases the long-term stability while causing a weaker electrode. In the electrolyte called EL6, I_2 and CuSCN were used as the redox couple. The CuSCN used causes a downward shift in the work function of the electrolyte, resulting in an increase in Voc. However, it causes a serious decrease in the current value. The electrolyte formula, called EL6, is sensitive to low temperatures, and precipitation is observed at these temperatures. However, the highest fill factor was again observed in EL6.

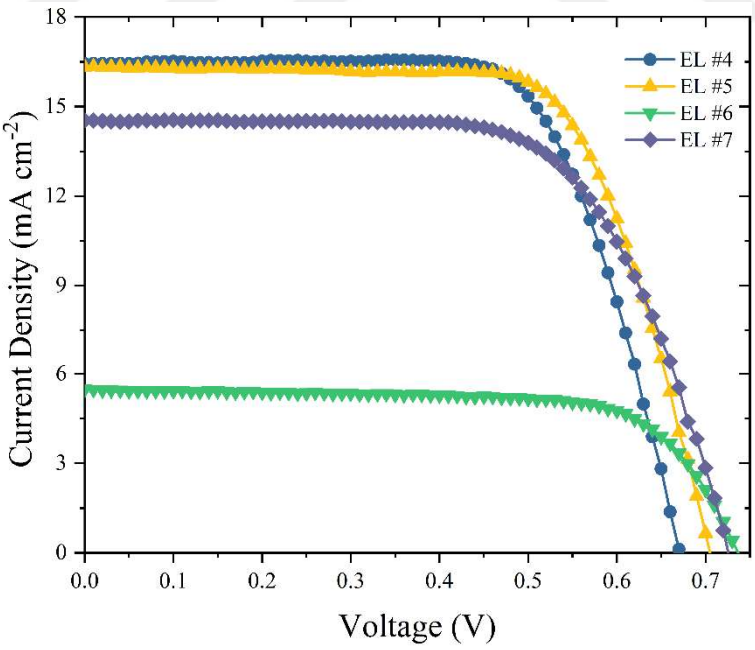


Figure 5.29 JV curves of DSSCs

BMII is an ionic liquid that can be used with all electrodes. It works to increase the conductivity of the electrolyte and has a low vapor pressure and a high level of

chemical stability. Because of its high hole handling efficiency as well as its long service life, TBP is a material that is frequently used as HTM in DSSCs. In addition to that, it is not too expensive and is not too difficult to produce. On the other hand, TBP possesses an energy level that is on the lower end, which indicates that it does not transport holes as effectively as some other HTMs that have higher energy levels. It was utilized in exactly the same manner across the board, with the exception of EL7. Guanidinium thiocyanate (GuSCN) is a chemical compound that is used in dye-sensitized solar cells (DSSCs) as a sensitizing agent. In a DSSC, the sensitizing agent is a molecule that absorbs sunlight and transfers the absorbed energy to the semiconductor material, such as titanium dioxide (TiO_2). The sensitizing agent is responsible for converting the absorbed sunlight into electrical energy, which can be used to power devices. GuSCN is a common choice for the sensitizing agent in DSSCs because it has a strong absorption coefficient and a wide absorption spectrum. It is also relatively cheap and easy to synthesize. However, GuSCN has a relatively low efficiency at converting absorbed sunlight into electrical energy, compared to some other sensitizing agents that have higher efficiencies. It is not used in electrolytes called EL6 and EL7. It has been used to varying degrees by the others.

Table 5.5 Performance parameters of DSSCs various electrolytes

Samples	**J_{sc}**	**V_{oc}**	**FF**	**η**
	mA cm^{-2}	**V**	**%**	**%**
EL#4	16.44	0.67	0.69	**7.68**
	16.43±0.13	0.67±0.01<	0.69±0.01<	7.65±0.04
EL#5	16.31	0.70	0.69	**8.03**
	16.51±0.13	0.7±0.01<	0.69±0.01	7.96±0.05
EL#6	5.48	0.74	0.71	**2.86**
	5.48±0.03	0.74±0.01<	0.7±0.01<	2.84±0.02
EL#7	14.54	0.73	0.66	**7.00**
	14.50±0.08	0.73±0.01<	0.66±0.01<	6.96±0.06

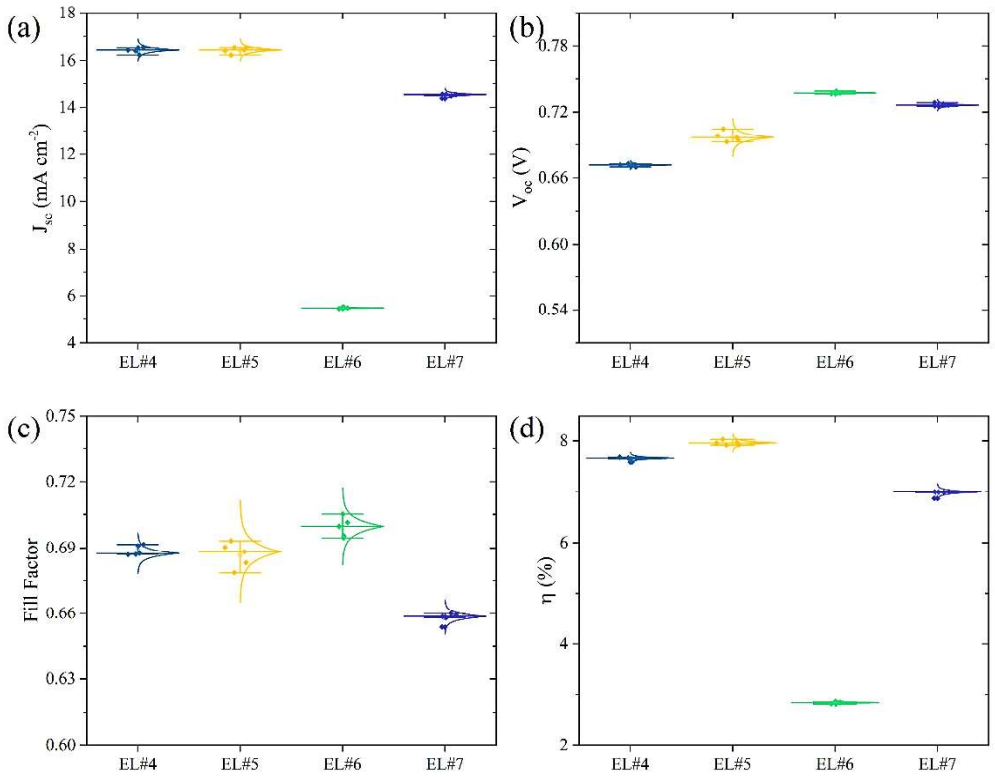


Figure 5.30 Performance parameter statistics of solar cells versus electrolyte

The electrolyte must have a certain concentration of LiI and I_2 in order to function properly. If the concentration of LiI in the electrolyte is too low, the cell will have a low open-circuit voltage (Voc), which means that it will be less efficient at converting sunlight into electricity. On the other hand, if the concentration of LiI is too high, the cell will have a high Voc, but the overall efficiency of the cell will be reduced due to the increased resistance of the electrolyte.

Similarly, if the concentration of I_2 in the electrolyte is too low, the cell will have a low short-circuit current density (Jsc), which means that it will be less efficient at converting sunlight into electricity. On the other hand, if the concentration of I_2 is too high, the cell will have a high Jsc, but the overall efficiency of the cell will be reduced due to the increased resistance of the electrolyte. Overall, it is important to keep the right amount of LiI and I_2 in the electrolyte of a DSSC so that the cell works well and turns as much sunlight into electricity as possible.

CHAPTER 6

RESULT AND DISCUSSION

6.1 Conclusions

The objective of this thesis research was to create well-designed photoanodes and electrolytes to further improve the performance of DSSCs. The key findings are as follows:

The initial phase of the research for the thesis consisted of the design and optimization of a $TiCl_3$-based blocking layer. The parameters that were taken into consideration for this stage of the research included molarity, annealing temperature and time, coating cycle, and coating speed. It was determined which parameters were the most appropriate for the blocking layer, and characterizations that included transparency and surface passivizing stood out as particularly important for testing the performance.

NiO was used in the second stage to repair the surface flaws that were present on the P25 nanoparticles. It was discovered that the position of the Ni-doped TiO_2/TiO_2 was the one that was most suitable for the additive layer. Titanium undergoes a transformation when nickel is added to it, and as a result, it acquires a negative shift in the transmission band of dioxide.

This shift results in a wider gap between the photoanodes and the electrolytes, as well as an increase in the amount of volatile organic compounds (V_{OC}). It has been discovered that the particles slow down the process of recombination, even though they cause faster injection and transport in their locations. This resulted in an increase in V_{OC} as well as J_{SC} values at the same time.

In the third part of the process, the developed solar cell is tested with a variety of electrolytes to determine which one works best. One of the tried electrolytes was CuSCN and I_2, while the LiI and I_2 redox pair were used in others. The CuSCN-based electrolyte showed the highest V_{OC} value. In the study range of long-term

stability and durability, MNP was used as an electrolyte solvent, and the boiling point is high and the steam pressure, DSSC, is low. The solvent MPN has a concentration of 7% in electrolyte. ACN, mixture of ACN, and VCN solvents which exhibited high efficiency in other electrolytes, were used. The highest yield was observed with electrolyte tagged as EL5. EL5 is a photovoltaic performance parameters J_{SC} 16.1 mA cm^{-2}, V_{OC} 0.7 V, FF 0.69 and efficiency 8.03% can be listed.

6.2 Outlook

The efficiency of the solar cells that were sensitive to paint stayed in the 13% band for a considerable amount of time before gradually increasing to 14.3% and 15.2%. Even though it has been in operation for a considerable amount of time, it continues to garner interest on academic as well as industrial levels. The following areas of focus are ones in which work can be taken to higher levels with increased values of efficiency:

- In Chapter 5.1, a formula was developed that demonstrates how the blocking layer performs its functions. This formula can be validated and taken even further by using a variety of units of measurement.
- However, for other coating techniques such as spray pyrolysis and chemical bath, the tested number of coating cycles, initial solution concentration, and annealing duration-temperature parameters are also investigated. This literature will help you understand why techniques are superior.
- Nickel was utilized in the process of surface modification described in Chapter 5.2. Using alternative elements such as aluminum, zirconium, and magnesium in place of nickel may also produce effective and promising results.
- It will be interesting, in addition to surface modification, to use different metal oxides as dopants of similar sizes.
- Only iodine-based electrolytes were used in Section 5.3 due to the limited options available; however, electrolytes containing iron, copper, and cobalt were reported to reach higher V_{OC} values. This has the potential to boost performance.

REFERENCES

[1] R. E. Smalley, "Top ten problems of humanity for next 50 years," in Energy & NanoTechnology Conference, 2003: Rice University Houston, TX.

[2] M. Grätzel, "Dye-sensitized solar cells," Journal of photochemistry and photobiology C: Photochemistry Reviews, vol. 4, no. 2, pp. 145-153, 2003.

[3] A. Nukusheva, G. Ilyassova, D. Rustembekova, R. Zhamiyeva, and L. Arenova, "Global warming problem faced by the international community: International legal aspect," International Environmental Agreements: Politics, Law and Economics, vol. 21, no. 2, pp. 219-233, 2021.

[4] S. Dale, "BP statistical review of world energy," BP Plc, London, United Kingdom, pp. 14-16, 2021.

[5] M. Z. Jacobson, "Roadmaps to transition countries to 100% clean, renewable energy for all purposes to curtail global warming, air pollution, and energy risk," Earth's Future, vol. 5, no. 10, pp. 948-952, 2017.

[6] M. Z. Jacobson et al., "100% clean and renewable wind, water, and sunlight all-sector energy roadmaps for 139 countries of the world," Joule, vol. 1, no. 1, pp. 108-121, 2017.

[7] A. Smets, K. Jäger, O. Isabella, R. van Swaaij, and M. Zeman, Solar Energy: The Physics and Engineering of Photovoltaic Conversion, Technologies and Systems. UIT Cambridge, 2016.

[8] F. Akarslan, "Photovoltaic systems and applications," Modeling and Optimization of Renewable Energy Systems, vol. 3, pp. 1035-1041, 2012.

[9] A. Blakers and M. Green, "20% efficiency silicon solar cells," Applied physics letters, vol. 48, no. 3, pp. 215-217, 1986.

[10] N. D. Oyeniran, "Evaluation of thermal performance on a stand alone pv solar inverter," Ladoke Akintola University Of Technology, 2018.

[11] R. King et al., "40% efficient metamorphic GaInP⁄ GaInAs⁄ Ge multijunction solar cells," Applied physics letters, vol. 90, no. 18, p. 183516, 2007.

[12] M. Bakker, H. Zondag, M. Elswijk, K. Strootman, and M. Jong, "Performance and costs of a roof-sized PV/thermal array combined with a ground coupled heat pump," Solar energy, vol. 78, no. 2, pp. 331-339, 2005.

[13] K. Bilen et al., "Energy production, consumption, and environmental pollution for sustainable development: A case study in Turkey," Renewable and Sustainable Energy Reviews, vol. 12, no. 6, pp. 1529-1561, 2008/08/01/ 2008..

[14] M. J. Barasa Kabeyi and O. A. Olanrewaju, "Geothermal wellhead technology power plants in grid electricity generation: A review," Energy Strategy Reviews, vol. 39, p. 100735, 2022/01/01/ 2022.

[15] A. Rahman, O. Farrok, and M. M. Haque, "Environmental impact of renewable energy source based electrical power plants: Solar, wind, hydroelectric, biomass, geothermal, tidal, ocean, and osmotic," Renewable and Sustainable Energy Reviews, vol. 161, pp. 112279 (1-29), 06/01 2022, doi: 10.1016/j.rser.2022.112279.

[16] M. Parfit, "Future power: Where will the world get its next energy fix," National Geographic, vol. 208, no. 2, pp. 2-31, 2005.

[17] W. Shockley, "The Shockley-Queisser limit," J. Appl. Phys, vol. 32, no. 3, pp. 510-519, 1961.

[18] B. O'regan and M. Grätzel, "A low-cost, high-efficiency solar cell based on dye-sensitized colloidal TiO2 films," nature, vol. 353, no. 6346, pp. 737-740, 1991.

[19] Y. Ren et al., "Hydroxamic acid pre-adsorption raises the efficiency of cosensitized solar cells," Nature, 2022/10/26 2022, doi: 10.1038/s41586-022-05460-z.

[20] A. Atli, A. Atilgan, C. Altinkaya, K. Ozel, and A. Yildiz, "St. Lucie cherry, yellow jasmine, and madder berries as novel natural sensitizers for dye-sensitized solar cells," (in English), International Journal of Energy Research, vol. 43, no. 8, pp. 3914-3922, Jun 25 2019, doi: 10.1002/er.4538.

[21] Y. Kocak, A. Atli, A. Atilgan, and A. Yildiz, "Extraction method dependent performance of bio-based dye-sensitized solar cells (DSSCs)," Materials Research Express, vol. 6, no. 9, p. 095512, 2019.

[22] Y. Kocak and A. Yildiz, "Carminic acid extracted from cochineal insect as photosensitizer for dye-sensitized solar cells," International Journal of Energy Research, vol. 45, no. 11, pp. 16901-16907, 2021.

[23] Z. K. Yildiz, A. Atilgan, A. Atli, K. Ozel, C. Altinkaya, and A. Yildiz, "Enhancement of efficiency of natural and organic dye sensitized solar cells using thin film TiO2 photoanodes fabricated by spin-coating," (in English), J Photoch Photobio A, vol. 368, pp. 23-29, Jan 1 2019, doi: 10.1016/j.jphotochem.2018.09.018.

[24] C. Altinkaya, A. Atli, A. Atilgan, K. Salimi, and A. Yildiz, "Facile fabrication of low-cost low-temperature carbon-based counter electrode with an outstanding fill factor of 73% for dye-sensitized solar cells," International Journal of Energy Research, vol. 44, no. 4, pp. 3160-3170, 2020.

[25] S. Akin, E. Erol, and S. Sonmezoglu, "Enhancing the electron transfer and band potential tuning with long-term stability of ZnO based dye-sensitized solar cells by gallium and tellurium as dual-doping," Electrochimica Acta, vol. 225, pp. 243-254, 2017.

[26] S. Akin, Y. Ulusu, H. Waller, J. H. Lakey, and S. Sonmezoglu, "Insight into interface engineering at TiO2/dye through molecularly functionalized caf1 biopolymer," ACS Sustainable Chemistry & Engineering, vol. 6, no. 2, pp. 1825-1836, 2018.

[27] X.-Q. Gong and A. Selloni, "Reactivity of anatase TiO2 nanoparticles: the role of the minority (001) surface," The Journal of Physical Chemistry B, vol. 109, no. 42, pp. 19560-19562, 2005.

[28] M.-C. Kao, H.-Z. Chen, and S.-L. Young, "Improved Energy Conversion Efficiency of TiO2 Thin Films Modified with Ta2O5 in Dye-Sensitized Solar Cells," Japanese Journal of Applied Physics, vol. 52, no. 1S, p. 01AD04, 2013.

[29] M. Rashad and A. Shalan, "Hydrothermal synthesis of hierarchical WO3 nanostructures for dye-sensitized solar cells," Applied Physics A, vol. 116, no. 2, pp. 781-788, 2014.

[30] M. Ye et al., "Recent advances in dye-sensitized solar cells: from photoanodes, sensitizers and electrolytes to counter electrodes," Materials Today, vol. 18, no. 3, pp. 155-162, 2015.

[31] J. Desilvestro, M. Graetzel, L. Kavan, J. Moser, and J. Augustynski, "Highly efficient sensitization of titanium dioxide," Journal of the American Chemical Society, vol. 107, no. 10, pp. 2988-2990, 1985.

[32] Z. Su and W. Zhou, "Formation, morphology control and applications of anodic TiO 2 nanotube arrays," Journal of Materials Chemistry, vol. 21, no. 25, pp. 8955-8970, 2011.

[33] H. Tsubomura, M. Matsumura, Y. Nomura, and T. Amamiya, "Dye sensitised zinc oxide: aqueous electrolyte: platinum photocell," Nature, vol. 261, no. 5559, pp. 402-403, 1976.

[34] Y. Fukai, Y. Kondo, S. Mori, and E. Suzuki, "Highly efficient dye-sensitized SnO2 solar cells having sufficient electron diffusion length," Electrochemistry Communications, vol. 9, no. 7, pp. 1439-1443, 2007.

[35] K. Keis et al., "Nanostructured ZnO electrodes for dye-sensitized solar cell applications," Journal of Photochemistry and photobiology A: Chemistry, vol. 148, no. 1-3, pp. 57-64, 2002.

[36] S. Nakade, Y. Makimoto, W. Kubo, T. Kitamura, Y. Wada, and S. Yanagida, "Roles of electrolytes on charge recombination in dye-sensitized TiO2 solar cells (2): the case of solar cells using cobalt complex redox couples," The Journal of Physical Chemistry B, vol. 109, no. 8, pp. 3488-3493, 2005.

[37] F. Gao et al., "Enhance the optical absorptivity of nanocrystalline TiO2 film with high molar extinction coefficient ruthenium sensitizers for high performance dye-sensitized solar cells," Journal of the American Chemical Society, vol. 130, no. 32, pp. 10720-10728, 2008.

[38] M. Toivola, F. Ahlskog, and P. Lund, "Industrial sheet metals for nanocrystalline dye-sensitized solar cell structures," Solar Energy Materials and Solar Cells, vol. 90, no. 17, pp. 2881-2893, 2006/11/06/ 2006.

[39] J. Wu et al., "Progress on the electrolytes for dye-sensitized solar cells," Pure and Applied Chemistry, vol. 80, no. 11, pp. 2241-2258, 2008, doi: doi:10.1351/pac200880112241.

[40] S. Thomas, T. Deepak, G. Anjusree, T. Arun, S. V. Nair, and A. S. Nair, "A review on counter electrode materials in dye-sensitized solar cells," Journal of Materials Chemistry A, vol. 2, no. 13, pp. 4474-4490, 2014.

[41] A. Hauch and A. Georg, "Diffusion in the electrolyte and charge-transfer reaction at the platinum electrode in dye-sensitized solar cells," Electrochimica acta, vol. 46, no. 22, pp. 3457-3466, 2001.

[42] N. Papageorgiou, W. Maier, and M. Grätzel, "An iodine/triiodide reduction electrocatalyst for aqueous and organic media," Journal of the electrochemical Society, vol. 144, no. 3, p. 876, 1997.

[43] K. Kalyanasundaram and M. Grätzel, "Applications of functionalized transition metal complexes in photonic and optoelectronic devices," Coordination chemistry reviews, vol. 177, no. 1, pp. 347-414, 1998.

[44] A. Hagfeldt, G. Boschloo, L. Sun, L. Kloo, and H. Pettersson, "Dye-sensitized solar cells," Chemical reviews, vol. 110, no. 11, pp. 6595-6663, 2010.

[45] A. Yella et al., "Porphyrin-sensitized solar cells with cobalt (II/III)–based redox electrolyte exceed 12 percent efficiency," science, vol. 334, no. 6056, pp. 629-634, 2011.

[46] M. K. Nazeeruddin et al., "Conversion of light to electricity by cis-X2bis (2, 2'-bipyridyl-4, 4'-dicarboxylate) ruthenium (II) charge-transfer sensitizers (X= Cl-, Br-, I-, CN-, and SCN-) on nanocrystalline titanium dioxide electrodes," Journal of the American Chemical Society, vol. 115, no. 14, pp. 6382-6390, 1993.

[47] J. B. Asbury, R. J. Ellingson, H. N. Ghosh, S. Ferrere, A. J. Nozik, and T. Lian, "Femtosecond IR study of excited-state relaxation and electron-injection dynamics of Ru (dcbpy) 2 (NCS) 2 in solution and on nanocrystalline TiO2 and Al2O3 thin films," The Journal of Physical Chemistry B, vol. 103, no. 16, pp. 3110-3119, 1999.

[48] H. Tributsch, "Reaction of excited chlorophyll molecules at electrodes and in photosynthesis," Photochemistry and Photobiology, vol. 16, no. 4, pp. 261-269, 1972.

[49] H. Gerischer and F. Willig, "Reaction of excited dye molecules at electrodes," Physical and Chemical Applications of Dyestuffs, pp. 31-84, 1976.

[50] M. K. Nazeeruddin et al., "Acid− Base equilibria of (2, 2 ‘-Bipyridyl-4, 4 ‘-dicarboxylic acid) ruthenium (II) complexes and the effect of protonation on charge-transfer sensitization of nanocrystalline titania," Inorganic Chemistry, vol. 38, no. 26, pp. 6298-6305, 1999.

[51] M. K. Nazeeruddin, P. Pechy, and M. Grätzel, "Efficient panchromatic sensitization of nanocrystallineTiO2 films by a black dye based on atrithiocyanato–ruthenium complex," Chemical Communications, no. 18, pp. 1705-1706, 1997.

[52] J. N. Clifford, E. Palomares, M. K. Nazeeruddin, M. Grätzel, and J. R. Durrant, "Dye dependent regeneration dynamics in dye sensitized nanocrystalline solar

cells: evidence for the formation of a ruthenium bipyridyl cation/iodide intermediate," The Journal of Physical Chemistry C, vol. 111, no. 17, pp. 6561-6567, 2007.

[53] S. Pelet, J.-E. Moser, and M. Grätzel, "Cooperative effect of adsorbed cations and iodide on the interception of back electron transfer in the dye sensitization of nanocrystalline TiO2," The Journal of Physical Chemistry B, vol. 104, no. 8, pp. 1791-1795, 2000.

[54] M. S. Ahmad, A. K. Pandey, and N. Abd Rahim, "Advancements in the development of TiO2 photoanodes and its fabrication methods for dye sensitized solar cell (DSSC) applications. A review," Renewable and Sustainable Energy Reviews, vol. 77, pp. 89-108, 2017.

[55] F. C. Krebs, "Fabrication and processing of polymer solar cells: A review of printing and coating techniques," Solar energy materials and solar cells, vol. 93, no. 4, pp. 394-412, 2009.

[56] V. Hubka, Principles of engineering design. Elsevier, 2015.

[57] F. Padinger, C. Brabec, T. Fromherz, J. Hummelen, and N. S. Sariciftci, "Fabrication of large area photovoltaic devices containing various blends of polymer and fullerene derivatives by using the doctor blade technique," Optoelectronics Review, no. 4, pp. 280-283, 2000.

[58] A. Mishra, N. Bhatt, and A. Bajpai, "Nanostructured superhydrophobic coatings for solar panel applications," in Nanomaterials-Based Coatings: Elsevier, 2019, pp. 397-424.

[59] R. Nagarjuna, S. Roy, and R. Ganesan, "Polymerizable sol–gel precursor mediated synthesis of TiO2 supported zeolite-4A and its photodegradation of methylene blue," Microporous and Mesoporous Materials, vol. 211, pp. 1-8, 2015.

[60] K. Sharma, B. Kaith, V. Kumar, S. Kalia, V. Kumar, and H. Swart, "Water retention and dye adsorption behavior of Gg-cl-poly (acrylic acid-aniline) based conductive hydrogels," Geoderma, vol. 232, pp. 45-55, 2014.

[61] K.-C. Lee and J.-G. Hwu, "Efficiency improvement in low temperature metal-oxide-semiconductor solar cells by thin metal film deposition on photon receiving area," Journal of Vacuum Science & Technology A: Vacuum, Surfaces, and Films, vol. 16, no. 4, pp. 2641-2645, 1998.

[62] G. Kirchhoff, "Über das Verhältnis zwischen dem Emissionsvermögen und dem Absorptionsvermögen der Körper für Wärme und Licht," in Von Kirchhoff bis Planck: Springer, 1978, pp. 131-151.

[63] P. Wurfel and W. Ruppel, "Upper limit of thermophotovoltaic solar-energy conversion," IEEE Transactions on Electron Devices, vol. 27, no. 4, pp. 745-750, 1980.

[64] L. C. Hirst and N. J. Ekins-Daukes, "Fundamental losses in solar cells," Progress in Photovoltaics: Research and Applications, vol. 19, no. 3, pp. 286-293, 2011.

[65] C. A. Nelson, N. R. Monahan, and X.-Y. Zhu, "Exceeding the Shockley–Queisser limit in solar energy conversion," Energy & Environmental Science, vol. 6, no. 12, pp. 3508-3519, 2013.

[66] F. Kabir, S. N. Sakib, S. S. Uddin, E. T. Efaz, and M. T. F. Himel, "Enhance cell performance of DSSC by dye mixture, carbon nanotube and post TiCl4 treatment along with degradation study," Sustainable Energy Technologies and Assessments, vol. 35, pp. 298-307, 2019.

[67] G. N. Arka, S. B. Prasad, and S. Singh, "Comprehensive study on dye sensitized solar cell in subsystem level to excel performance potential: A review," Solar Energy, vol. 226, pp. 192-213, 2021.

[68] V. Manthina and A. G. Agrios, "Blocking layers for nanocomposite photoanodes in dye sensitized solar cells: Comparison of atomic layer

deposition and TiCl4 treatment," (in English), Thin Solid Films, vol. 598, pp. 54-59, Jan 1 2016, doi: 10.1016/j.tsf.2015.11.054.

[69] V. Manthina and A. G. Agrios, "Single-pot ZnO nanostructure synthesis by chemical bath deposition and their applications," Nano-Structures & Nano-Objects, vol. 7, pp. 1-11, 2016.

[70] T. P. Brennan et al., "The importance of dye chemistry and TiCl 4 surface treatment in the behavior of Al 2 O 3 recombination barrier layers deposited by atomic layer deposition in solid-state dye-sensitized solar cells," Physical Chemistry Chemical Physics, vol. 14, no. 35, pp. 12130-12140, 2012.

[71] S. M. Prokes, J. L. Gole, X. B. Chen, C. Burda, and W. E. Carlos, "Defect-related optical behavior in surface-modified TiO2 nanostructures," (in English), Advanced Functional Materials, vol. 15, no. 1, pp. 161-167, Jan 2005, doi: 10.1002/adfm.200305109.

[72] S. Wendt et al., "The role of interstitial sites in the Ti 3d defect state in the band gap of titania," Science, vol. 320, no. 5884, pp. 1755-1759, 2008.

[73] P. M. Sommeling et al., "Influence of a TiCl4 post-treatment on nanocrystalline TiO2 films in dye-sensitized solar cells," J Phys Chem B, vol. 110, no. 39, pp. 19191-7, Oct 5 2006, doi: 10.1021/jp061346k.

[74] B. C. O'Regan, J. R. Durrant, P. M. Sommeling, and N. J. Bakker, "Influence of the TiCl4 treatment on nanocrystalline TiO2 films in dye-sensitized solar cells. 2. Charge density, band edge shifts, and quantification of recombination losses at short circuit," (in English), J Phys Chem C, vol. 111, no. 37, pp. 14001-14010, Sep 20 2007, doi: 10.1021/jp073056p.

[75] L. Kavan, "Titania in diverse forms as substrates," in Dye-sensitized solar cells: CRC Press Boca Raton, 2010.

[76] I. C. Baek et al., "Facile preparation of large aspect ratio ellipsoidal anatase TiO2 nanoparticles and their application to dye-sensitized solar cell," Electrochemistry Communications, vol. 11, no. 4, pp. 909-912, 2009.

[77] C.-Y. Huang, Y.-C. Hsu, J.-G. Chen, V. Suryanarayanan, K.-M. Lee, and K.-C. Ho, "The effects of hydrothermal temperature and thickness of TiO2 film on the performance of a dye-sensitized solar cell," Solar energy materials and solar cells, vol. 90, no. 15, pp. 2391-2397, 2006.

[78] Y. Lei, H. Liu, and W. Xiao, "First principles study of the size effect of TiO2 anatase nanoparticles in dye-sensitized solar cell," Modelling and Simulation in Materials Science and Engineering, vol. 18, no. 2, p. 025004, 2010.

[79] G. Li et al., "Synergistic effect between anatase and rutile TiO 2 nanoparticles in dye-sensitized solar cells," Dalton Transactions, no. 45, pp. 10078-10085, 2009.

[80] N.-G. Park, J. Van de Lagemaat, Frank, and AJ, "Comparison of dye-sensitized rutile-and anatase-based TiO2 solar cells," The Journal of Physical Chemistry B, vol. 104, no. 38, pp. 8989-8994, 2000.

[81] K. H. Ko, Y. C. Lee, and Y. J. Jung, "Enhanced efficiency of dye-sensitized TiO2 solar cells (DSSC) by doping of metal ions," Journal of colloid and interface science, vol. 283, no. 2, pp. 482-487, 2005.

[82] F. Hirose, K. Kuribayashi, T. Suzuki, Y. Narita, Y. Kimura, and M. Niwano, "UV Treatment Effect on TiO2 Electrodes in Dye-Sensitized Solar Cells with N719 Sensitizer Investigated by Infrared Absorption Spectroscopy," Electrochemical and Solid-State Letters, vol. 11, no. 7, p. A109, 2008/04/18 2008, doi: 10.1149/1.2908188.

[83] K. E. Lee, M. A. Gomez, S. Elouatik, and G. P. Demopoulos, "Further understanding of the adsorption mechanism of N719 sensitizer on anatase TiO2 films for DSSC applications using vibrational spectroscopy and confocal Raman imaging," Langmuir, vol. 26, no. 12, pp. 9575-9583, 2010.

[84] L. C. Miranda, Angelo, "Optimal effect of TiO2 particles size on the current – potential behaviour of dye sensitized TiO2 solar cells " Chemical Engineering Transactions, vol. 17, pp. 975-980, 2009, doi: 10.3303/CET0917263.